Measurement of cicular dichroism dynamics in a temperature jump experiment for the study of protein folding

Mai-Thu Khuc

PhD thesis

presented by

Mai-Thu KHUC

On the subject of:

Measurement of Circular Dichroism Dynamics in a Temperature Jump Experiment for the Study of Protein Folding

Defended on December 5th, 2011

Pascale CHANGENET-BARRET	Reviewer
Kokou Dodzi DORKENOO	Reviewer
Gilbert ZALCZER	President
Martin VOLK	Examiner
François HACHE	Advisor

ACKNOWLEDGEMENT

I would like to thank the jury for accepting and giving me the honor to present my PhD project. They also have provided me useful ideas and encouragements for this PhD thesis.

I would like to thank “generous” Jean-Louis Martin for accepting and welcoming me to do my three years of PhD in LOB.

I was extremely lucky to be given the opportunity to work with François Hache as my advisor. I could never thank him enough for his continuous and incredible support, help and advices through my three years of PhD.

Martin Volk was the one who gave me the knowledge of temperature jump experiment. I was very lucky to have a chance to work in his laboratory which is one of the world expertises in temperature jump experiment. Martin has also given me lots of advices, support and encouragement for my PhD project. I was very happy to have him as one of my jury.

I would like to thank Monique Martin, Pascal Plaza and Johanna Brazard from Ecole Normale Supérieure de Paris who have given us their precious OBIP and OxyBP samples. Also thanks to their indispensable ideas and opinions, I was able to obtain my first scientific publication about OBIP.

A great acknowledgement goes to Xavier Solinas (our LOB’s excellent technician) who has built up our sophisticated synchronization electronics. My PhD can not be completed without his wonderful hands and his so-bright head.

I would also like to thank Lucille Medonça (my very kind group mate) who has done a lot of important experiments for temperature jump estimation. She also let me learn her work of temperature jump simulation. Moreover, Lucille was the one who implemented successfully the Fast Fourier Transform technique for our signal detection. She always discussed and gave me her useful ideas and encouragement. Not only for work, was she also my lifesaver who helped me a lot with my administrative problems and so on. Also, thank you for you delicious cakes and your kind preparation for my PhD celebration party.

Latifa Bouzhir-Sima was another lifesaver. Most of my medical calls were made by her. Also thank you for your work help, your wise health advices as well as your usual talk.

I would also like to thank Jean-Marc who was always there to solve our mechanical problems.

Another acknowledgement goes to our secretarial staff (Laure Lapapelle and Christelle François) for their kind administrative assistance.

I was very happy to work with LOB people who were always nice, helpful and encouraging. Thank you all!

CNRS (for financial support) and EDX people (Pierre Legrain, Audrey Lemarechal, Fabric Baronnet, Christine Ferret) are gratefully acknowledged.

Finally, I would like to thank my family and friends who have been always there, encouraging me and keeping me sane.

TABLE OF CONTENTS

CHAPTER 1

INTRODUCTION

1.1. Importance of proteins/protein folding

Proteins are the biological workhorses that carry out numerous vital functions in every cell. Of all the molecules found in living organisms, proteins are the most important. They function as catalysts, they support the skeleton, they defend against infections, they generate movement, they control growth and differentiation, they transmit nerve impulses, and they transport and store other molecules such as oxygen. Without proteins, life that we know doesn't exist.

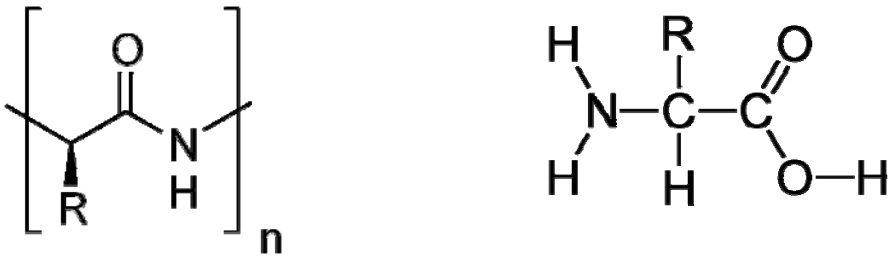

a) b)

Figure 1.1 Chemical structure of: a) A peptide bond, b) An α-amino acid in its unionized form.

Proteins are polypeptides constructed from a set of only 20 building blocks, known as amino acids, bonded together by peptide bonds between the carboxyl and amino groups of adjacent amino acid residues (figure 1.1a). The sequence of amino acids in a protein is defined by the sequence of a gene, which is encoded in the genetic code. All amino acids have

the same basic structure consisting of an amino group, a carboxyl group and a hydrogen atom but differ due to the presence of a side-chain (known as R, figure 1.1b). An amino acid can be hydrophilic (water-attracting) or hydrophobic (water-repelling), acidic or basic, depending on the properties of the side-chain.

To carry out their task, proteins must fold into a complex three-dimensional structure. The shape into which a protein naturally folds is known as its native conformation. There are four levels of protein structure:

- Primary structure defined by the amino acid sequence,
- Secondary structure is regularly repeating local structures stabilized by hydrogen bonds. The most common types are the α-helix (supported by intra-peptide hydrogen bonding between residues i and i+4), beta sheet (supported by intra-peptide hydrogen bonding between residues further apart than in the α-helix, or between different peptide strands) and random coil (showing no regular intra-peptide hydrogen bond).
- Tertiary structure is the global shape of a single protein molecule, which is formed by the spatial relationship of the secondary structures to one another. Tertiary structure is generally stabilized by nonlocal interactions, most commonly the formation of a hydrophobic core, but also through salt bridges, hydrogen bonds, disulfide bonds, and van der Waals bonds. The tertiary controls the basic function of the protein.
- Quaternary structure is the structure formed by non-covalent forces among several protein molecules (polypeptide chains), which function as a single protein complex.

Although the primary structure of a protein can be derived from the sequence of a gene, its tertiary structure can not be determined. The mystery of how polypeptides or proteins fold into their characteristic and functional three-dimensional structure is an exciting and unique challenge that has been currently being investigated in biological research.

One of the most important results in understanding the process of protein folding was a thought-provoking experiment that was carried out by C. B. Anfinsen and colleagues in the early 1960s [1]. They investigated an enzyme ribonuclease that was made of 124 amino acids. Their results demonstrated that the unfolding or “denaturation” of the enzyme was reversible. After the cleavage of disulfide bonds and disruption of tertiary structure, the enzyme spontaneously refolds to native form and its function returns. Therefore, Anfinsen proposed that the native conformation of a protein corresponds to the one of lowest Gibbs free energy

(figure 1.2) and should be determined by the amino acid sequence ("thermodymamic hypothesis", Nobel Prize 1972).

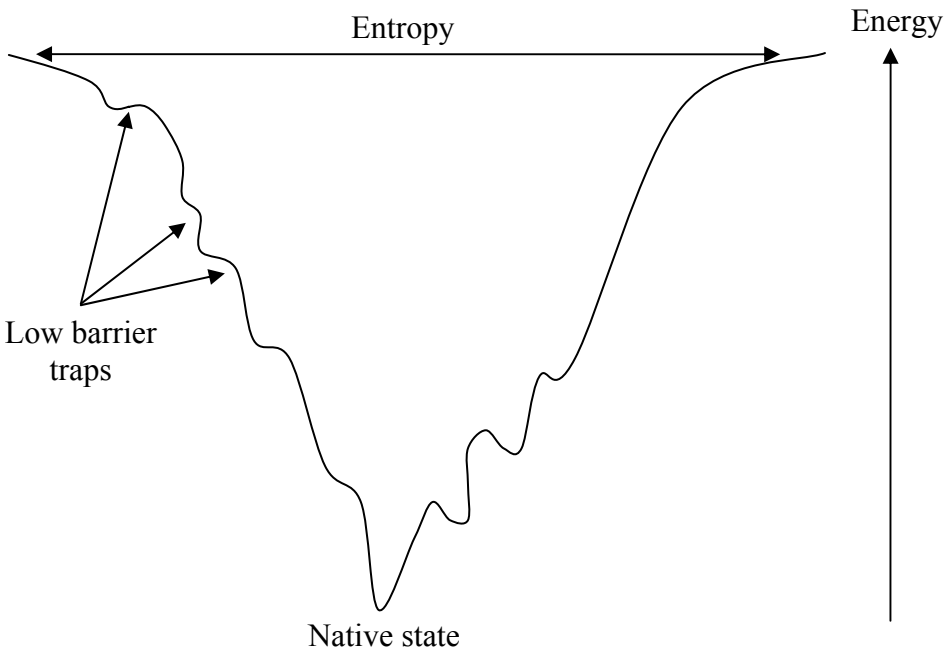

Figure 1.2 Cross section through a folding funnel. The width of the funnel represents the entropy of the polypeptide chain and the height its energy.

In 1969, C. Levinthal calculated that even if a protein only consisted of 150 amino acids and if one knows the bond angles to be better than a tenth of a radian, the protein could theoretically adopt as many as 10^{300} possible conformations (Levinthal's paradox, 1969). Assuming a protein could try out 10^{100} different conformations per second, it would still take 10^{200} years to try all possibilities. However, proteins in nature are observed to fold within milliseconds to seconds. So, Levinthal suggested protein folding is speeded and highly guided by the rapid formation of local interactions which serve as nucleation points in the folding process. Then, the final conformation does not have to be the one of lowest free energy, however, it must be a metastable state which is in a sufficient low energy to survive possible perturbations in a biological system.

Different protein folding pathways that have been investigated experimentally and theoretically in recent years have provided interesting hypotheses but still have left lots of disagreements. For proteins of less than 100 amino acids, only two levels of folding can be observed, the unfolded protein and the finished, folded, functional protein [2-7]. In the case of larger proteins, an intermediate step can be observed. Several models have been proposed to

describe this process and the underlying mechanism. These include the framework model, the diffusion-collision model, the hydrophobic collapse model and the nucleation-condensation model (see table 1.1).

Models	**Mechanisms**	**References**
Framework (figure 1.3)	Some peptide segments fold into secondary structure before being packing together to form the final three-dimensional protein. The initial secondary structures are thought to be stable.	8
Diffusion-collision	Similarly to the framework model, some peptide segments with secondary structure are formed first before packing up into the final three dimensional structures. However, the segments with secondary structure are highly unstable and present in the unfolded peptide with low probabilities. They stabilize each other only when coming into contact.	9
Hydrophobic collapse (figure 1.3)	The unfolded protein undergoes fast collapse driven by the hydrophobic effect and becomes a disordered compact state with hydrophobic side-chains in the inside and hydrophilic side-chains on the outside. Secondary structure and tertiary contacts are then formed within this compact aggregate.	10
Nucleation-condensation (figure 1.3)	Formation of a small nucleus (formation of highly-unstable secondary structure with only few residues) acts as the nucleation site for the fast propagation of the rest of the protein.	11

Table 1.1 Several different models of protein folding pathways.

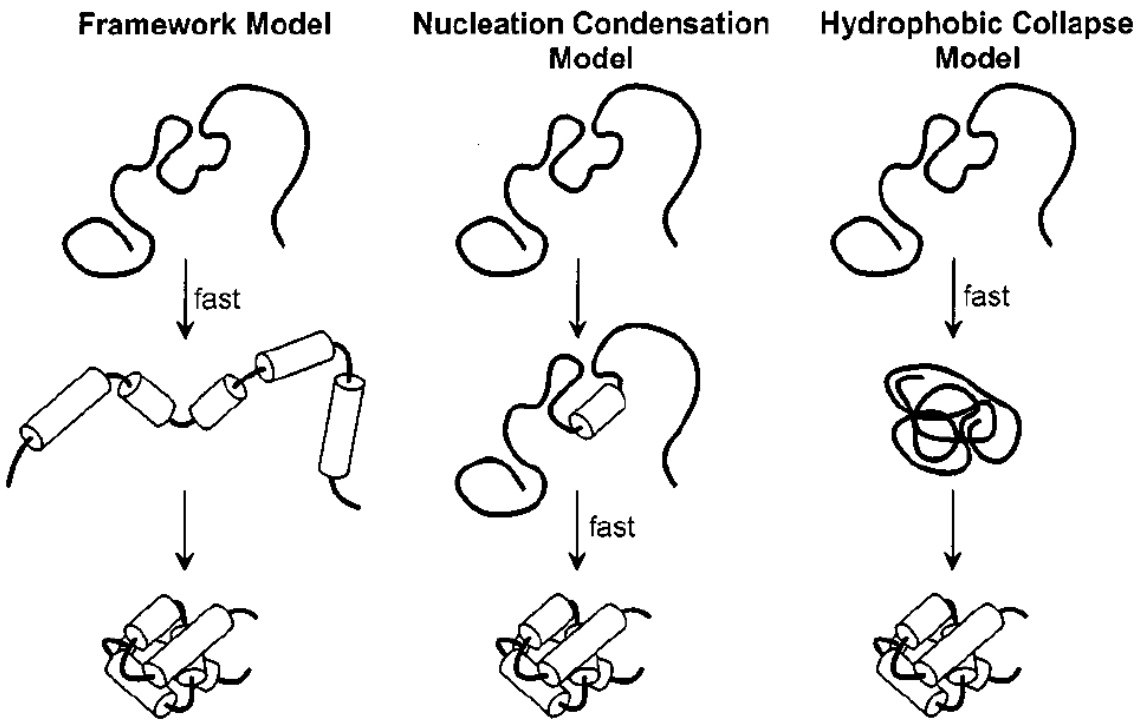

Figure 1.3 Schematic illustrations of three different models of protein folding pathways: framework model, nucleation condensation model and hydrophobic collapse model. Figure is extracted from reference [12].

As with all spontaneous processes in nature, protein folding also consumes energy. Obeying the laws of thermodynamics, a protein must fold so that it attains the lowest possible energy. It is thought that this is achieved by using an energy gradient or funnel (figure 1.2) along the path from the random tangle to the folded protein [13]. As each protein seeks out its natural shape through a funnel of declining energy, it can take many folding routes and still reach its target of the completed three-dimensional structure. So, fixed reaction pathways are not any more necessary. This understanding of protein folding was obtained from both computational simulations of model proteins and experimental studies [14], and it has been used to improve methods for protein structure prediction and design [14].

As mention previously, Anfinsen has shown that if proteins become unfolded, they fold back into their original proper shape; no shaper or folder is needed. However, we know now that protein folding can go wrong. For example, when an egg is boiled, the proteins in the white part unfold. But when the egg cools, the proteins don't turn back to their original structures. Instead, they form a solid, insoluble mass. This is misfolding. A fully denatured protein exists as a random coil. Under certain conditions, some proteins can refold into their original three-dimensional conformation. However, in many cases, denaturation is irreversible; after denaturation, proteins forms insoluble amorphous aggregate of protein

fibers instead of folding back to their initial three-dimensional structures [15]. Misfolding of proteins, in which proteins convert into highly ordered fibrillar aggregates, is behind many diseases such as prion-related illnesses (Creutzfeldt-Jakob disease, mad cow disease), amyloid-related illnesses (Alzheimer's disease, familial amyloid polyneuropathy), as well as intracytoplasmic aggregation diseases (Huntington's and Parkinson's disease) [16]. It is thought that the misfolding process is provoked by secondary structure transformation from α-helices into β-sheets, which prevents normal cellular processes.

On the other hand, dynamic aspects of protein folding are important for correct prediction of the folding pathway of any natural or design protein, and so are of great value for the prediction of its final three-dimensional structure [12]. Besides, information on the dynamic of protein folding, and of secondary structure formation in particular, may also help explain the molecular mechanisms behind conditions that leads to misfolding of proteins [12], and thus, may be useful for prevention or treatment for the diseases involved.

It is often believed that the formation of secondary structural elements, such as α-helices, β-strands or β-turns, is the first rapid stage of protein folding, in which the fully unfolded polypeptide collapses into a more compact form [8, 9, 11]. After the formation of the secondary structures, the number of possible conformations that the protein has to explore in the search for the lowest free energy state is greatly reduced. These secondary structure elements may then act as nucleation sites for the further collapse to the final native conformation. This project aims to investigate the fast folding dynamics of α-helices, which is the most common secondary structure found in almost all native proteins for a purpose of understanding the initial phrase of the whole process of protein folding.

1.2. Techniques for observation of fast folding processes in real-time

According to molecular dynamics simulations, α-helix formation was predicted to occur on the 10-ns timescale [17]. Numerous techniques are currently available for the real-time observation of fast folding dynamics of peptides or proteins on such a short timescale. Some of these techniques allow monitoring of highly localized structural changes, whereas others are sensitive to overall secondary structural changes or global movements of the whole protein structure. These techniques are thus complementary and can provide different

information (local and global) on the folding dynamics of a same protein. The simultaneous use of several methods usually significantly enhances the interpretation of results obtained from a particular experiment.

1.2.1. Absorbance

The movement of a cofactor from an exterior environment into the protein interior shifts the position of its absorbance bands, which is usually sensitive to local environmental changes. For example, time-resolved absorption spectroscopy has been used to monitor the ligand-binding process of heme proteins [18-21] or the whole collapse process of such proteins [22] by following the change in absorption of the proteins' heme groups in the spectral range of 400-430 nm.

1.2.2. Infrared absorbance

Infrared spectroscopy is generally applied for direct observing secondary structural changes in proteins and peptides. The peptide amide I band near 1650 cm^{-1}, which mainly originates from the C=O stretch vibration of the peptide backbone, is very sensitive to changes in secondary structure of proteins/peptides [23]. Upon secondary structure formation, its frequency is shifted by hydrogen bonding and transition dipole coupling, both of which depend on the relative geometry of the peptide groups [24]. For example, an increase in the temperature shifts the helix-coil equilibrium of a peptide towards less helical conformation. This results in a broadening of the amide I band and a shift of the band maximum to higher frequency [25]. Time-resolved IR spectroscopy has been used to monitor the changes in the overall secondary and tertiary structure of proteins [26-29] and peptides [2, 4, 6, 25, 30-33].

Local probing at residue level can be achieved with the help of isotopic labeling such as the replacement of $^{12}C=^{16}O$ by $^{13}C=^{16}O$/$^{13}C=^{18}O$, which shifts the amide I band by approximately 40 cm^{-1} ($^{13}C=^{16}O$ labeling [34])/60 cm^{-1} ($^{13}C=^{18}O$ labeling [35]) toward lower frequencies. $^{13}C=^{16}O$ isotope-edited IR spectroscopy has been used to selectively determine the stability of different parts of an α-helical peptide [36]. Ultrafast protein folding dynamics at residue specific resolution has been studied in time-resolved IR measurements using $^{13}C=^{18}O$ label [35].

1.2.3. Fluorescence

The aromatic amino acid residues of proteins can be used as intrinsic fluorescence probes, avoiding any distortion effects on the proteins. On the other hand, external fluorophores can be bound to the peptide chain covalently or attached noncovalently as extrinsic probes. Fluorescence methods can be used to observe both local and global structural changes of proteins, depending on the property of the fluorophore, the presence of fluorescence quenchers and the particular fluorescence characteristics being measured (table 1.2).

Fluorescence methods	**Properties**	**Information**	**References**
Spectral characteristics	Spectrum of the fluorescence probe, which has characteristics highly sensitive to the surroundings, shifts upon folding from the random coil to a more compact structure.	Local/Global	37, 38
Fluorescence quenching *(measured either by the overall fluorescence yield or by time-resolved fluorescence decay)*	Folding of a protein prevents an additional extrinsic fluorescence quencher from accessing the fluorophore.	Local/Global	39, 40
	Quenching of the fluorescence signal of an energy donor in the presence of an energy acceptor by distance-dependent nonradiative excitation energy transfer. The energy acceptor can be intrinsic or extrinsic chromophore and can be bound covalently to the peptide backbone.	Local	19, 41-44

Table 1.2 Different fluorescence methods for observation of fast dynamics of protein folding.

1.2.4. UV resonance Raman scattering

UV Resonance Raman (UVRR) spectroscopy has been proved to have potential in the studies of protein folding for observing overall secondary structure or local structure changes, depending on the chromophore under investigation (such as amide groups, aromatic side-chains or protein cofactor) [45, 46]. One advantage of UVRR scattering is that the amide III region can be accessed, whereas IR spectroscopy is limited to the amide I region which overlaps with side-chain vibrations and absorption of solvent H_2O (or D_2O). Secondary structure can be reported via the intensities of resolved UVRR components of the amide III and S spectral envelopes, or by least squares fitting, over all four amide regions, with secondary structure spectra determined from crystallographically characterized protein sets [45, 46]. Time-resolve UVRR has been used to follow fast changes of overall helical structure of some α-helical peptides [47-50] or protein [51]. Slow secondary conformation change like β-sheet formation process has also been studied by time-resolved UVRR on some proteins [52, 53]. Local probing can be achieved by isotope-edited UV resonance Raman spectroscopy and has been applied to study the spatial dependence of the unfolding dynamics of the secondary structure of an alanine-based α-helical peptide which has two perdeuterated end parts and a non-deuterated center [54].

1.2.5. Optical rotatory dispersion (ORD)

ORD, which is the wavelength dependence of the orientation of a linearly-polarized light, is well-known as a determination method for the secondary structures of proteins/peptides. Recently, time-resolved ORD spectroscopy has been used to monitor the fast folding/unfolding dynamics of secondary structure of α-helical peptides [55] and proteins [56, 57]. As a quantitative technique, the change in the helical content upon the secondary structural changes can be reported [55].

1.2.6. Other techniques

Many other, more specialized methods have been applied to investigate fast folding processes of proteins (table 1.3).

Methods	Property	References
Small-angle X-Ray scattering	Scattering at the smallest angles yields the radius of gyration, providing a measure of compactness of globular proteins.	58
Magnetic circular dichroism	Optical activity is induced by the application of an external magnetic field, is particularly sensitive to the disturbance of the electronic states of a chromophore by the surrounding structure.	59
Photoacoustic calorimetry	Protein volume changes upon unfolding of proteins.	60, 61
Electron parametric resonance (EPR)	The EPR signal of a spin-labeled protein depends on their tumbling mobility and thus changes upon the formation of the protein.	62

Table 1.3 Some other, more specialized techniques used for observing fast folding process of proteins.

1.2.7. Circular dichroism: principle and its role in the determination of secondary structure of proteins/peptides

1.2.7.1. Optical activity and circular dichroism

When a molecule is optically active, it has a different refractive index for right- and left- circularly polarized light. This results in the rotation of the plane of polarization of the light. The rotation is wavelength-dependent, thus the effect is called optical rotatory dispersion (ORD). Besides, the molecule also absorbs the two polarizations of light to different extents. This is called circular dichroism (CD). When a molecule exhibits a combination of ORD and CD in the region of absorbance, then the transmitted light becomes elliptically polarized which is observed in circular dichroism.

Let consider a light wave linearly-polarized in the x direction:

$$\vec{E} = E_0 e^{i(kz-\omega t)} \begin{pmatrix} 1 \\ 0 \end{pmatrix}, \tag{1.1}$$

where E_0 is the vibration amplitude, k is the wavevector, ω is the angular speed. This linearly-polarized light wave can be analysed as a superposition of left- and right- circularly polarized light waves:

$$\vec{E} = \vec{E}_L + \vec{E}_R = \frac{E_0}{2} e^{i(kz-\omega t)} \begin{pmatrix} 1 \\ -i \end{pmatrix} + \frac{E_0}{2} e^{i(kz-\omega t)} \begin{pmatrix} 1 \\ i \end{pmatrix}. \tag{1.2}$$

By passing through an optically-active medium of thickness l, the two vibration components meet different refractive indices (n_L, n_R), where n_L and n_R are the refractive index of left- and right-circularly polarized light respectively, and different linear absorption coefficients (α_L, α_R), where α_L and α_R are absorption indices of left- and right-circularly polarized light respectively. Thus, the two transmitted vibrations have a complex phase difference of

$$\phi = \frac{2\pi}{\lambda} \left[(n_L - n_R) - i(\alpha_L - \alpha_R) \right] l , \tag{1.3}$$

where λ is the wavelength. Therefore, we obtain a complex rotation

$$\theta = \frac{\phi}{2} = \frac{\pi}{\lambda} \left[(n_L - n_R) - i(\alpha_L - \alpha_R) \right] l . \tag{1.4}$$

On the other hand, the amplitudes of the two transmitted vibration components become:

$$E_L^{'} = \frac{E_0}{2} e^{-\frac{2\pi}{\lambda}\alpha_L l} , \tag{1.5}$$

$$E_R^{'} = \frac{E_0}{2} e^{-\frac{2\pi}{\lambda}\alpha_R l} , \tag{1.6}$$

As a result, we obtain an elliptic vibration, which have the axes:

$$A = E_L^{'} + E_R^{'} , \tag{1.7}$$

$$B = E_L^{'} - E_R^{'} . \tag{1.8}$$

Hence, the ellipticity is define as

$$\psi \cong \tan\psi = \frac{A}{B} = \frac{\frac{E_0}{2}(e^{-\frac{2\pi}{\lambda}\alpha_L l} - e^{-\frac{2\pi}{\lambda}\alpha_R l})}{\frac{E_0}{2}(e^{-\frac{2\pi}{2}\alpha_L l} + e^{-\frac{2\pi}{2}\alpha_R l})}$$

$$= \frac{1 - e^{-\frac{2\pi}{\lambda}(\alpha_R - \alpha_L)l}}{1 - e^{-\frac{2\pi}{\lambda}(\alpha_R - \alpha_L)l}}$$

$$= th\frac{\pi}{\lambda}(\alpha_L - \alpha_R)l$$

$$= \frac{\pi}{\lambda}(\alpha_L - \alpha_R)l \text{ in radian.} \qquad (1.9)$$

As being defined, CD is the difference in absorption of left- and right-circularly polarized light:

$$\Delta A = A_L - A_R = \log\frac{I_0}{I_L^{'}} - \log\frac{I_0}{I_R^{'}}, \qquad (1.10)$$

where I_0, $I_L^{'}$ and $I_R^{'}$ are the intensities of the linearly-polarized incident light, the transmitted left- and right-circularly polarized components. Then, we have

$$\Delta A = \log\frac{I_R}{I_L} = \log e.\ln\frac{I_R}{I_L}$$

$$= \log e.\ln\frac{E_R^{'2}}{E_L^{'2}}$$

$$= \log e.\ln\frac{\left(\frac{E_0}{2}\right)^2 e^{-\frac{4\pi}{\lambda}\alpha_R l}}{\left(\frac{E_0}{2}\right)^2 e^{-\frac{4\pi}{\lambda}\alpha_L l}}$$

$$= \log e.\frac{4\pi}{\lambda}(\alpha_L - \alpha_R)l. \qquad (1.11)$$

On the other hand, by applying Beer-Lambert's law, CD can also expressed as

$$\Delta A = \Delta\varepsilon Cl = (\varepsilon_L - \varepsilon_R)Cl, \qquad (1.12)$$

where ε_L, ε_R are the molar extinction coefficients for left- and right-circularly polarized light respectively, C is the molar concentration and $\Delta\varepsilon$ is defined as the molar dichroic absorption coefficient. Combining two equations (1.11) and (1.12), we obtain

$$\frac{\pi}{\lambda}(\alpha_L - \alpha_R) = \frac{\Delta\varepsilon Cl}{4l.\log e}. \quad (1.13)$$

Comparing (1.9) and (1.12), one get

$$\psi = \frac{\Delta\varepsilon Cl}{4\log e}. \quad (1.14)$$

The term "molecular ellipticity" is usually used and is defined in degrees.mol^{-1}.L.m^{-1} as

$$\Theta = \frac{100\Delta\varepsilon}{4\log e} \times \frac{180}{\pi} = 3298\Delta\varepsilon, \quad (1.15)$$

where $\Delta\varepsilon$ is expressed in mol^{-1}.L.cm^{-1}.

1.2.7.2. Origin of optical activity

An electronic transition is the result of the movement of charges when electrons of a molecule are perturbed by the electric field of an electromagnetic radiation. Similarly, the magnetic field can induce a magnetic transition The optical activity associated with a transition depends on the electric dipole moment and the magnetic dipole moment induced by the action of the electromagnetic radiation on the electrons in the molecule. The rotational strength R_k of a transition is defined as the product of two vectors of the electric dipole $\vec{\mu}_e$ and the magnetic dipole times the cosine of the angle γ between the two vectors:

$$R_k = \vec{\mu}_e \vec{\mu}_m \cos\gamma. \quad (1.16)$$

If a molecule has a plane or center of symmetry, either the sum of all the induced electric and magnetic dipoles is zero, or the vectors representing the magnetic and electric dipoles are orthogonal to one another. And thus, there is no optical activity. However, there are molecules that have neither reflection plane nor symmetry center, and so the molecules are optically active and they are said to be chiral. In such cases, three phenomena may exist:

- Two transitions occur in a single chromophore, one is magnetic and one is electric. The asymmetry in the molecule perturbs the field, resulting in a symmetry breakdown in the chromophore and so the two transitions are no longer perpendicular to one another. The n-π* transition is electrically forbidden but is magnetically permitted. In

an asymmetric molecule, such a transition can have very low total absorption of light but high optical activity. This case is found in all helical polypeptides and proteins.

- Two groups have simple electric transitions. These are coupled by their proximity to produce a magnetic moment. This phenomenon is responsible for most of the optical activity of helices.
- Two chromophores are present in a single molecule. One has a magnetic transition and one has an electric transition. These are coupled in the molecule and strengthen each other.

1.2.7.3. Role of circular dichroism in the determination of secondary structure of proteins and peptides

As proteins and peptides consist of amino acid residues which are chiral molecules, they exhibit optical activity and so CD. The chromophore which interacts with light is the amide bond. Three electronic transitions are thought to occur in the range of 130-230 nm, including a weak $n\rightarrow\pi^*$ transition (210-230 nm), a strong $\pi\rightarrow\pi^*$ transition (170-195 nm), and a second, weaker $\pi\rightarrow\pi^*$ transition (135-160 nm) [63-65]. In the CD spectrum of α-helices, a weak $n\rightarrow\pi^*$ electronic transition occurs at ~220 nm while a higher frequency $\pi\rightarrow\pi^*$ electronic transition takes place at ~190 nm [63, 64]. This $\pi\rightarrow\pi^*$ transition undergoes exciton splitting that gives rise to two dipole-allowed transitions: one perpendicular to the helical axis at 190 nm and the second parallel to the axis at 205 nm. For β-sheets, the $n\rightarrow\pi^*$ transition occurs at ~217 nm regardless of strand orientation in the sheet while the $\pi\rightarrow\pi^*$ transition occurs at ~194 nm for parallel sheets and ~196 nm for anti-parallel sheets [65]. These transitions can be observed characteristically in a CD spectrum (see chapter 4 for more details). From the CD spectrum, one can extract the information on the fraction of a molecule that is in the α-helix shape, the β-sheet configuration or random coil conformation (see chapter 4 for the analysis).

Static CD measurements of the amide bond absorption in the far UV (190-230nm) have been widely used for the quantitative determination of secondary structures of proteins and peptides [66]. This field has recently known an important progress with the appearance of SRCD (Syncrotron Radiation CD) and protein secondary structure determination can be performed through websites such as DICHROWEB [67] Another advantage of CD spectroscopy is that the measurements can be performed in aqueous solution instead of heavy

water which must be done with IR spectroscopy. This makes the experiment more accessible and closer to physiological conditions of proteins.

1.3. Methods for fast initiation of peptide or protein folding

In order to be able to observe any process on a short timescale, it is essential to start the process fast enough, i.e., within the desired time resolution. The most general methods for the initiation of protein folding or unfolding are based on fast mixing techniques, in which solution conditions, such as denaturant concentration or pH, are rapidly changed from unfavorable for folding/unfolding to favorable by mixing with other suitable solutions. Since the mixing methods rely on diffusion of molecules in solutions, the experiments using these methods are normally restricted to observing processes on millisecond, or longer timescales. However, in many cases, rapid mixing measurements show indications of unresolved fast processes of protein folding occurring during a burst phase within the dead time of the measurements [68, 69]. As mentioned previously, by using molecular dynamic simulation, α-helix formation is predicted to occur on the 10-ns timescale, which is much shorter than the required time for efficient mixing of the standard rapid mixing techniques. Recently, some innovative approaches have been successful in providing initial insights into the fast processes of peptide and protein folding on short timescales (< 1 ms).

1.3.1. Rapid mixing methods

Rapid mixing is a standard method for triggering protein-folding reactions by the fast reduction of the concentration of denaturants, such as guanidine hydrochloride (GuHCl) or urea, or by a sudden change in the pH of the solution to a value more favorable for the folded protein. This technique has been widely used for the studies of protein-folding dynamics, although its time resolution is limited to the timescale of milliseconds. Two strategies have been pursued to maximize the time resolutions of these rapid mixing techniques:

- The first approach is based on turbulent flow to achieve mixing of two solutions. The purpose is to attain highly turbulent flow conditions in a small volume. One example following this strategy is designed by Regenfuss *et al.* [70]. They used a tapered outer capillary and an inner, smaller-outer diameter capillary to introduce the two flows to be mixed. The openings of the two capillaries were nearly plugged by a platinum bead. The two sample solutions were then forced to flow around the sphere at high

rate, causing fast mixing. The mixed stream then went through an observation cell where fluorescence, absorbance or resonance Raman spectrum can be obtained as a function of distance along the flow, which can be converted to time using the flow rate and volume of the cell. Using a two-dimensional UV-sensitized CCD detector can provide full temporal and spectral response simultaneously [71]. 100μs dead time can be achieved with this mixer design. The fastest time resolution reported for turbulent flow mixing is 50 μs [72]. One main advantage of this approach is the use of a large amount of sample. A number of laboratories have used a turbulent flow mixer to study the folding dynamics of horse cytochrome c [72, 73].

- Another strategy is to use microfluidic devices which are based on the principle that diffusional mixing times scale as the square of the linear dimension of the mixing volume. Short mixing times are attainable by hydrodynamic focusing, which creates a micron or submicron stream of protein solution in contact with a surrounding (sheath) stream. Because flow rates are much smaller in these cases, the flow is laminar and the sample and sheath stream do not mix. In stead, the folding/unfolding process is initiated by diffusion of denaturants/protons from the sheath flow into the central protein stream. Pollack et al. [59] has fabricated and used such a microfluidic device for the observation of fast folding dynamics of cytochrome c. This approach only consumes a very small quantity of sample and is useful for any processes that can be photochemically initiated.

1.3.2. Relaxation methods

Relaxation methods, such as dielectric relaxation, ultrasonic attenuation and ultrasonic velocimetry, rely on a rapid change of an extrinsic variable such as pressure to perturb the biological system. These methods were applied in very early researches to investigate the helix-coil dynamics of α-helical homopolymers, yielding relaxation times in the range of 10 ns to 10 μs [74, 75]. Studying the conformational relaxation of the acidic molten globule state of α-lactalbumin by using ultrasonic velocimetry, Nölting et al. [76] has indicated that the structural relaxation of the protein occurs significantly in less than 500 ns. These relaxation methods, however, only give indirect structural information on the folding dynamics of proteins.

Intra-chain diffusion is regarded as an important elementary process that determines the maximum rate at which a protein can fold [77]. Recently, triplet-triplet energy transfer between chromophores which are attached to opposite ends of a short peptide chain with purely random coil structure has been used to investigate the formation of intramolecular contact in some small peptides [77, 78]. The triplet state of one chromophore (donor) is quenched upon electron exchange during contact formation with the chromophore (acceptor) at the other peptide end. The triplet decay rate is thus identical to the rate of quenching which is also close to the rate of contact formation. Therefore, the contact formation time can be evaluated based on measurements of the lifetime of the triplet state of the chromophore "donor", which was observed to be in the range of 10-100 ns, depending on the length of the peptide chain.

1.3.3. Photochemical methods

Photochemical methods have been used early on for triggering the folding of heme proteins such as cytochromes by photodissociation of carbon monoxide (CO) from the heme cofactor or electron transfer to the heme. CO photodissociation relies on denaturant concentrations at which a reduced heme protein without a CO ligand remains folded, while the same protein with a CO ligand is unfolded. Under such conditions, fast photodissociation of CO, which occurs on a picosecond timescale, causes the protein to be unligated in its unfolded form, and then relaxes to the more stable folded structure. Upon initiation of refolding of the heme protein, peptide chain diffusion-limited ligation of the heme can be observed by following the fast changes in the heme absorbance spectrum [18, 45, 79, 80], or by using time-resolved CD spectroscopy [21] or time-resolved MCD measurements [58].

On the other hand, it can be also found that at certain denaturant concentrations, the heme proteins are unfolded in the oxidized state while remaining folded in the reduced state. Thus, electron transfer to an oxidized unfolded heme protein, which can be induced by photoexcitation of a suitable chromophore, can trigger the refolding process of the protein. However, the timescale of initiation of protein folding by this method is limited by the electron transfer time, which is less than 1 μs with freely diffusing electron donors [81]. Shorter timescales can be achieved by covalently linking an extrinsic chromophore to the protein. Protein folding initiated by electron transfer has been studied on some heme proteins [20, 81, 82].

Although these ligand dissociation or electron transfer methods are almost ideal for triggering folding processes of heme proteins on very short timescales, their application is limited to these proteins and cannot easily be extended to other types of samples. Furthermore, the folding dynamics of heme proteins which are initiated by these techniques are likely governed by ligand formation and exchange processes rather than by intrinsic protein-folding dynamics. Thus, one can not apply the conclusions from such experiments on a general protein folding problem. Besides, both methods require the presence of great amounts of denaturants, which significantly affect the folding dynamics of proteins [20, 72, 81].

1.3.4. Laser-induced temperature jumps and its role in time-resolved studies of folding/unfolding processes of proteins/peptides

Laser-induced temperature jump technique is the most versatile and simplest of the fast initiation approaches for the time-resolved studies of folding/unfolding processes of proteins/peptides. This technique relies on the thermal instability of proteins/peptides. As proteins/peptides are stable only over a limited range of temperatures, increasing temperature above the limited range will cause the proteins/peptides lose their native structure [12]. Note that in several cases, proteins can also unfold at low temperatures; this phenomenon is known as cold denaturation [83]. In many cases, the denaturation process is observed to be fully reversible and the protein refolds spontaneously upon returning to physiological temperatures. Thermodynamically, the protein ensemble exists in an equilibrium between the folded structure and unfolded conformations, which shifts with temperature. For proteins, the equilibrium shifts from completely folded to completely unfolded conformation only over a few degrees [12]. However, for shorter peptides, the transition region is usually much larger, often ranging over several tens of degrees [31, 84, 85].

A sudden increase in temperature (temperature jump), which is too fast for the protein ensemble to respond simultaneously, initially leaves the protein ensemble in a conformational distribution that does not correspond to the equilibrium distribution at the new temperature. The late response of the protein ensemble towards the new thermal equilibrium can be observed by an appropriate probe, allowing monitoring of the folding/unfolding process of the protein [12]. The use of temperature jump to displace thermodynamic equilibrium was pioneered by Czerlinski and Eigen [86] who used rapid capacitance discharge to produce

Joule heating in conducting solution within several microseconds. Faster temperature jump can be achieved by using short laser pulses which directly or indirectly heat up the solvent and enables observation of protein dynamics on very short timescales (nanoseconds, picoseconds). In indirect heating, the laser pulse energy is absorbed by an inert dye that undergoes fast internal conversion [25, 26, 87]. Direct heating can be achieved by direct excitation of weak overtone bands of H_2O near 1.5 μm or D_2O near 2 μm, which have been made routinely by Raman shifting of Nd:YAG laser pulses [4, 6] or by difference frequency generation with dye laser pulses [27]. The time resolution of temperature jump methods is determined by the time needed to achieve a homogeneous temperature increase. Vibrational relaxation of the excited modes and energy flow from a dye to the solvent occur on picosecond timescales in aqueous solution, and complete thermalization of the solvent and solute can be achieved within 10-20 ps [88, 89].

A temperature increase generally results in a relaxation dynamics which corresponds to an overall unfolding of the protein, except for the case of cold denaturation which will induce net folding. Analysis of temperature jump dynamics requires a dynamic model in order to relate the observed relaxation times to the rate constants of the model reaction. The simplest model is the relaxation between fully-folded state and completely-unfolded state. If it is the case, the equilibrium relaxation time constant τ_{rel} is determined by

$$\tau_{rel} = \frac{1}{k_f + k_u}$$

where k_f and k_u are the rate constants for folding and unfolding reactions, respectively. Therefore, the relaxation towards the unfolded protein yields the same information as the relaxation towards the folded protein. The folding/unfolding rate constants can be calculated from τ_{rel} and the equilibrium constant $K = k_f/k_u$. Relaxation dynamics of more complicated systems, which do not exhibit simple two-state equilibrium behaviour, requires more sophisticated models to be analysed [90], nevertheless, folding and unfolding relaxation still should give the same information.

Laser-induced temperature jump is currently the most widely-used initiation approach for the investigation of fast folding/unfolding processes of proteins/peptides. The major advantage of temperature jump methods that distinguishes them from the rapid mixing methods and the fast photochemical methods is that it doesn't require the presence of denaturants to trigger protein folding/unfolding and thus, the process can be observed under

native solvent conditions; this avoids any possible undesired effect on the folding/unfolding dynamics caused by the denaturants. Furthermore, laser-induced temperature jump techniques rely on temperature-induced folding/unfolding of proteins and peptides and are thus applicable to a very broad range of proteins and peptides. Finally, once again laser-induced temperature jump with the used of short laser pulses allows observation of protein-folding dynamics on very short time scales (nanoseconds, microseconds).

1.4. Outlook on the thesis

As one has learnt how important it is to understand the mechanism behind the processes of protein folding/unfolding, knowing that CD spectroscopy offers quantitative determination on the secondary structure of proteins and peptides, realizing the advantages of laser-induced temperature jump (T-jump) for the initiation of fast folding/unfolding processes of proteins and peptides, we have developed a nanosecond T-jump experiment in combination with UV-CD spectroscopy for a quantitative investigation of the folding/unfolding dynamics of proteins and peptides.

Time-resolved CD was pionneered as soon as 1985 by Prof. Kliger [91] who demonstrated the potentiality of the technique by monitoring conformational changes in carboxy-myoglobin with a 50 ns time resolution. Prof. Simon then improved the time resolution down to 80 ps [92]. In recent years, demonstration of sub-picosecond CD measurements was carried out in the Laboratory for Optics and Biosciences [93]. Other similar time-resolved techniques have also been developed: optical rotation dispersion, magnetic circular dichroism, linear dichroism... A recent review is given in [94]. Recently, several groups have developed time-resolved CD spectroscopy with broadband sources which allow the simultaneous measurement of a complete CD spectrum with a very high resolution [95].

In all these studies, triggering of the conformational change was performed by photochemical methods such as the photodissociation of carboxymyoglobin. However, these techniques are limited to specific proteins and not well adapted to the study of protein folding. On the other hand, as we have seen above, T-jump experiments provide a very efficient way to mimick denaturation processes in peptides or proteins in their physiological environment. We have therefore decided to mix these techniques and to measure the CD in the far UV after a T-jump excitation. This thesis contains six chapters:

- Chapter 1 has been written as an introduction to protein-folding problem and the tools that have been used to solve it.
- Chapter 2 describes experimental details that we have developed and experienced to build up a nanosecond T-jump/CD experiment.
- Chapter 3 introduces our temperature jump measurements as well as our calculation for applying temperature jump approach to study proteins/peptides unfolding in our experiment.
- Chapter 4 investigates the unfolding dynamics of poly (α-L-glutamic) acid using our T-jump/CD experiments. From our T-jump measurements, information on the change in helical fraction of the peptide has been extracted. Furthermore, the results have been compared with those obtained from Dr. Volk's T-jump/IR measurements (University of Liverpool, UK).
- Chapter 5 presents our work in the course of our collaboration with Dr. Volk to study the folding dynamics of a coiled-coil dimmer, measured by Volk's T-jump/IR measurements.
- Chapter 6 describes a picosecond time-resolved CD experiment and our results obtained from studying a fast photoinduced reaction on a putative photoreceptor protein involved in the photophobic response of Blepharisma japonicum. Our results demonstrate the local geometrical changes that accompany this process.

CHAPTER 2

EXPERIMENTAL DETAILS

This chapter presents experimental details on our temperature jump experiments which allow a quantitative observation of the helix-coil dynamics of α-helical peptides. The idea is to combine the use of a temperature jump with probing of the change in circular dichroism of these peptides in the far UV, where the secondary structures reveal with characteristic CD features. The CD feature, which shows up at 220 nm, is commonly used to estimate the α-helical content of proteins. By measuring the variation of circular dichroism of a polypeptide, one obtains the variation of the helical fraction in the peptide.

In order to heat up water with nanosecond pulses, two strategies can be employed. One can use indirect heating where a dye [26] excited by the second harmonic of the laser serves as heat transducer. Alternatively, one can directly heat the water solvent using IR laser pulses. The latter method yields less cavitation problems [2], but demands a nanosecond IR source whereas the former one is directly implementable with a Nd:YAG laser. We have therefore carried out a series of test on the indirect mechanism that we will present in the next section.

However, considering the experimental problems with indirect heating, we have finally decided to buy a nanosecond OPO directly operating in the infrared. The two laser sources needed to carry out a CD/T-jump experiment are then presented. On the one-hand, one needs a nanosecond IR source to induce the temperature jump, hereafter called the "pump". On the other hand, a UV source compatible with the detection of the CD is necessary (the "probe"). Finally, electronic synchronization of the two sources and of the various detection apparatus is necessary.

2.1. Temperature jump set-up

2.1.1. Choice of the heating mechanism

Because indirect heating is much cheaper, we have started considering this mechanism for our T-jump experiment. This indirect heating is the result of the following steps:

- Dye absorption of laser pulses.
- Fast internal conversion of photon energy into vibrational energy.
- Vibration relaxation and heat diffusion into the surrounding.
- Uniform temperature heat diffusion (in pumped volume) during laser pulse duration (100 ps).
- Temperature stability in the pumped volume (1 ms).

One of the drawbacks of this indirect heating technique is the bleaching of the dye which is used as an intermediate for energy transfer. As far as we know, gold nanoparticles give the possibility of absorption at the Nd:YAG wavelength of 532 nm. The need for understanding of the photostability of these compounds to choose an appropriate material is one of the first requirements for a T-jump experiment.

2.1.1.1. Photostability measurements for Fuchsin dye and gold nanoparticles

We have studied two samples: the Fuchsin dye and gold nanoparticles. Both compounds have a strong absorption around 530 nm and release rapidly their heat to water after excitation. Fuchsin in the form of powder was dissolved in double-distilled water (pH = 8.45) to get a 3 mM fuchsin solution. The solution was then diluted to get a 0.075 mM solution with a 0.56 optical density was achieved. Gold nanospheres suspended in water was fabricated following Turkevich et al. method [96, 97].

In order to measure the photostability, sample is irradiated by a Nd:YAG laser at 532 nm wavelength. Green light coming out of the laser is split into two beams, one is for reference and the other will be sent to the sample. The two beams are then directed to two photodiodes, of which the two signals will be treated by two averagers and modulated by a module card which is connected to a computer. The averagers and module card are triggered by an electrical signal from the laser.

After several measurements on photostability of fuchsin and gold nanoparticles, one can conclude that gold nanoparticles show very promising photostability over fuchsin dye. Under irradiation of Nd:YAG laser with a 27 mW power, fuchsin exhibits a continuous slow degradation over time with a 13.2 hour time constant at room temperature and a dramatic soaring of transmission signal with a 5.2 minute time constant at 52°C. Although gold nanoparticles undergo some small changes in transmission at the beginning of laser irradiation, they show up a good stability after four hours with the same laser power. One can also notice that the changes of gold nanoparticles due to laser irradiation take longer time at higher temperature. Actually, in order to use such gold nanoparticles in T-jump experiment, they should be irradiated during 4 hours at room temperature and at least 1 hour at 52°C before use so that one can expect a good stability.

Unfortunately, the Turkevich method provides charged nanoparticles which interact with polypeptides. Mixing these particles with a peptide instantaneously resulted in the appearance of a precipitate. To correct for this effect, one should use capped nanoparticles, which are much more complicated to produce. Furthermore, even though gold nanoparticles display good stability properties, the indirect heating remains prone to cavitation problems.

2.1.1.2 Direct heating set-ups

In view of the aforementioned difficulties, we decided to go for a direct heating apparatus. Several possibilities exist to generate IR pulses from a Nd;YAG laser:

- Raman shifter: by passing the Nd:YAG pulse through a cell containing a gas, its wavelength is shifted because of Raman effect.
- Dye laser: A Nd:YAG laser can be used to pump a dye laser. A further difference frequency stage yields IR pulses.
- Nanosecond OPO's. Several possibilities exist for Nd:YAG pumped OPO's. They can be based on PPLN or on BBO crystals.

We have had the opportunity to buy a commercial nanosecond OPO which is very convenient. We will now present the laser systems in details.

2.1.2. Pump laser system

Our pump laser system is based on a nanosecond frequency-doubled Nd:YAG laser (GCR4, Spectra-Physics). The active medium is a rod of neodymium-doped yttrium aluminium, which is pumped by a flash lamp that emits white light. Excited electrons quickly drop to the upper level of the lasing transition, where they remain for a relatively long time-about 230 s. The most probable lasing transition is connected with an emission of a photon at 1064 nm, because afterwards electrons quickly relax to the ground state and a population inversion is easily created. The Nd:YAG laser is designed to limit oscillation to 1064 nm light. An electro-optic Q-switch is employed to prevent oscillation, and therefore, the population inversion is built up high. At the point of maximum population inversion, the Q-switch is switched to transmission mode by a fast high-voltage pulse, allowing the energy stored in the medium to be converted into a high intensity pulse of < 10ns duration. The active medium is placed in a resonant cavity, where the pulse intensity is greatly amplified by stimulated emission. The Q-switched pulse passes through a SHG (second harmonic generation) crystal where the 1064 nm light interacts with the crystal to produce 6ns pulse at 532 nm with a repetition rate of 30 Hz and an energy of 550 mJ.

Most T-jump experiments based on an IR probe necessitate the use of deuterated water and require IR pulses at 1.9 μm. Such is not the case in our set-up where we deal with a UV probe and our samples are dissolved in H_2O. In that case, the IR wavelength necessary to heat up water is about 1.5 μm, which corresponds to the excitation of the $\nu_1+\nu_3$ overtone mode of H_2O. Absorption at this wavelength is 32 cm^{-1}, a weak absorption which allows uniform heating of the sample.

In order to reach IR wavelengths, the 532 nm light beam is used to pump a commercial nanosecond OPO (GWU, Spectra-Physics) where 532 nm photons are converted into signal-idler photon pairs through second-order nonlinear optical interactions with a β-BaB_2O_4 (beta-barium borate or BBO) crystal [98]. For reasons of energy conservation, the relation

$$\nu_p = \nu_{sig} + \nu_{idl},$$

where ν_p, ν_s and ν_i are the frequencies of the pump, signal and idler beams respectively, must be held. The signal and idler wavelengths, which are determined by a phase-matching condition, can be varied in a wide range of 690-2300 nm. In order to obtain the idler

wavelength of 1.454 μm, the signal wavelength is precisely tuned to 839 nm. The OPO delivers up to 8 mJ pulses at 1.454 μm (idler) with a duration of 5 ns.

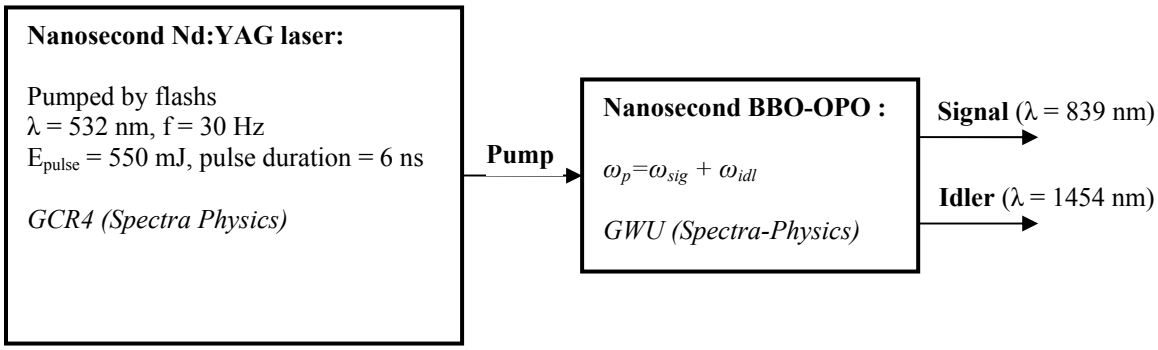

Figure 2.1 Description of the nanosecond laser system used to induce temperature jump.

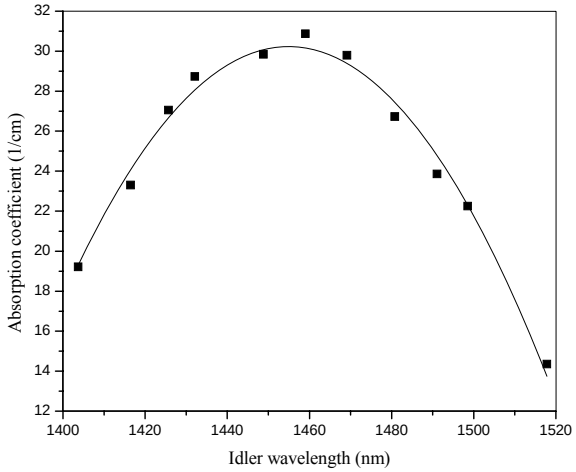

Figure 2.2 The $\nu_1+\nu_3$ overtone band of H_2O with maximum absorption at 1.454 μm. Measurement taken in a sample of distilled H_2O with a 100 μm path-length cell using a PbSe photodiode. A polynomial fit is also shown.

A description of our nanosecond system which is used to induce temperature jump is shown in figure 2.1.

The idler wavelength of 1.454 μm is chosen for a maximum water absorption (figure 2.2) measured by a PbSe photodiode.

2.1.3. Probe laser system

The probe pulse must be tunable in the far UV, especially around 220 nm where the ratio CD/absorption is the greatest. We use a sub-picosecond source based on a 1 kHz amplified Titanium-Sapphire system followed by several stages of BBO based optical

parametric amplification and frequency-mixing. This source delivers 40nJ pulses tunable between 220 and 350 nm.

2.1.3.1. 1kHz Titanium-Sapphire laser system

The schematic representation of our 1 kHz Titanium-Sapphire system is depicted in figure 2.3. The principle of this laser system can be briefly described as follows:

- A crystal rod of titanium-doped sapphire is placed in a cavity of an oscillator. It is pumped by a continuous solid laser with a wavelength of 532 nm and produces a large emission spectrum centered at 800 nm. The cavity of the oscillator is designed to allow all the longitudinal modes included in the spectrum and a self-mode-locking regime that is based on the optical Kerr effect induces these modes to be synchronized in phase [99]. This mode-locked oscillator generates ultra-short pulses tunable between 700 and 950 nm with a duration of 100 fs and a repetition frequency of 82 MHz. The pulse wavelength is normally tuned close to 800 nm where the maximum gain and laser efficiency are obtained.
- These pulses are sent to a regenerative amplifier [100] which is pumped by a nanosecond solid laser with frequency-doubled pulses at 527 nm and a pulse repetition of 1kHz. Before passing through the amplifier medium which contains a crystal of titanium-doped sapphire, the pulses are chirped and temporally stretched to a much longer duration by a factor of 10^3 to 10^5 by means of a grating pair (the stretcher). This reduces the peak power to a level that is sufficiently low compared with the intensity limit of gigawatts/cm^2, to avoid serious damage to the gain medium through nonlinear processes. After the gain medium, another grating pair (the compressor) is used to remove the chirp and temporally compress the pulses to a duration similar to the input pulse duration.

This laser system provides pulses with a duration of 150 fs, a repetition rate of 1kHz and an energy of about 0.4mJ. Such laser beam is intense enough for latter nonlinear optic processes.

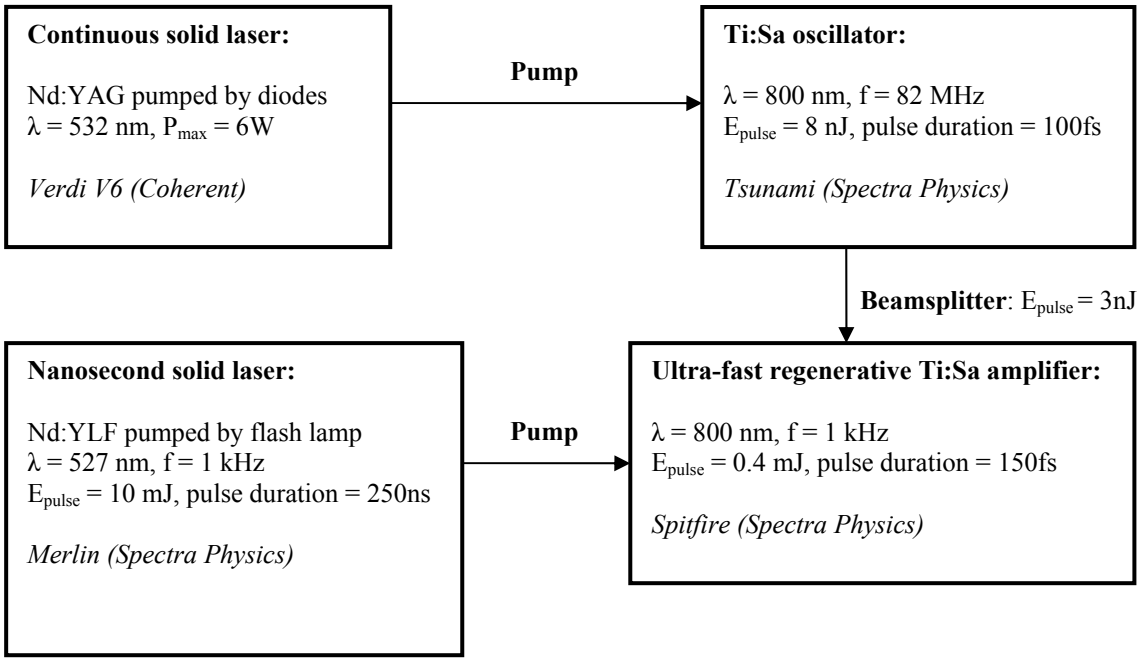

Figure 2.3 Schematic representation of the 1 kHz Titanium-Sapphire system

2.1.3.2. Generation of tunable UV pulses

In order to convert the 800 nm light into a tunable UV light, several intermediate stages of BBO based optical parametric amplification and frequency-mixing are required and described in this section:

- White-light generation from the 800 nm light
- An optical parametric amplification stage that amplifies the visible wavelengths of the continuum
- A sum frequency generation stage to attain tunable UV pulses

2.1.3.2.1. White-light generation

White-light generation by focusing femtosecond laser pulses with several microjoules of energy into a transparent condensed medium is a well-known and often-used nonlinear optics effect. There are several complex mechanisms such as Raman effect, Brillouin effect and self-phase modulation that have been introduced to explain this phenomenon.

The starting point is the self-phase modulation: According to optical Kerr effect, when passing through a medium, an intense ultra-short pulse *I(t)* can induces a change in refractive index of the medium

$$n(I) = n_0 + n_2 I \tag{2.1}$$

$$\text{with } I(t) = I_0 \exp(-t^2/\tau^2), \tag{2.2}$$

where we suppose that the pulse has a Gaussian form with a full width at half maximum τ, where n_0 is the linear refractive index of the medium, and n_2 is the second-order nonlinear refractive index.

We obtain the instantaneous phase $\phi(t,z)$ of the electric field of the pulse

$$\phi(t,z) = -\varpi_0 t + \frac{\varpi_0}{c} n(I) z, \tag{2.3}$$

where ϖ_0 is the central frequency of the pulse and z is the path length that the pulse travelled in the medium. In the same manner, one can write the instantaneous frequency

$$\varpi(t,z) = -\frac{\partial \phi(t,z)}{\partial t} = \omega_0 - \frac{\omega_0}{c} n_2 \frac{\partial I(t,z)}{\partial t}. \tag{2.4}$$

Note that in the case of a pulse with a Gaussian profile, the instantaneous frequency becomes

$$\varpi(t,z) = \varpi_0 - \frac{\partial}{\partial t}\left[\frac{\omega_0}{c}\frac{2n_2 z}{\tau^2} I_0 \exp(-t^2/\tau^2)\right]. \tag{2.5}$$

Hence, the instantaneous frequency is red (blue) shifted on the leading (trailing) edge of the pulse. As a result, new frequencies are created with central frequency ϖ_0, leads to superbroadening of the spectrum. It is the phenomenon of self-phase modulation behind the formation of continuum spectrum. This resulting continuum spectrum is interesting for us because it allows us to select one wavelength from the spectrum for latter process of optical parametric amplification.

In our case, we use a Sapphire crystal with a thickness of 1 cm for the generation of a continuum spectrum. The resulting spectrum extends to the visible domain from the original infrared spectrum. An attenuator is inserted to vary the intensity of the infrared beam focusing onto the crystal. This enables the control of the stability of the continuum spectrum, ensuring a stability of the whole nonlinear optics system.

2.1.3.2.2. Optical parametric amplification

Optical parametric amplification (OPA) is a phenomenon of second-order nonlinear optical interaction. Its principle is illustrated in figure 2.4. OPA allows us to select and amplify a wavelength from the continuum.

Figure 2.4 Principle of optical parametric amplification.

The focalization of a faint "signal" beam and an intense "pump" beam into a same point on a nonlinear crystal with correct alignment induces an amplification of the "signal" beam and generation of another beam called "idler".

Following the law of energy conservation, we have

$$\nu_p = \nu_s + \nu_i , \tag{2.6}$$

where ν_p , ν_s and ν_i are the frequencies of the pump, signal and idler beams respectively.

The amplification of the signal beam depends not only on the intensity of the pump but also on the characteristics of the crystal (material, thickness) and the alignment which needs to be in good agreement with two important conditions:

- Phase-matching: $k_p = k_s + k_i$. When the condition is respected, the waves stay in phase while propagating in the crystal and constructively interfere.
- Group velocity matching: $\vec{v}_{g,p} = \vec{v}_{g,s}$. It requires the pump and signal beam to propagate with the same velocity in superposition in the crystal for an effective energy exchange.

Note that in all cases from now on, the *p, s* and *i* indices represent the pump, signal and idler beams.

In our case, we use a BBO crystal pumped by a 400 nm light beam (SHG of the 800 nm infrared beam) for amplifying the wavelengths of the continuum. Here, we are put in the case of type I phase matching, in which the pump and signal need to be polarized along the extraordinary and ordinary axes respectively. Note that our OPA stage is made with non-

collinear geometry - i.e., the directions of the pump and signal beams are separated by an angle $\alpha(\lambda_p, \lambda_s)$.

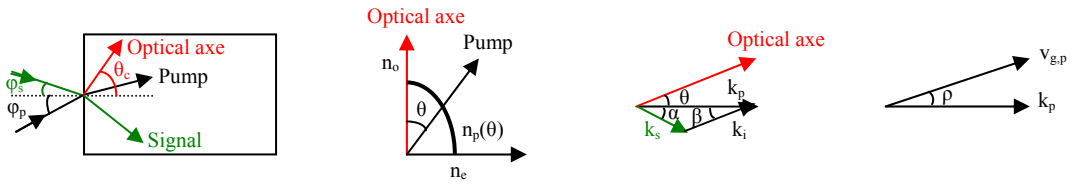

(a) (b) (c) (d)

Figure 2.5 Optical parametric amplification in non-collinear geometry: (a) Geometric description of pump and signal beam with respect to the optical axis of the crystal. (b) Index ellipsoid. (c) Phase matching condition. (d) Walk-off effect on the direction of the group velocity.

The determination of $\alpha(\lambda_p, \lambda_s)$ for improving the efficiency of the amplification stage was introduced in previous theses [93, 101]. To begin with, we define some angles which are represented in figure 2.5:

- Phase-matching angle θ between the direction of the wave vector $\vec{k}_p$ of the pump and the optical axis of the crystal
- Ordinary (extraordinary) index n_o (n_e) of the BBO crystal
- Angle β between the direction of the idler beam and the direction of the pump beam
- Walk-off angle ρ, which is the angle between the direction of the wave vector $\vec{k}_p$ of the pump and the direction of its Poynting vector. It is expressed as a function of θ:

$$\rho(\theta) = Arc\tan\left(\frac{n_{o,p}^2}{n_{e,p}^2}\tan\theta\right) - \theta\,. \tag{2.7}$$

When it is not compensated in the case of type I phase matching, the pump and signal beams, with a diameter d, do not overlap beyond a distance $L = d / \tan\rho$.

In the case of type I phase matching, the direction of the group velocity $\vec{v}_{g,p}$ deviates from the direction of the $\vec{k}_p$ vector (extraordinary wave) by the ρ angle while $\vec{v}_{g,s}$ is collinear with the $\vec{k}_s$ vector (ordinary wave).

Knowing that the idler is also polarized along ordinary axis, with the help of the schemas in figure 2.5, a system of equations can be written as:

$$\frac{n_{o,s}}{\lambda_s}\sin\alpha = \frac{n_{o,i}}{\lambda_i}\sin\beta\,, \tag{2.8}$$

$$\left(\frac{n_p(\theta)}{\lambda_p}\right)^2 = \left(\frac{n_{o,s}}{\lambda_s}\right)^2 + \left(\frac{n_{o,i}}{\lambda_i}\right)^2 + \frac{2n_{o,s}n_{o,i}}{\lambda_s\lambda_i}\cos(\alpha+\beta), \quad (2.9)$$

$$v_{g,s}\cos\alpha = v_{g,s}\cos(\rho(\theta)), \quad (2.10)$$

$$1 = \frac{n_p(\theta)^2\sin^2\theta}{n_{e,p}^2} + \frac{n_p(\theta)^2\cos^2\theta}{n_{o,p}^2}, \quad (2.11)$$

where 2.8 and 2.9 are the projections of the phase matching condition onto horizontal and vertical axes, 2.10 is the projection of the group velocity matching onto the horizontal axis and 2.11 is the expression of the $n_p(\theta)$ of the pump in index ellipsoid.

This system of equations is easily solved by Matlab. We obtain the values of θ and α angles for each wavelength of the continuum. Knowing the value of θ_c angle between the optical axis of the crystal and the normal to polished faces of the crystal (30°C in our case), we can deduce the angle of incidence φ_s of the signal beam and φ_p of the pump beam on the crystal:

$$\varphi_s = \pm Arc\sin(n_{o,s}\sin(\theta+\alpha-\theta_c)), \quad (2.12)$$

$$\varphi_p = \pm Arc\sin(n_{e,p}\sin(\theta_c-\theta)), \quad (2.13)$$

where the + sign corresponds to the case of $\theta < \theta_c$ and $\theta+\alpha > \theta_c$.

The phase matching and group velocity matching conditions can not be simultaneously verified, however, the optical parametric amplification can be optimized by choosing the θ and α angles as follows:

- $\theta \cong 30°(\pm 10°)$: phase matching is verified for each wavelength of interest and over a band large enough for the amplification of 150fs pulses.
- $\alpha \cong 4°$: the walk-off angle is compensated, ensuring a good spatial superposition of the pump and signal beams. The amplification can be reinforced with the help of a thick crystal (2 mm in our case).

2.1.2.2.3. Generation of a tunable UV probe

The schema in figure 2.6 represents different stages of nonlinear optics that allows us to reach UV domain. There are three main stages:

1. The first stage generates a continuum from 800 nm light by using a sapphire crystal of 1cm thickness.
2. The second stage provides optical parametric amplification of a chosen wavelength of the continuum in non-collinear geometry that has the configuration described in the previous paragraph. It uses BBO 2 crystal and a pump beam of wavelength of 400nm, generated by frequency-doubling of an 800nm beam with BBO 1 crystal. The chosen wavelength can be shortened or lengthened with the help of a mirror mounted on a micrometer translation stage. The wavelengths that can be selected and amplified lie between 490 nm and 650 nm.
3. The final stage with the help of BBO 3 crystal makes sum frequency generation of a UV beam by mixing the amplified wavelength by the stage of optical parametric amplification and a 400 nm beam produced by frequency-doubling of an 800nm beam with BBO 4 crystal. The resulting beam is tunable between 220 nm and 245 nm.

Calling (o) the common ordinary axis of all the BBO crystals and (e) the extraordinary axis, the first one is orthogonal to the plane of the figure 2.6 and the second one is in the plane. Knowing that the 800nm beam coming out of the commercial system is polarized along the ordinary axis:

- Type I phase matching is verified in the BBO 1 and BBO 4 crystals: $2\vec{k}_{800}^{(o)} = \vec{k}_{400}^{(e)}$.
- For the stage of optical parametric amplification in the BBO 2 crystal, we have $\vec{k}_{400}^{(e)} = \vec{k}_{visible}^{(o)} + \vec{k}_{idler}^{(o)}$.
- The sum frequency generation in the BBO 3 crystal verifies the type I phase matching: $\vec{k}_{400}^{(o)} + \vec{k}_{visible}^{(o)} = \vec{k}_{UV}^{(e)}$, where the polarization of the 400nm beam is tuned by a $\lambda/2$ plate.

We obtain a probe beam tunable between 220 nm and 245 nm and polarized in the plane of the figure.

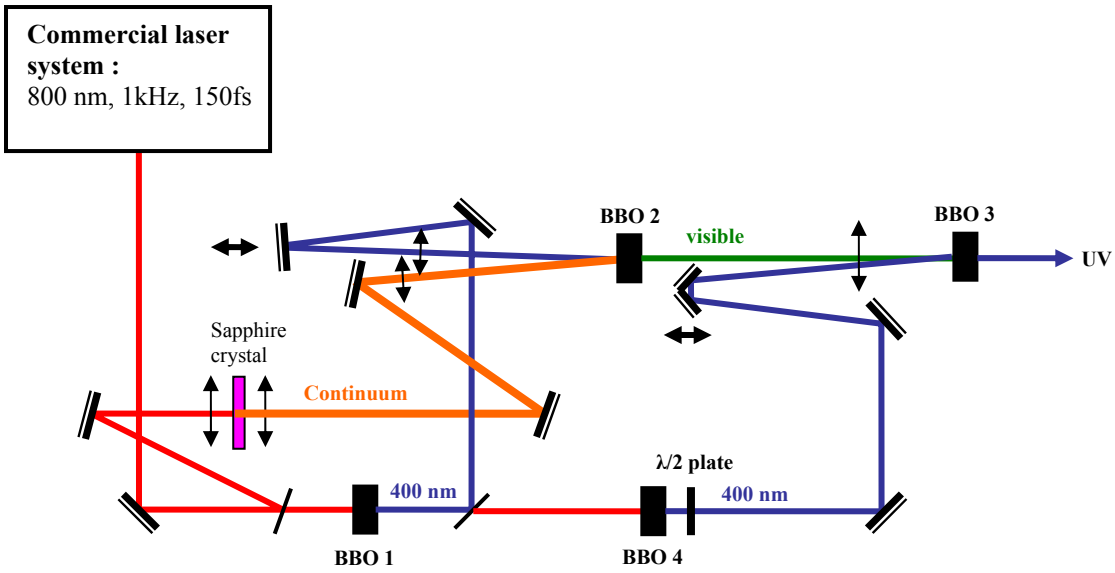

Figure 2.6 Schematic representation of different stages of nonlinear optics for the generation of a tunable UV probe.

2.1.4. CD/T-jump experimental set-up

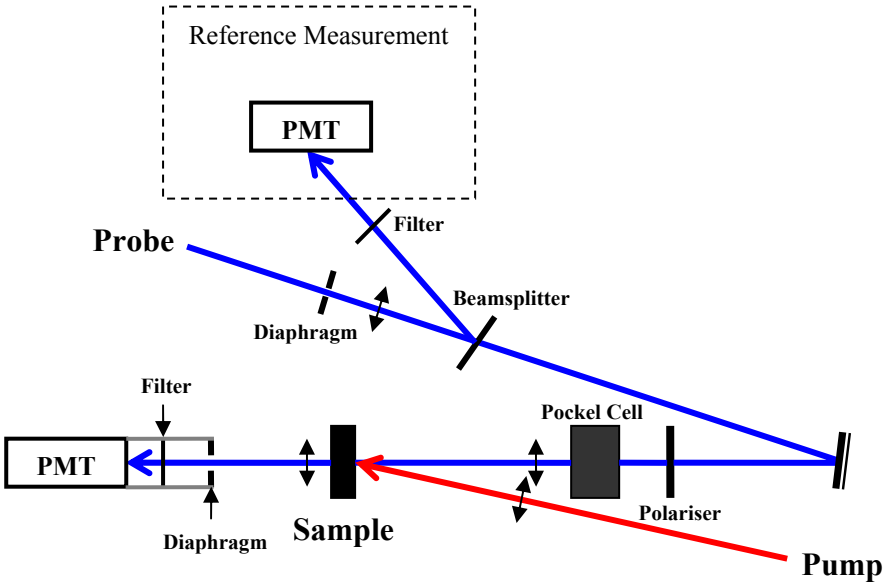

Figure 2.7 Schematic representation of our CD/T-jump experimental set-up.

Figure 2.7 illustrates our CD/T-jump experimental set-up which corresponds to a classical pump-probe experiment. Both pump and probe pulses are focused onto the sample with 100 mm focal length lenses. In order to measure CD, the probe beam is sent through a polarizer and a longitudinal KD*P Pockels cell (Gsänger LM8) whose axes are oriented at 45° with respect to the incident polarization [92]. An alternate voltage (± 600 V) is applied to the Pockels cell to transform the linear probe polarization into right or left circular polarization.

After a preliminary alignment of the Pockels cell with the help of the isogyre pattern (Maltese cross), fine alignment as well as adjustment of the applied voltage is carried out by inserting a quarter-waveplate and a crossed analyzer after the Pockels cell and optimizing the contrast between the two circular polarizations. The transmitted probe intensity is focused by a lens onto a photomultiplier tube (PMT, Electron Tubes 9402) and a gated integrator/ Boxcar averager system (Stanford SR250). In order to reduce the effects of laser fluctuations, we carry out normalization of the signal by a reference signal which is measured by the same type of PMT. An interference filter with a peak wavelength of 220 nm and a FWHM of 10 nm is put in front of the photocathode of each PMT. Moreover, to improve the linearity of the signal normalization, a diaphragm with a small aperture (~2 mm in diameter) is placed before the beamsplitter which is inserted on the probe part at the beginning for creating a reference beam. To avoid thermal lensing effect, a diaphragm which is bound to the entrance of the PMT is kept opened. The signals are processed with a personal computer which controls all the experimental parameters.

We have also estimated the size of the beams. The pump diameter is about 500 μm whereas the probe one is about 80 μm, ensuring that the probe sees a transversely uniform temperature profile.

2.1.5. Precise alignment of pump and probe beams

When making a temperature jump measurement, it is essential to have an optimum spatial overlap of the pump and probe beams. This is to ensure that the sample volume being probed is homogeneously heated, and thus, the probe sees a transversely uniform temperature profile.

This can be achieved by first obtaining the diameter of the pump beam at the focus in the sample is at least three times larger than that of the probe beam. As presented in previous section, the pump diameter at the focus is about 500 μm which is about six times larger than the probe diameter of 80 μm.

The next step is then to find and optimise the pump/probe beam overlap. With the help of a 200 μm pinhole mounted on a micrometer translation stage and placed at the sample position, this procedure is simply accomplished. First, the pinhole is adjusted to find the probe beam through it. After that, the pinhole is put so that the probe beam goes into the middle of the pinhole. This is done by monitoring the intensity of the probe measured by the PMT. Finally, the pump

beam is optimized through the pinhole by adjusting a lens and looking at transmitted intensity detected by a PbSe photodiode.

2.2. Electronic synchronization

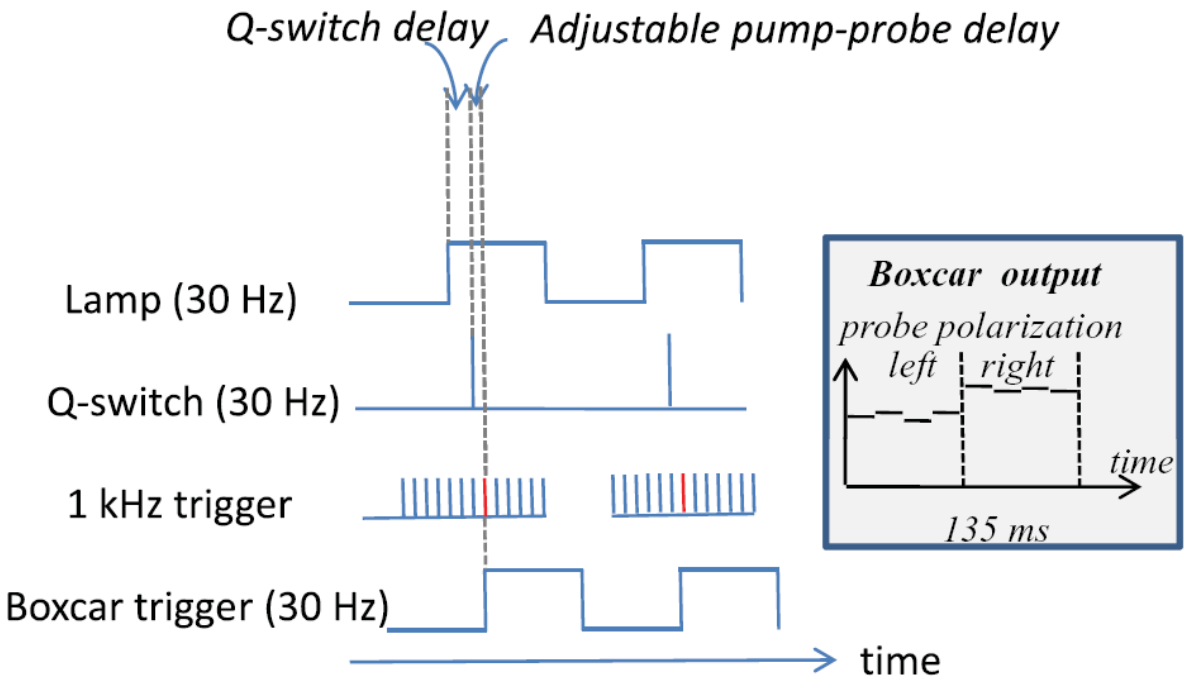

Figure 2.8 Triggering signals generated by the synchronization electronics. Two variable delays are generated: the Q-switch delay and the adjustable pump-probe delay. The inset schematically describes the Boxcar output signal when the Pockels cell voltage is modulated at 3.7 Hz.

A major issue of our T-jump experimental set-up is the electronic synchronization of the lasers and of the detection devices. A sophisticated system of synchronization electronics have been developed based on a complex programmable logic device (CPLD – Lattice) with a great help of our electronic workshop (Xavier Solinas's work). An electronic board whose behaviour is described in VHDL has been designed using the 82 MHz Titanium-Sapphire laser oscillator as external clock. The parameters for the timing of the various signals are dynamically transferred through the RS232 interface of the personal computer which controls the acquisition processes and data analysis. Five triggering signals are generated, which are depicted in figure 2.8. First, two 30 Hz signals are used to trigger the Nd:YAG laser. The first one triggers the laser flash lamps, whereas the second one triggers the Q-switch. The delay between these two pulses is chosen equal to 210 μs for an optimum functioning of the laser. Then, a 1 kHz trigger is provided to the Titanium-Sapphire amplifier. The delay between the

Q-switch trigger and this 1 kHz signal is the crucial point of the device. It allows us to vary the pump-probe delay for the experiment up to 1 ms. Longer delays can be easily accessed thanks to the probe pulse train where pulses are separated by 1 ms. As depicted in figure 2.8, a 30 Hz pulse train impinging on the sample can be picked out of the 1 kHz probe pulse train with a fixed delay that can be chosen negative or positive with a resolution of 12.1 ns. Two other triggers are generated by the synchronization electronics. First, a 30 Hz signal is created in perfect synchronization with the probe pulse train relevant for the experiment. This signal is used to trigger the boxcar gate for signal detection. Second, the 30 Hz signal is divided by 8 in order to obtain a 3.7Hz signal which are used to modulate the Pockels cell voltage (not shown in figure 2.8). As a result, four probe pulses have right circular polarization followed by four pulses with a left polarization. The output of the boxcar is schematically depicted in the inset of figure 2.8.

2.3. Measurement of circular dichroism

2.3.1. Principle of the technique

Once the polarization-modulated probe beam passes through the sample, its intensity becomes modulated due to the CD:

$$I_{\pm} = Ke^{-(\alpha_0 \pm \delta\alpha)L} \approx Ke^{-\alpha_0 L}[1 \mp \delta\alpha L], \tag{2.12}$$

where K is a constant, α_0 is the mean absorption coefficient, L is the path length and $\delta\alpha$ describes the CD: absorption coefficient for a left (*resp*. right) polarization is $\alpha_0 + \delta\alpha$ (*resp*. $\alpha_0 - \delta\alpha$) and the CD is equal to $2\delta\alpha L$. From this expression, one obtains:

$$CD = \frac{I_- - I_+}{(I_+ + I_-)2}. \tag{2.13}$$

The $\frac{(I_+ + I_-)}{2}$ term is directly accessible through the signal detected by the Photomultiplier tube (PMT signal). The problem is to measure $I_- - I_+$.

2.3.2. Three detection schemes

Three complementary manners have been developed to measure this intensity difference. The first idea is to use a lock-in amplifier (LI) locked on the Pockels cell modulation. This is the most straightforward technique and from the LI signal, one measures

CD as 2.2LI/PMT (the 2.2 factor being due to the square modulation imposed on the signal). However, due to the weakness of the modulation and the small modulation frequency (3.7 Hz), sorting out the signal from noise requires extensive averaging. Another possibility is to measure I_+ and I_- independently and to calculate the difference with the computer after averaging. Identification of these two intensities is made possible by sending the 3.7 Hz modulation signal to the acquisition card. Finally, we have also tried to perform Fast Fourier Transform of a series of 4096 data. The resulting spectrum clearly displays a peak corresponding to the modulation frequency, whose amplitude gives the magnitude of the CD.

These three techniques have been implemented in the same software and simultaneous measurements have been carried out with the three techniques. For a given acquisition time, the three techniques yield very similar results (see figure 2.9). Having the three results together allows us to confirm the reality of the signal and to improve our signal-to-noise ratio.

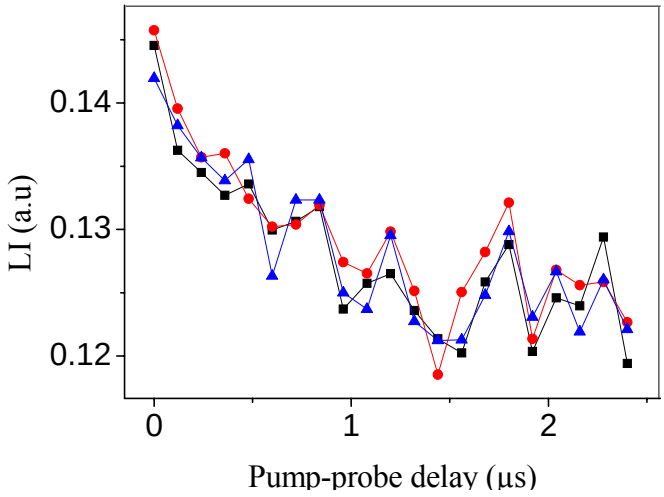

Figure 2.9 LI values obtained by: (black line) using a lock-in amplifier, (red line) calculating the intensity difference $I_- - I_+$ with the computer and (blue line) performing Fast Fourier Transform of a series of 4096 data.

2.4. First experimental set-up and unsolvable artifacts

Before ending this chapter, we would like to address another issue. In some previous works (see chapter 6), we had implemented a very original manner to measure time-resolved CD by utilizing a linearly-polarized probe and measuring the pump-induced ellipticity with a Babinet-Soleil compensator (BS) [102]. A schema of the set-up is shown in figure 2.10.

The linearly-polarized probe beam is sent through the sample and then is passed through the BS compensator and a crossed-analyzer. The probe transmission is measured by a photomultiplier tube (PM signal) and the signal is integrated by a Stanford SR250 boxcar. Same normalization procedure like being said in section 2.1.3 is taken.

However, measuring the time-resolved CD with the technique turned out to be impossible in our T-jump experiments. The reason for this is that with this latter technique, some artifacts can occur in presence of birefringence. Usually, birefringence is not pump-sensitive and does not preclude using this technique. However, in our T-jump experiment, it appears that the very rapid temperature change in the cell provokes a transient birefringent feature on the few microsecond timescale which completely masks the CD signals. The polarization modulation technique that is employed at last and presented in previous paragraphs has the great advantage that it is insensitive to sample birefringence to a large extent.

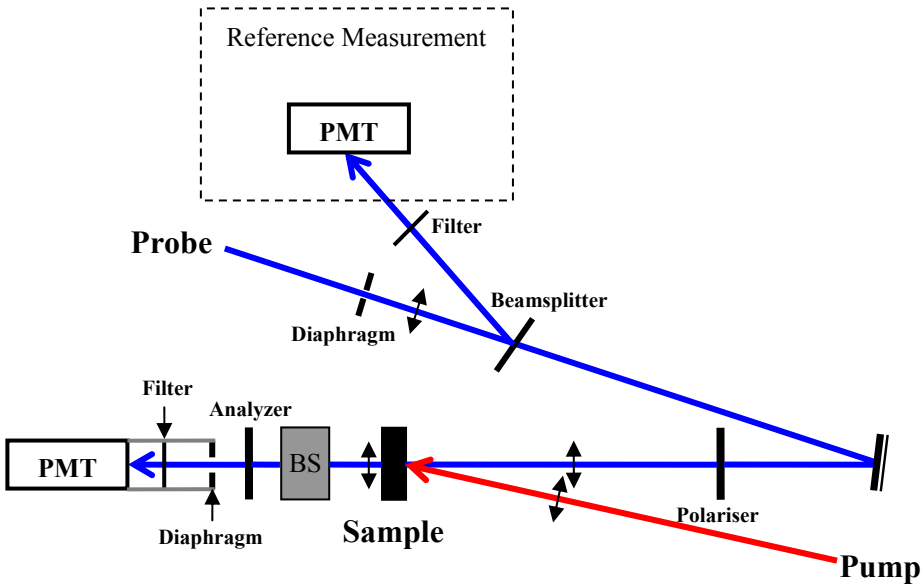

Figure 2.10 Schema of our first CD/T-jump experimental set-up that utilizes a linearly-polarized probe and measures the pump-induced ellipticity with a Babinet-Soleil compensator (BS).

We want now to give a more precise account of the effects of birefringence on the CD measurements.

In order to do so, we use the Jones matrix formalism: the electromagnetic field is defined by a column vector (corresponding to the two polarization directions) and each optical

element is described by a 2x2 matrix. The output beam is then given by the product of the 2x2 matrix by the column vector:

$$E_{out} = M_{opt.el.} E_{in}. \tag{2.14}$$

We are interested in the circular dichroism which is the difference in absorption for a right or a left circular polarization. Such circularly-polarized beams are defined as

$$E_{in} = \frac{1}{\sqrt{2}} \begin{bmatrix} 1 \\ \pm i \end{bmatrix}, \tag{2.15}$$

where the sign '+' (*resp.* '–') stands for the right (*resp.* left) circular polarization. A chiral sample displaying a weak optical rotation and circular dichroism is described by

$$M_{sample} = e^{-\frac{\alpha L}{2}} \begin{bmatrix} 1 & i(\eta - i\theta) \\ -i(\eta - i\theta) & 1 \end{bmatrix}, \tag{2.16}$$

where α is the mean absorption coefficient, L the sample thickness, $\eta = (\alpha_L - \alpha_R)L/4$ is proportional to the CD and $\theta = \pi(n_L - n_R)L/\lambda$ is responsible for the optical rotation.

With these definitions, one obtains for the circular polarized beams

$$E_{out} = \frac{1}{\sqrt{2}} \begin{bmatrix} 1 \\ \pm i \end{bmatrix} (1 \mp (\eta - i\theta)). \tag{2.17}$$

As expected, the polarization of E_{out} is still perfectly circular, only its intensity and phase are modified. The corresponding intensities are

$$I_{out} = 1 \mp 2\eta \tag{2.18}$$

and we recover: $CD = I_L - I_R = 4\eta = (\alpha_L - \alpha_R)L$.

Let us now suppose that the optical beam encounters some linear birefringence. This birefringence can have many origins. It can be static, due to mechanical strain in the lenses or the cell windows for example, or dynamical if it is induced by the pump beam which heats up the sample inhomogeneously. If we suppose that this birefringence is weak, the general matrix reads

$$M_{LB} = \begin{bmatrix} 1 & ibsin2\gamma \\ ibsin2\gamma & 1 \end{bmatrix}, \tag{2.19}$$

where $2b \ll 2\pi$ is the induced retardation and γ the angle between the fast axis and the laboratory frame. After passing through the birefringent device and the chiral sample, the electric fields are:

$$E_{out} = M_{LB} M_{sample} E_{in}, \tag{2.20}$$

$$E_{out} = \frac{1}{\sqrt{2}}\begin{bmatrix} 1 \mp bsin2\gamma \\ \pm i(1 \pm bsin2\gamma) \end{bmatrix}(1 \mp (\eta - i\theta)). \tag{2.21}$$

As a first consequence, one can see that the output beam is no longer perfectly circularly polarized. However, to the first order in b, η and θ, its intensity is still

$$I_{out} = 1 \mp 2\eta, \tag{2.22}$$

which indicates that in this configuration, the birefringence does not perturb the CD measurement.

This feature is crucial for our experiment and we would like to stress that it is so because there is no polarization device after the sample. In many other experimental techniques such as the Babinet-Soleil one that we have developed or the one proposed by the Kliger group, there is a crossed polarizer between the sample and the detector. The detected electric field is therefore

$$E_{detected} = \begin{bmatrix} 0 & 0 \\ 0 & 1 \end{bmatrix} E_{out} = \frac{1}{\sqrt{2}}\begin{bmatrix} 0 \\ \pm i(1 \pm bsin2\gamma) \end{bmatrix}(1 \mp (\eta - i\theta)) \tag{2.23}$$

corresponding to an intensity $I_{detected} = \frac{1}{2}(1 \pm 2(b - \eta))$. In that case, one can see that the birefringence occurs at the first order and will directly concurrence the measurement of the CD.

This simple calculation allows us to stress the insensitivity of our measurement technique to birefringence to a large extent. Note however that the above calculation is valid only for weak birefringence effects. This feature has proved to be very important in the T-jump experiment where we have observed that the pump induced a transient birefringence effect in the cell. It was therefore very important to get rid of this artifact signal in order to sort out the dynamics of the CD from the dynamics of the induced birefringence.

This insensitivity is due to the absence of any polarization device between the sample and the detection [103]. As soon as a polarizer or any other polarizing device is introduced, birefringence becomes a crucial issue.

CHAPTER 3

TEMPERATURE JUMP MEASUREMENTS

3.1. Introduction

Measuring temperature jump is an important part and the first step of any temperature jump measurement. As temperature jump techniques rely on the strong temperature dependency of the folding/unfolding dynamics of proteins and peptides, it is of extreme importance to accurately quantify the size of the temperature jump.

This chapter presents firstly an estimation of the temperature jump in our experimental conditions, secondly our simulation work on calculation of temperature jump as well as its following evolution in a sample cell, and thirdly our method and measurements to determine the size of the temperature jump.

3.2. Estimation of the temperature jump

We can estimate the temperature jump from the energy deposited by the IR pump into the sample. Let us call E_0 the incident pump pulse energy. The amount of energy absorbed by the sample is

$$E_{abs} = E_0(1 - e^{-\alpha L}), \tag{3.1}$$

where α is the absorption coefficient and L the sample thickness. This absorbed energy provokes a rise of temperature given by

$$E_{abs} = mC_{Water}\Delta T, \tag{3.2}$$

where m is the mass of the water excited by the pump and $C_{Water} = 4.136$ J/kgK is the heat capacity of water. We can calculate the mass of water from its volume $V = L \times S$ where S is the beam surface.

In our experiment, the pulse energy is at most 8 mJ and the beam diameter is about 500 µm, corresponding to a surface $S = 5 \times 10^{-7}$m^2. The absorption coefficient is $\alpha = 32$ cm^{-1}. In Table 3.1, we calculate the temperature jump as a function of the sample thickness L..

L (µm)	**ΔT** (°C)
10	**7.8**
100	**6.7**
1000	**2.4**

Table 3.1 Temperature jump as a function of the cell thickness.

It is interesting to note that the thicker the cell, the smaller the temperature jump. This feature can be easily understood: when one increases the thickness, the water volume increases proportionally whereas the absorbed energy scales sublinearily with $(1 - e^{-\alpha L})$. As a result, one sees that it is important to choose a very thin cell to carry out the T-jump experiment. In our case, we have chosen a 100 µm cell which is still very efficient and which is more tractable and commercially available.

3.3. Simulation of the temperature jump

In order to be able to predict and understand the evolution of temperature inside our cell, a Matlab program have been written by Lucille Mendonça based on simple heat transfer theory following Wray *et al.* [104]. The principle of the calculation is to divide our cell in small ring cells indexed by (*i,j*) for the *r* and *z* directions, where *z* corresponds to the direction of the pump beam (see figure 3.1), compute the thermal flux between cells and the temperature *T* of the cell at each calculation step.

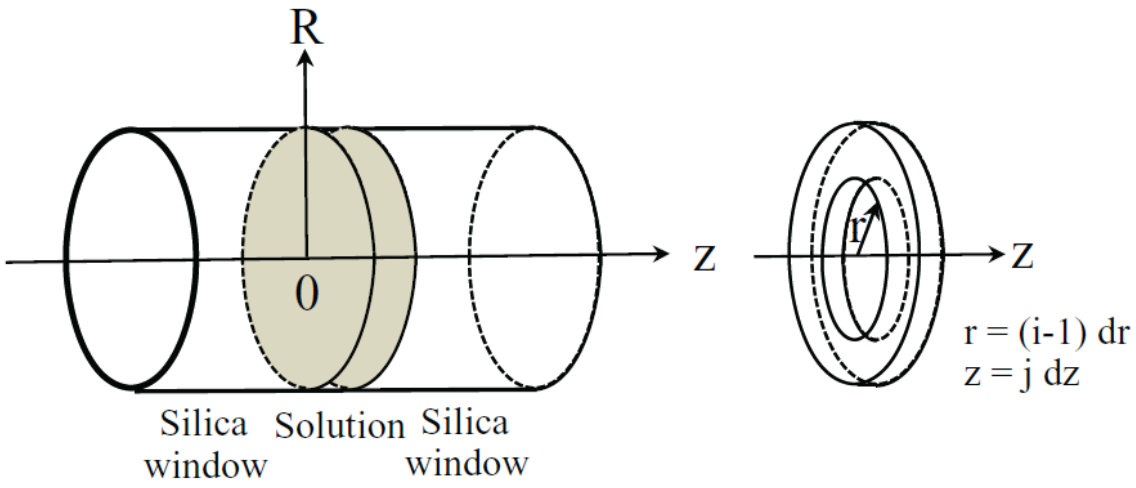

Figure 3.1 Sketch of the elementary cell used in the temperature jump simulation.

Using the Fourier law:

$$j = \lambda \nabla T = -\lambda \left(\frac{\partial T}{\partial r} e_r + \frac{\partial T}{\partial z} e_z \right), \tag{3.3}$$

where ***j*** is the thermal flux and λ is the heat conductivity, we can write the heat energy exchanged during time interval dt along the r and z directions between cells i and $i+1$ and between cells j and $j+1$, respectively, as:

$$Qr_{i,j} = \lambda 2\pi i dr dt \frac{T_{i+1,j} - T_{i,j}}{dr}, \tag{3.4}$$

$$Qz_{i,j} = -\lambda \pi (2i-1) dr^2 dr \frac{T_{i,j+1} - T_{i,j}}{dz}. \tag{3.5}$$

The temperature after a time dt can be written using the first principle of thermodynamics applied to a cell (i,j):

$$T_{i,j} = T_{i,j} + \frac{Qr_{i-1,j} + Qz_{i,j-1} - Qr_{i,j} - Qz_{i,j}}{C\pi (2i-1) dr^2 dz}, \tag{3.6}$$

where C is the volumetric heat capacity of the material of cell (i,j).

In the calculations, the thermal parameters are applied for our cell: λ_{water} = 0.5984 $W.K^{-1}.m^{-1}$, C_{water} = 4.136×10^6 $J.m^{-3}.K^{-1}$, λ_{silica} = 1.4 $W.K^{-1}.m^{-1}$, C_{silica} = 1.408×10^6 $J.m^{-3}.K^{-1}$. When the heat transfer takes place between a water cell and a silica one, the average value of λ is used.

We have considered a 500 µm pump beam, a 100 µm path length cuvette, 0.5 mm of silica for the cuvette windows and a 5°C T-jump starting at 20°C. Absorption of the pump light in water was also taken into account ($\alpha = 32 cm^{-1}$).

In order to see if the temperature remains constant on a long enough time scale for the peptide dynamics to be seen after a pump pulse, a calculation has been performed for 0.1 s following a single pump pulse. The results are shown in figure 3.2. The average temperature along the z axis in the solution decreases only slightly in the first millisecond, whereas cooling takes place between 1 and 100 ms. Figure 3.3 displays the temperature profile within the cell. As expected, cooling of the water is due to heat exchange with the cell window. We see that the temperature remains constant for about 100 µs and cools on the time scale of 10 ms. This cooling effect is efficient on timescales larger than 100 µs, a very long time compared to our peptide dynamics (see chapter 4).

Finally, we have studied the cumulative heating of the solution due to the 30 Hz pump repetition rate. Calculating the time evolution of the temperature for 3s with a pump period of 30ms, we found that the background temperature in the middle of the cell can increase by more than 5 degrees after 2 s of irradiation with the pump beam for a 1 mm thick cell. Continuously rotating the cuvette at a certain speed could avoid this cumulative heating up of the solution (see next section).

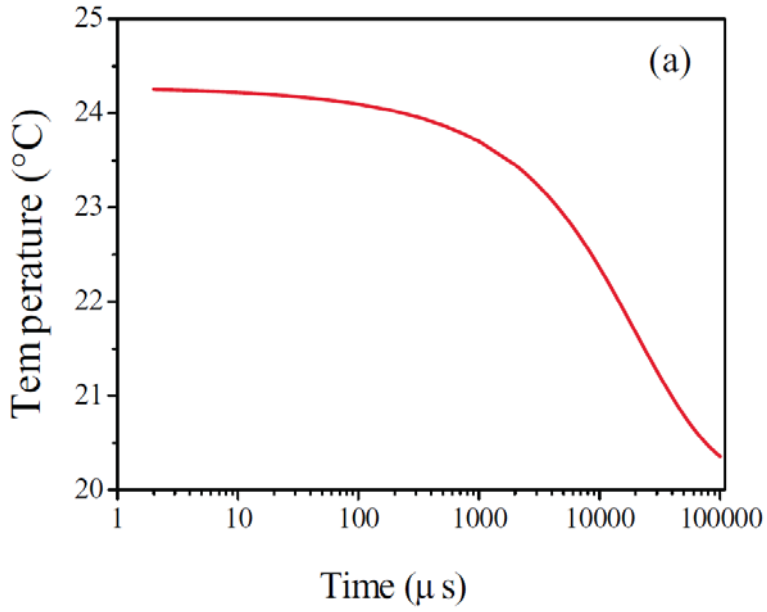

Figure 3.2 Evolution of the mean temperature with time for a 100 µm pathlength cell with silica windows, assuming an instantaneous initial T-jump of 5°C in the first layer of the sample from an initial temperature of 20°C.

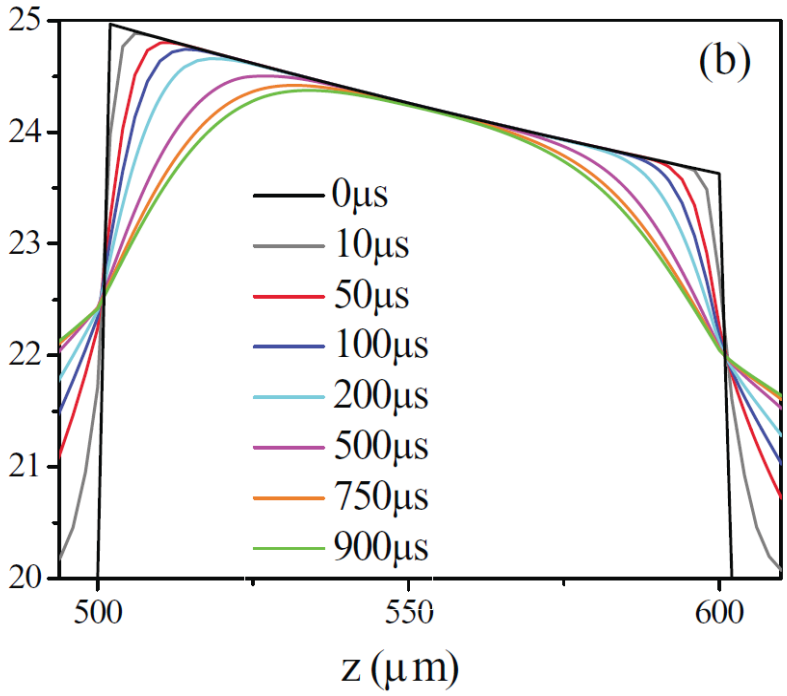

Figure 3.3 Temperature profile in the sample (and adjacent window volume) along the beam path for different delays after the T-jump.

3.4. Temperature jump measurements

Measuring *in situ* the temperature increase of the sample is a crucial issue for a temperature jump experiment. Such a measurement is usually directly obtained by monitoring the absorption change of water in the infrared [2, 6, 27, 31, 32]. However, we don't have this possibility here since we work with a probe delivering pulses in the visible or in the UV. We have therefore developed another technique allowing the precise measurement of the temperature jump and its dynamics in our experimental set-up. Similar techniques have been proposed in references [113] and [105].

3.4.1. Choice of a temperature indicator

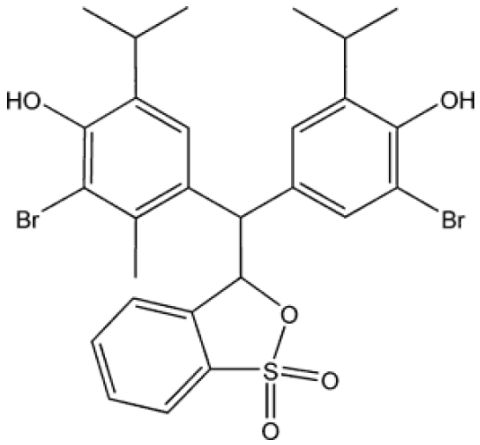

Figure 3.4 Bromothymol Blue in acid form.

Because absorption in the visible or the UV is usually not very sensitive to temperature, we have to use some intermediate temperature-dependent process. One such process is the strong dependence of some buffers on temperature. This effect, which is a source of problems for chemists, is very well documented and we have chosen the Tris-HCl buffer. At a pH of 7.2 at room temperature, the pH changes by –0.028/°C with temperature. Such pH changes are easily observable with colored pH indicators. In our case, we expect the pH to change from 7.2 to 6.7 when temperature increases from 21 to 41°C. We have therefore utilized the pH indicator Bromothymol Blue (figure 3.4), whose pH sensitivity is in the 6.2-8.2 range. We use a saturated solution of Bromothymol Blue in TrisHCl buffer (pH = 7.2).

3.4.2. Temperature jump calibration

Our next task is to calibrate temperature with the sample of saturated solution of Bromothymol Blue in TrisHCl buffer (BBT) as the temperature indicator. The absorption spectra of the solution as a function of the temperature are displayed in figure 3.5a. One can see that the absorption of BBT is strongly temperature-dependent with maximum absorption change at 615 nm (figure 3.5b).

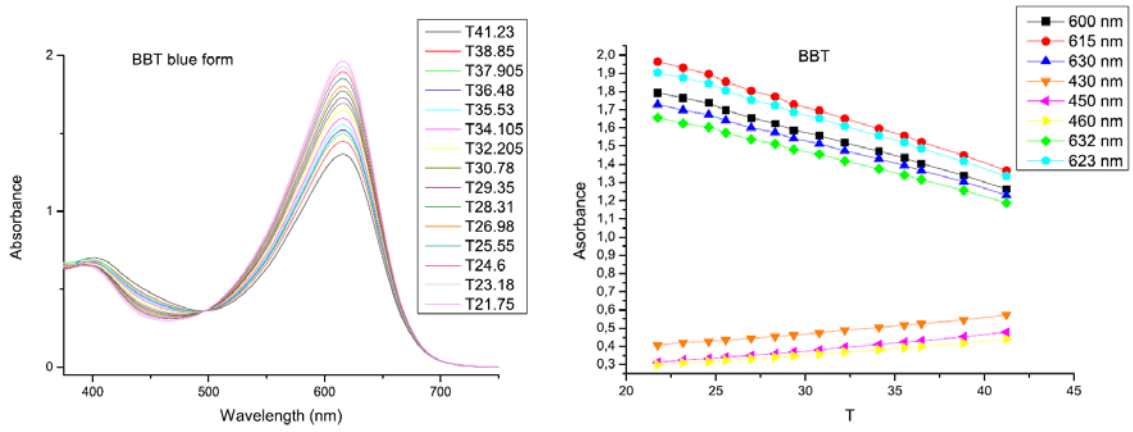

a) b)

Figure 3.5 a) Temperature-dependent spectra of a saturated solution of Bromothymol Blue in TrisHCl buffer (pH = 7.2). b) Absorbance as a function of temperature T (°C) of the BBT sample at different considered wavelengths.

The absorption curves as a function of temperatures can be fitted to a straight line, which has gradient corresponding to the absorbance change per degree centigrade. Thus, as the absorbance at each temperature is calculated by

$$A = -\log\left(\frac{I}{I_0}\right), \tag{3.7}$$

where I_0 is the transmission at each temperature when there is no sample and I is the transmission of light after passing through the sample at the same temperature, we can deduce the change in temperature from the change in absorption:

$$\Delta T = \frac{-\log\left(\frac{I_{afterT-jump}}{I_{beforeT-jump}}\right)}{\frac{dA}{dT}}, \tag{3.8}$$

where $I_{beforeT\text{-}jump}$ and $I_{afterT\text{-}jump}$ are the transmission signal observed before and after the sudden change in temperature induced by the pump from a starting temperature and $\frac{dA}{dT}$ can be obtain from the slope of the linear fit of the absorption as a function of temperature.

We chose to work at 623 nm where we measure

$$\frac{1}{A_{623}}\frac{dA_{623}}{dT} = (-0.0169 \pm 0.0025)T/°C, \tag{3.9}$$

where A_{623} is the absorbance of BBT at 623 nm and T is the starting temperature.

3.4.3. Temperature jump measurements

The set-up used for measuring the size of the T-jump is described in figure 3.6. Both pump and probe pulses were focused onto the BBT sample with 100 mm focal length lenses. The pump beam properties corresponded to those of the pump beam of the CD experiment described in chapter 2 with a pump energy of ~ 8 mJ/pulse and a 500 µm beam focus. The probe beam wavelength was tuned to 623 nm. In order to obtain 623 nm light, we only needed to use two first stages of the three nonlinear stages of the probe beam generation system which is described in chapter 2 (see figure 3.7). The transmitted probe intensity was focused by a lens onto a photomultiplier tube (Philips, type RTC XP2233B). The transmitted signal was then averaged by the gated integrator/ Boxcar averager system . Normalization of the signal was done with the help of a reference beam which is measured by another photomultiplier tube. An interference filter with a peak wavelength of 623 nm and a FWHM of 18 nm is placed in front of each PMT.

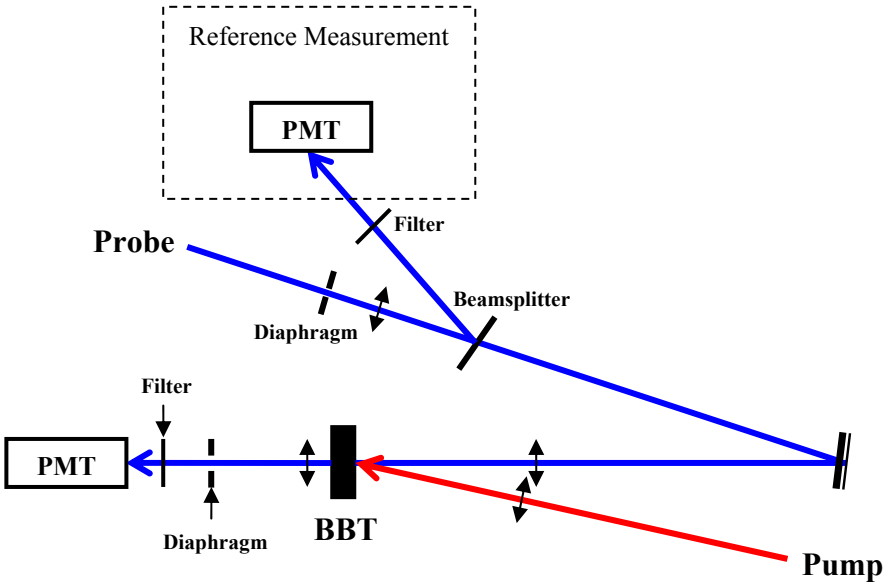

Figure 3.6 Schematic representation of our set-up for temperature jump determination.

We have performed T-jump experiments on the saturated solution of Bromothymol Blue in TrisHCl buffer at 20°C and followed in time the change in transmission of the solution at 623 nm and deduced the temperature increase using equation (3.7). First tests were carried out on a 1 mm-thick cell. The T-jump does not exceed 2°C in this configuration as expected from the simulations.

An important issue is to know the effect of the heat accumulation due to the high repetition rate of the pump laser. We have measured a temperature offset which results from these cumulative effects of 9°C. To correct this effect, we have implemented a rotation of the cell. Figure 3.8 displays the temperature offset as a function of the rotation speed. One can see that the temperature offset decreases when the motor tension increases. Therefore, we chose to work with the motor tension of 12.5 V which corresponds to 300 rpm rotation speed.

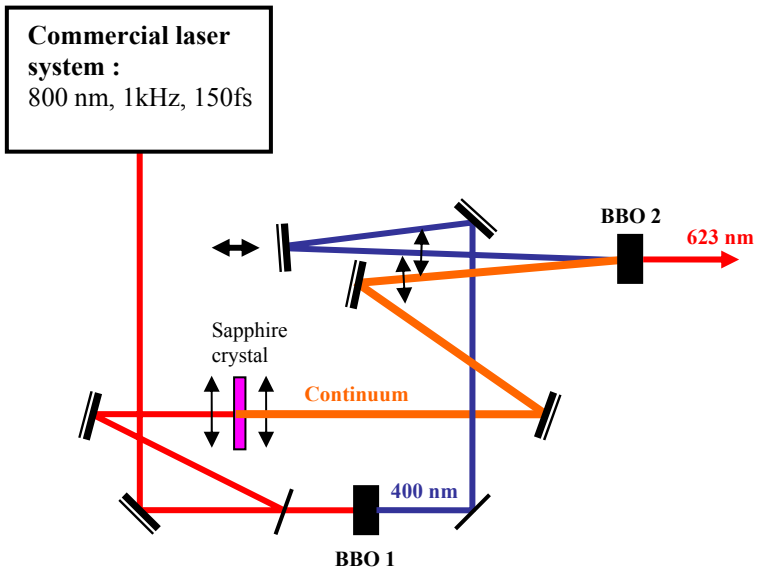

Figure 3.7 Schematic representation of different stages of nonlinear optics for the generation of a 623 nm light beam.

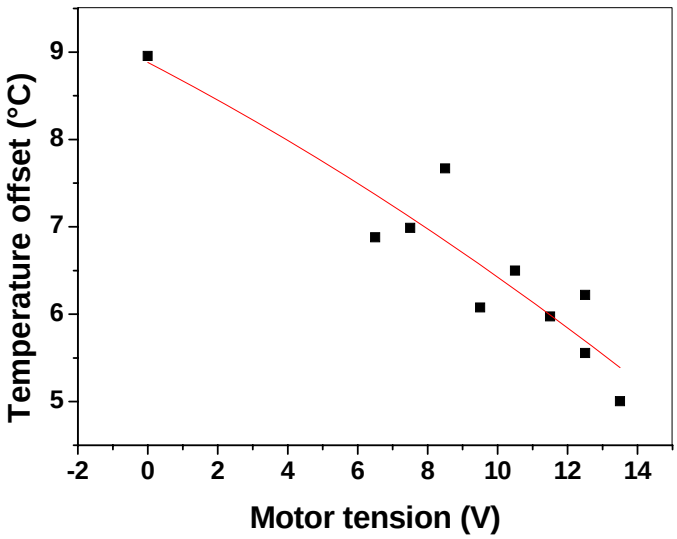

Figure 3.8 Heat accumulation effect as a function of motor tension in a 1 mm pathlength silica cell induced by multiple IR laser pulses, measured using the transient absorbance of a saturated solution of Bromothymol Blue in TrisHCl buffer at 623 nm. Red curve is the polynomial fit of the data.

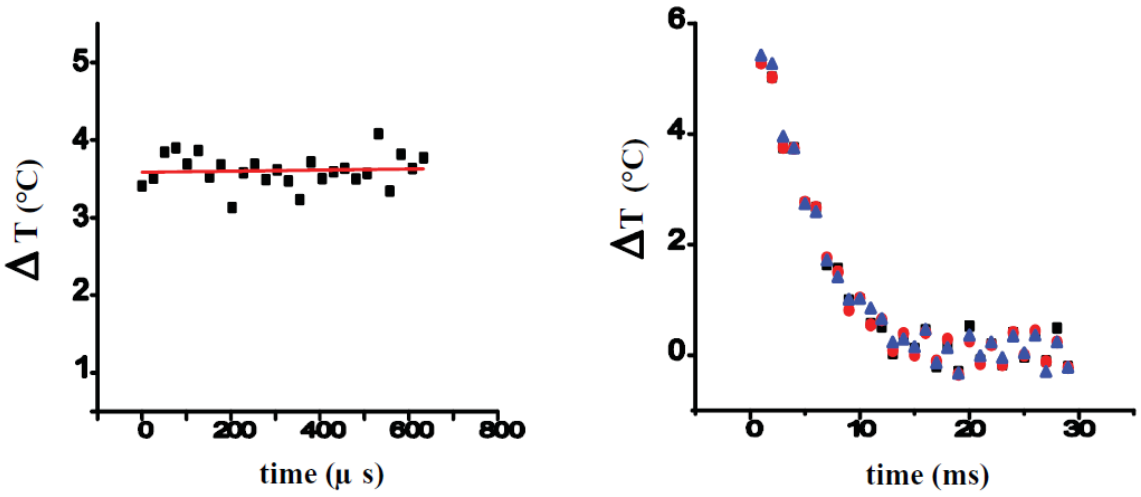

a) b)

Figure 3.9 Short (a) and long (b) time scale evolution of the temperature in a 100 µm pathlength silica cell rotated with 300rpm speed following an IR laser pulse induced T-jump, measured using the transient absorbance of a saturated solution of Bromothymol Blue in TrisHCl buffer at 623 nm. Note that the T-jump amplitude is lower on the left-hand side figure because of a lower pump power.

The temperature offset is furthermore strongly reduced when one uses a thinner cell. Indeed, in that case, heat can flow more easily through the windows. With the 100 µm pathlength quartz cell that we use for the CD experiment, we don't observe any temperature offset when the cell is rotated at 300 rpm.

Figure 3.9 shows the temperature change as a function of time for two relevant timescales when the sample cell was rotated at 300 rpm. Note that the T-jump amplitude is lower on the left-hand side figure because of a lower pump power: the pump power for the measurement on the short time scale is 220 mW whereas the one with long timescale measurement is 240 mW. One observes that the temperature jump remains constant on the time scale of a few hundred microseconds, ensuring that the dynamics that we could observe on this timescale come from the peptide and not from the cooling of the water. On the other hand, the temperature increase completely relaxes between two pump pulses separated by 33 ms, discarding any cumulative effect. This feature confirms the efficiency of rotating the cell in our experiment. Finally, we measure a maximum temperature jump of 5°C with our experimental conditions, a convenient value for carrying out unfolding experiments.

We would like to stress two interesting characteristics of our set-up. We utilize a silica cell instead of a CaF_2 cell, as usually used in IR-detected T-jump experiments, since we have no need for infrared transparence. Because silica has a lower heat conductivity, we observe a slower decay of the water temperature. As seen in figure 3.9, the temperature remains

constant over more than 800 µs, much longer than the 200 µs timescale observed for CaF_2 [2]. This can be an advantage for measuring longer processes. Furthermore, we did not observe any cavitation effect, a convenient feature for experiments. We think that it is a consequence of the direct heating, which allows measurements in the absence of dye molecules which tend to aggregate and act as nucleation sites for cavitation [2].

3.5. Conclusion

Our temperature jump measurements have proved the efficiency of the rotation of the cell in diminishing the cumulative heating in the cell. A 300 rpm rotation speed has been chosen and a maximum T-jump of 5°C has been obtained with a 500 µm pump beam focus and a pump energy of 8mJ/pulse in a 100 µm pathlength quartz cell. Following the evolution of the change in temperature in short time scale after the temperature jump, we observe a constant temperature on the time scale of hundreds of microseconds, allowing monitoring of folding/unfolding dynamics of proteins and peptides from tens of nanosecond to hundreds of microsecond timescale.

CHAPTER 4

HELIX-COIL DYNAMICS OF POLY(α-L-GLUTAMIC ACID)

4.1. Introduction

This chapter presents results of our CD/T-jump experiments on a Poly (α–L-glutamic acid) (PGA) sample that is used as an example to study the helix-coil transition in peptides/proteins. The schematic representation of poly (α-L-glutamic acid) with charged side chains is shown in figure 4.1.

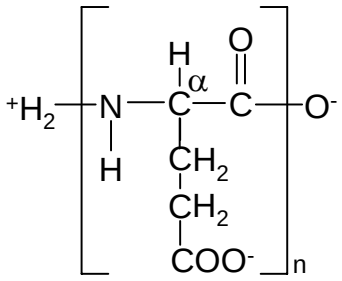

Figure 4.1 Schematic representation of Poly (α-L-glutamic acid).

The stability, helix-coil transition and dynamics of PGA have been extensively investigated by means of intrinsic viscosity [106], potentiometric titration [107, 108], optical rotation, optical rotatory dispersion [106, 109], IR/time-resolved IR spectroscopy [110, 111] and CD spectroscopy [111]. As reported, the conformation of PGA is highly dependent on pH and ionization strength of solvants [106-109]. This dependence is due to the charged state of the ionisable side chains of PGA. Highly protonated PGA is predominantly α-helical in

aqueous salt solution, whereas the fully charged state is randomly coiled [108], since at fully-charged state, the electrostatic repulsion between the negatively-charged glutamic acid side chains prevents the formation of an α-helix and favors random coil structure. In the transition region (pH ~ 5-6), PGA is partially in an α-helix and partially in random coil structure. Reducing the pH of the sample provokes the protonation of the side chains and weakens the repulsion force between them, leading to the peptide adopting an α-helical structure. For example, in 0.1 M salt, PGA is random coil at pH 6.4, almost fully helical at pH 4.5 and is about 50% helical at pH 5.1 according to optical rotation spectroscopy and potentiometric titration criteria [107, 108]. Diminishing the ionization strength of the solvent causes the pH-dependent helix-coil transition to shift to higher pH [107]. Along with pH and ionization strength dependencies, the conformation of PGA also changes with temperature [109-111]. As temperature increases, the equilibrium of the helix-coil transition shifts to the random coil configuration. At pH 5, the helix-coil transition of PGA occurs at a transition temperature of 34°C [111]. The helix-coil dynamics of PGA has been suggested to be largely independent of the motions of its side chains [112]. In addition to helix-coil transition, PGA undergoes irreversible phenomena with changes in temperature and pH. There have been proposed two discernible processes: aggregation, favored above 40°C and precipitation, favored below 20°C [109]. Both phenomena increase with decreasing pH of the sample.

In this chapter, we show the results of our CD/T-jump experiments which allow us to attain quantitative information on the helix-coil dynamics of PGA in aqueous solution. As mentioned previously in chapter 1, in addition to providing quantitative measurements on the helix-coil dynamics of α-helical peptides, possibility of carrying out the measurements in H_2O instead of D_2O is another advantage of CD spectroscopy over IR spectroscopy. Moreover, we also compare our results of CD measurements on the helix-coil dynamics of PGA with the results from time-resolved IR experiments.

4.2. Sample preparation

Poly(glutamic acid) PGA with a molecular weight of 64000 (determined by means of viscosimetry as reported by the supplier), corresponding to about 500 residues per peptide, was purchased from Sigma-Aldrich. The peptide was dissolved in an aqueous solution of 0.18M acetic acid and 0.12M sodium acetate without further purification with a concentration of 20 mg/mL, which corresponds to 0.155 M in terms of glutamic residues. The pH of the

sample was carefully adjusted to 4.7 (measured with a PHR-146 Micro Combination pH electrode and a Jenco Model 60 Portable Digital pH Meter) where the conformation of the peptide was expected to change with temperature.

The peptide is placed into a 100µm-path-length quartz cell (Hellma) which can be thermalized by external water circulation. In order to avoid cumulative effects due to the pump, the cell is continuously rotated at 300rpm rotation frequency.

4.3. Results and discussions

4.3.1. Steady-state temperature-dependent absorption measurements

Absorption spectrum of an α-helix in the range of 130-240 nm includes three electronic transitions such as a weak n→π* transition (~220 nm) and two dipole-allowed π→π* transitions: one perpendicular to the helical axis (~190 nm) and the second parallel to the helical axis (~205 nm) [63, 64]. Figure 4.2 shows a fitted absorption spectrum of an α-helix and its three Gaussian components, plotted using parameters obtained by R. Mandel *et al.*, 1972 [63] in a sample of Poly-gamma-methyl-L-glutamate (PMG) in Hexafluoroisopropanol (HFIP).

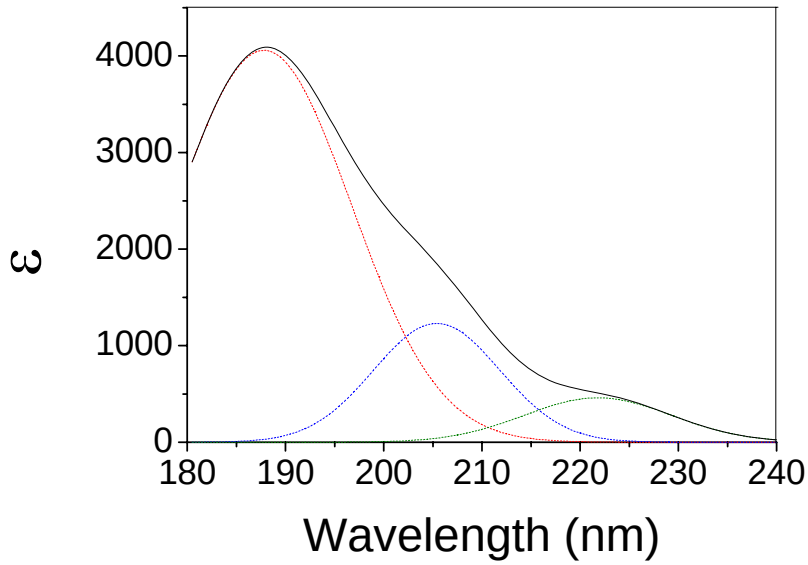

Figure 4.2 Fitted absorption spectrum (solid black) and its three Gaussian components (dotted), plotted using parameters obtained by R. Mandel *et al.*, 1972 [63] in a sample of PMG in HFIP.

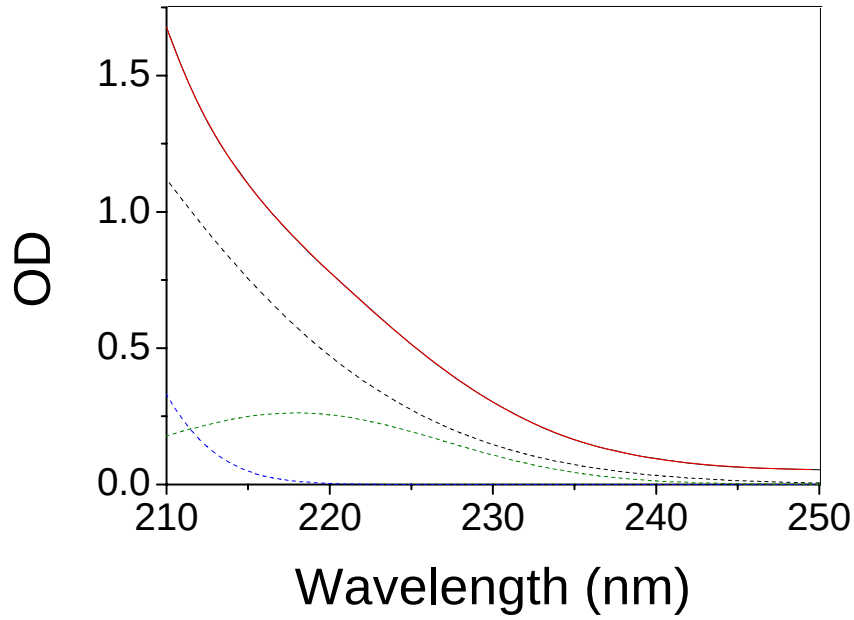

Figure 4.3 Absorption spectrum of PGA (20 mg/mL, pH 4.7, 100 μm pathlength) (solid black) at 21°C measured by a UV-visible spectrometer (Shimazu, UV-1700 Pharma Spec), its fitted spectrum (solid red) and its decomposition into three Gaussian bands: dashed black curve associated with the perpendicularly-polarized $\pi\rightarrow\pi^*$ transition, dashed blue curve associated with the parallel-polarized $\pi\rightarrow\pi^*$ transition and dashed olive curve associated with the $n\rightarrow\pi^*$ transition.

Transition		**Obtained here**	**Obtained by R. Mandel *et al.*, 1972 [63]**
$\pi\rightarrow\pi^*$ Perpendicularly-polarized	Amplitude	2.56	
	Center wavelength (nm)	186.8	187.8
	Bandwidth (nm)	25.6	12.6
$\pi\rightarrow\pi^*$ Parallel- polarized	Amplitude	2.41	
	Center wavelength (nm)	197.5	205.4
	Bandwidth (nm)	8.9	9.1
$n\rightarrow\pi^*$	Amplitude	0.26	
	Center wavelength (nm)	218	221.8
	Bandwidth (nm)	12.8	10.6

Table 4.1 Fitted parameters of the absorption spectrum of our PGA sample (20 mg/mL, pH 4.7, 100 μm pathlength) at 21°C using a tri-Gaussian function (4.1) and comparison with parameters obtained by R. Mandel *et al.*, 1972 [63] in a sample of PMG in HFIP.

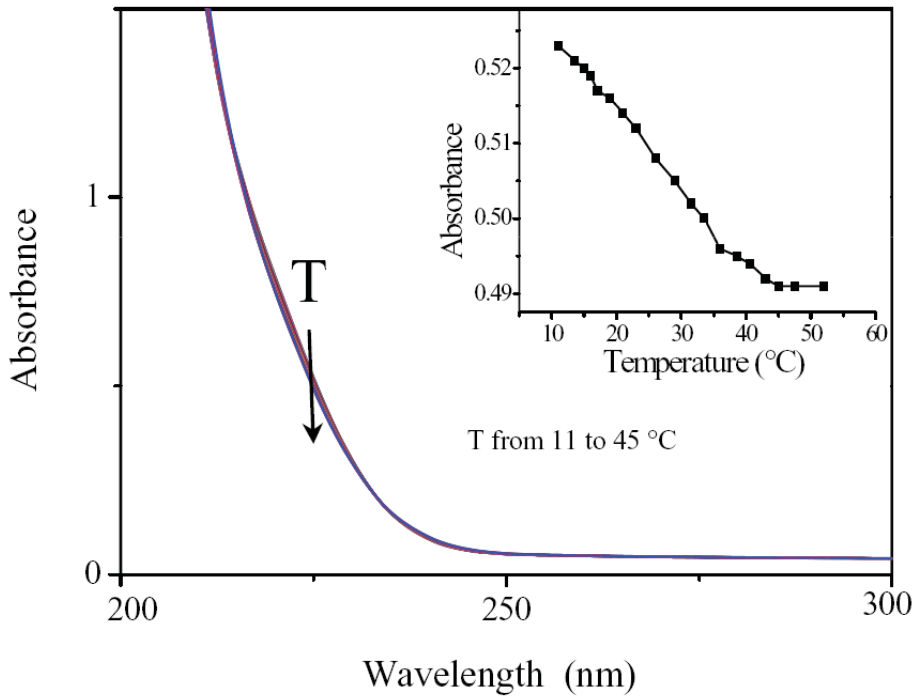

Figure 4.4 UV absorption spectrum of PGA (20 mg/mL, pH 4.7, 100 μm pathlength) for different temperatures ranging from 11 to 52 ◦C, measured by a UV-visible spectrometer (Shimazu, UV-1700 Pharma Spec). The inset displays the dependence of the absorbance at λ = 225 nm on temperature.

The absorption spectrum of our PGA sample at 21°C measured by a UV-visible spectrometer (Shimazu, UV-1700 Pharma Spec) is displayed in figure 4.3. The spectrum is fitted with a tri-Gaussian function

$$A = A_0 + \sum_{i=1}^{3} A_i \exp(-(\lambda - \lambda_i)^2 / \Delta_i^2), \qquad (4.1)$$

where

i =	1	corresponds to	the perpendicularly-polarized π→π* band,
	2		the parallel-polarized π→π* band,
	3		the n→π* band,

A_0 is an offset parameter, A_i is the amplitude of i band, λ_i is the center wavelength of i band and Δ_i is the bandwidth of i band. Its decomposition into three Gaussian bands $A_i \exp(-(\lambda - \lambda_i)^2 / \Delta_i^2)$ are also plotted in the same graph. Results of the fit and comparison with parameters obtained in previous work [63] are given in table 4.1. The n→π* transition band which was reported to occur at 222 nm [63] has a small broadening and a slight blue shift to 218 nm. This might be due to the formation of some β-sheets in the sample which has a n→π* transition at ~217 nm [65]. The parallel-polarized π→π* band is also shifted to shorter wavelength, observed at 197.5 nm. This fortifies the indication of the formation of β-sheet that has a π→π* transition occurs at ~194 nm for parallel sheets and ~196 nm for anti-

parallel sheets [65]. The two dipole-allowed π→π* transitions of β-sheet could also explain the broadening of the perpendicularly-polarized π→π* band (186.7 nm) since the fit only starts from 210 nm to 250 nm.

Figure 4.4 shows the absorption spectra of PGA for 17 temperatures ranging from 11 to 52°C, measured by the Shimazu UV-visible spectrometer. The interesting feature is enlarged in the inset and one clearly observes a decrease of absorption at 225 nm. This feature is consistent with the expected unfolding of PGA with increasing temperature as observed in reference [113].

4.3.2. Steady-state temperature-dependent CD measurements

Figure 4.5 shows the steady-state CD spectrum (solid black curve) of the PGA sample at 25°C. This spectrum was measured at the DISCO line of the SOLEIL synchrotron facility (France). It displays the well-known double minimum structure at 209 nm and 222 nm which is characteristics of a high-helicity sample.

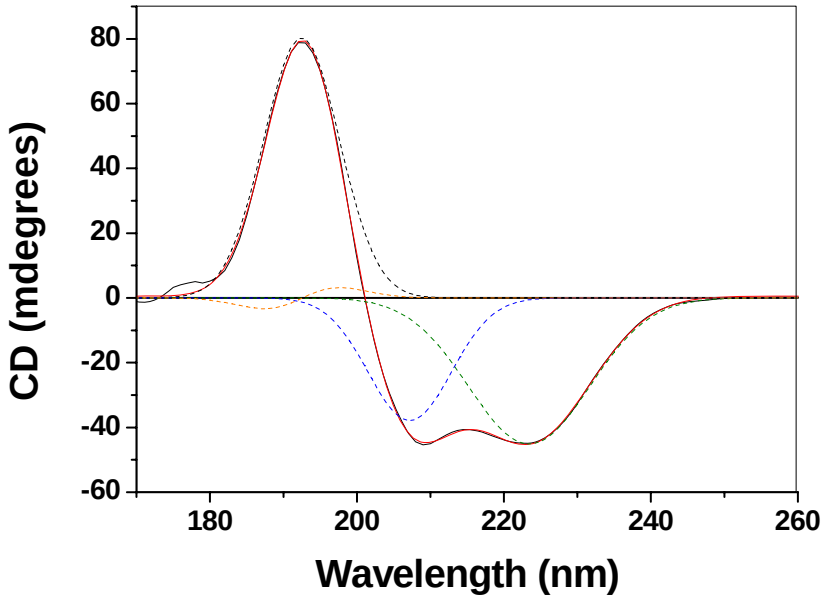

Figure 4.5 Steady-state CD spectrum (in mdeg, solid black curve) of PGA sample (20 mg/mL, pH 4.7), measured at the SOLEI synchrotron facility (France), its fitted spectrum (solid red curve) and its decomposition into three Gaussian bands (dashed black curve corresponding to the perpendicularly-polarized π→π* transition, dashed blue curve corresponding to the parallel-polarized π→π* transition and dashed olive curve corresponding to the n→π* transition) and the non-Gaussian helix band (dashed orange curve).

The CD spectrum of an α-helix is thought to be a combination of three CD bands associated with the 220 nm n→π* transition, the 190 nm perpendicularly-polarized π→π*

transition, the 205 nm parallel-polarized π→π* transition and an additional helix band [63]. In order to fit the CD spectrum of our PGA sample, following the method proposed by R. Mandel *et al.*, 1972 [63], we use a function which is defined as a sum of three Gaussians and a non-Gaussian helix term which is used to describe the additional helix band:

$$\theta = \theta_0 + \sum_{i=1}^{3} \theta_i \exp\left[-(\lambda - \lambda_i)^2 / \Delta_i^2\right] + \theta_H \left[2(\lambda_1 - \lambda)(\lambda_1 / \Delta_1^2) + 1\right] \exp\left[-(\lambda - \lambda_1)^2 / \Delta_1^2\right], \quad (4.2)$$

where

i = 1 corresponds to the perpendicularly-polarized π→π* band,
2 the parallel-polarized π→π* band,
3 the n→π* band,

θ_0 is an offset parameter, θ_i is the amplitude of *i* band, λ_i is the center wavelength of *i* band and Δ_i is the bandwidth of *i* band. The fitted curve and its decomposition into four single bands are also displayed in figure 4.5. The parameters of the fit and the results observed by R. Mandel *et al.*, 1972 [63] for a comparison are listed in table 4.2. As one can see, we gain similar results with the observation in the previous work, except for the broadening of the perpendicularly-polarized and the non-Guassian π→π* bands.

Transition		**Obtained here**	**Obtained by R. Mandel *et al.*, 1972 [63]**
π→π* Perpendicularly-polarized	Amplitude	80.5	
	Center wavelength (nm)	192.5	187.8
	Bandwidth (nm)	7.3	12.6
π→π* Parallel- polarized	Amplitude	-38	
	Center wavelength (nm)	207.2	205.4
	Bandwidth (nm)	8	9.1
n→π*	Amplitude	-45.2	
	Center wavelength (nm)	223.4	221.8
	Bandwidth (nm)	11.6	10.6
π→π* (non-Gaussian)	Amplitude	-0.1	
	Center wavelength (nm)	192.5	187.8
	Bandwidth (nm)	7.3	12.6

Table 4.2 Fitted parameters of the steady-state CD spectrum of our PGA sample (20 mg/mL, pH 4.7, 100 μm pathlength) at 21°C using a tri-Gaussian function (4.2) and comparison with parameters obtained by R. Mandel *et al.*, 1972 [63] in a sample of PMG in HFIP.

In order to measure the temperature dependence of the CD of our PGA sample, we have used our CD experiment set-up which allows measurement of the CD for λ = 225 nm. Figure 4.6 shows the steady-state temperature-dependent CD of our PGA sample. Here again, the decrease of CD (in absolute values) with temperature is a signature of the unfolding of the peptide. The helical fraction of the peptide can be estimated from its CD value following Rohl&Baldwin, 1997 [3]:

$$f_H = \frac{[\theta]_{222} - [\theta]_c}{[\theta]_H - [\theta]_c}, \tag{4.3}$$

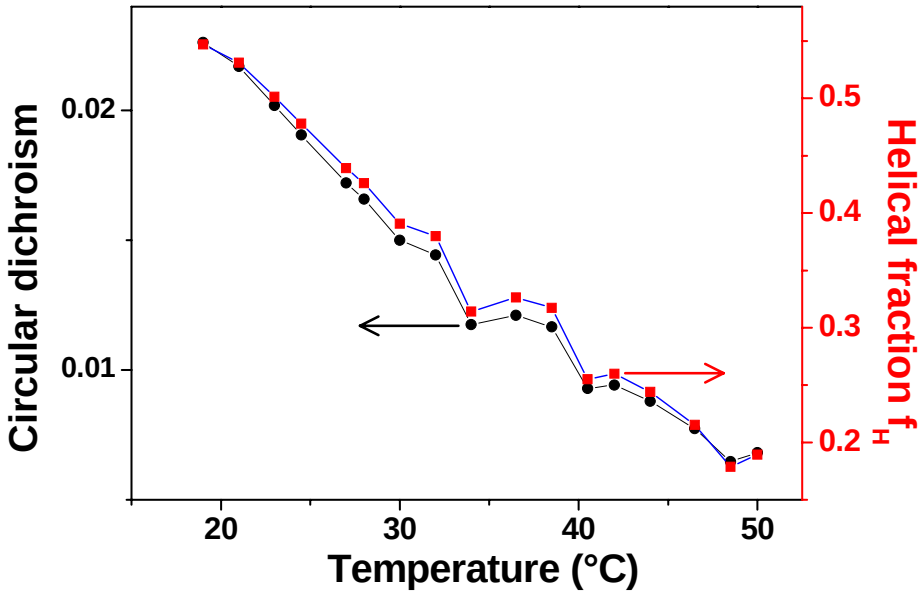

Figure 4.6 Circular dichroism (= $2\delta\alpha L$) in absolute values (dots, left scale) and the corresponding helical fraction [squares, right scale, calculated as described in equation (4.3)] of PGA (20 mg/ml, pH 4.7, 100µm pathlength) measured at 225 nm as a function of the temperature.

where $[\theta]_c = 2220 - 53T$ is the random coil ellipticity for temperature T expressed in °C and $[\theta]_H = -44000 + 250T$ is the ellipticity of an infinite α-helix. Ellipticities are expressed in deg.cm^2.dmol^{-1} per residue. In our measurement, we measure

$$CD = (\alpha_L - \alpha_R)L, \tag{4.4}$$

where α_L and α_R are the absorption coefficients for a left- and right-circularly polarized light, respectively. The conversion of our measured value, CD, to ellipticity is given by

$$[\theta] = \frac{3298}{\ln 10}\frac{CD}{cL}, \tag{4.5}$$

where c is the residue concentration (M) and L is the cell thickness (cm). With our experimental parameters, this yields $[\theta] = 925000CD$. Note that in order to reduce the laser

fluctuations, we chose to work at 225 nm instead of 222 nm. Given the shape of the CD curves (see figure 4.5), the slight discrepancy between these two wavelengths yields a negligible error. Thanks to equation (4.3), we can access the helical fraction in our PGA sample. It dependency as a function of the temperature is also displayed in figure 4.2 (right scale). It decreases from 0.55 at 19°C to 0.19 at 50°C. The peptide is about 50% helical at 23°C and around 80% randomly coiled at 50°C. Again, we observe a constant change in the temperature range of 20-35°C which was also observed in our temperature-dependent absorption measurements (previous paragraph). Furthermore, the agreement between temperature-dependent CD measurements (figure 4.6) and those of absorption measurements (figure 4.4) for λ = 225 nm has been confirmed by following equation:

$$A_{T1} - A_{T2} = -\log_{10} \frac{PMT_{T1}}{PMT_{T2}}, \tag{4.6}$$

where A_{T1} and A_{T2} are the absorbance of our PGA sample at temperatures *T1* and *T2* respectively measured by the Shimazu UV-Visible spectrometer and PMT_{T1} and PMT_{T2} are the PMT signal at each temperature obtained with our CD experiment set-up.

4.3.3. Quantitative observations of helix-coil unfolding dynamics

We have carried out T-jump experiments with T-jumps of 4-5°C from two starting temperatures: 21 and 28°C. According to results of the temperature-dependent absorption and CD measurements, we expect similar changes for both temperatures. Both measurements were carried out for λ = 225 nm.

Figure 4.7 displays the time-resolved absorption (black curve) and CD (red curve) changes measured in our PGA sample following heating of the water by a 8 mJ IR pulse for $T_{initial}$ = 28°C. The CD curve is the average of the three curves obtained by our three detection techniques simultaneously. The three CD curves are shown in the inset of figure 4.8. For absorption as well as for CD, we observe decreases in signal which are consistent with an unfolding of PGA after the T-jump. A drop of the absorbance of about 15 mOD and a drop of the CD of about 0.002 are obtained. All the curves can be very well fitted by a simple exponential function and results of the fit are listed in table 4.3. As one can see, considering the uncertainty of the dynamics, the three detection techniques give very similar results. Moreover, the same relaxation time constant of 0.6 µs is observed with time-resolved CD and time-resolved absorption. Comparing the measured changes in absorption or CD with the steady-state temperature-dependent data (figure 4.4 and 4.6), we find that the changes

correspond to a temperature increase by 4°C, in agreement with the size of the T-jump determined from the IR pump power we used, calibrated as described in chapter 3. The time-resolved CD result is directly converted to the absolute helical content using equation 4.3 and one obtains a decrease of about 5% in helicity of PGA (from 41% at 28 °C to 36 % at 32°C). This is the main advantage of CD measurements over measurements using other spectroscopic techniques for following protein/peptide folding dynamics. For any attempt to theoretically describe helix folding dynamics (or protein folding dynamics in general), e. g. using statistical mechanics models [4] or molecular dynamics simulations [111], quantitative knowledge of the helical content and its changes during equilibrate at the higher temperature will provide important additional experimental information compared to the usual kinetic experiments which only yields the relaxation time constant which only yields the relaxation time constant without giving and insight into the actual structural changes of the peptide.

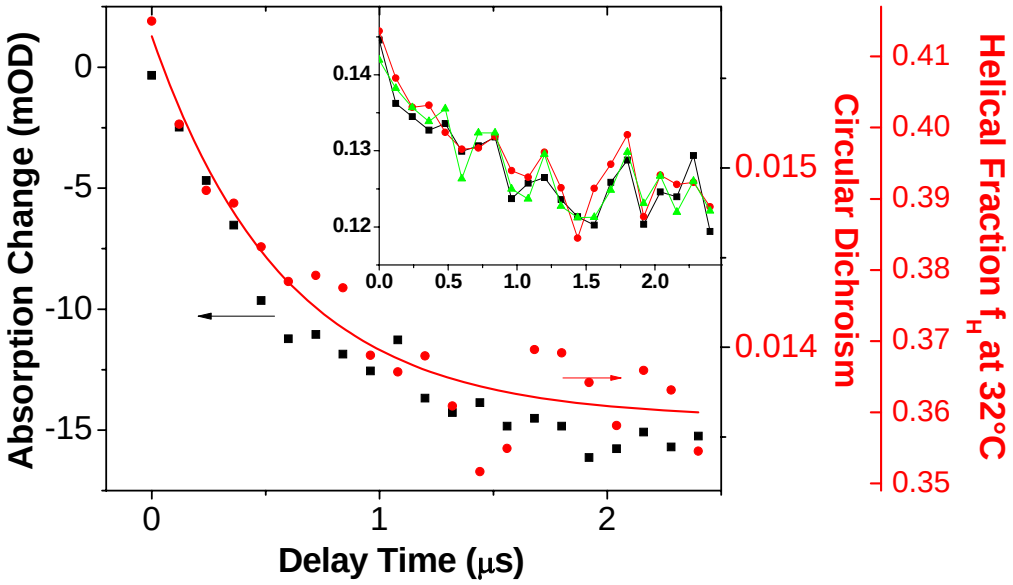

Figure 4.7 Transient UV absorption (squares, left scale) and CD (= $2\delta\alpha L$) in absolute values (dots, right scale) at 225 nm following a T-jump of 4°C in a sample of PGA (20 mg/mL, pH 4.7, 100 μm pathlength) at an initial temperature of 28°C. The solid line is an exponential fit common to the two data sets. The change in CD is translated to helical fraction, calculated as described in equation (4.3), on the far right scale. The inset shows the CD data obtained with the lock-in amplifier (squares), the direct measurement of $I_- - I_+$ (dots) or the Fast Fourier Transform technique (triangles).

		Relaxation time (μs)	Change in helical fraction (%)
Time-resolved CD	With Lock-in amplifier	0.6±0.2	
	Intensity difference calculated by PC	0.5±0.15	
	Performing FFT of the data	0.6±0.2	
	Average result	0.6±0.1	~ 5%
Time-resolved absorption		0.6±0.05	

Table 4.3 Relaxation time constant of the helix-coil transition and change in helicity of PGA (20 mg/mL, pH4.7, 100μm pathlength) for $T_{initial}$ = 28°C, induced by a T-jump of 4°C.

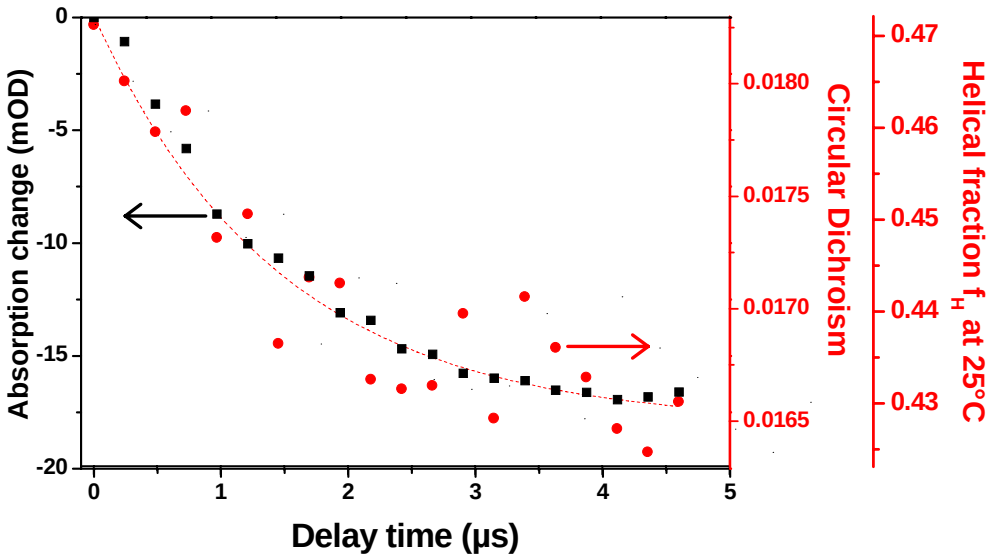

Figure 4.8 Transient UV absorption (squares, left scale) and CD (= $2\delta\alpha L$) in absolute values (dots, right scale) at 225 nm following a T-jump of 5°C in a sample of PGA (20 mg/mL, pH 4.7, 100 μm pathlength) at an initial temperature of 21°C. The dashed line is an exponential fit common to the two data sets. The change in CD is translated to helical fraction, calculated as described in equation (4.3), on the far right scale.

Figure 4.8 presents the time-resolved absorption (black) and CD (red) changes of the PGA sample induced by a T-jump of 5°C at starting temperature of 21°C. With the same fitting procedure using a mono-exponential function which has the results listed in table 4.4, we obtain a time constant of 1.5 μs for absorption as well as for CD. As expected, the relaxation time gets bigger at the lower temperature. We observe a drop of the absorbance of about 17 mOD and a drop of the CD of about 0.002, which are very similar to the results obtained for the T-jump of 5°C at the starting temperature of 28°C. This is consistent with

results of temperature-dependent absorption and CD measurements (figure 4.4 and 4.6) which give a constant slope for temperatures ranging between 20 and 35°C. This agreement between CD changes observed in the time-resolved and the steady-state measurements indicates that the peptide secondary structure fully equilibrates on the microsecond time scale. In term of helical fraction, the helicity of PGA decreases from 47% at 21°C to 43% at 26°C, losing 4% of helical fraction.

		Relaxation time (μs)	**Change in helical fraction (%)**
Time-resolved CD	With Lock-in amplifier	1.5±0.4	
	Intensity difference calculated by PC	1.6±0.5	
	Performing FFT of the data	1.3±0.4	
	Average result	1.5±0.3	~ 4%
Time-resolved absorption		1.5±0.1	

Table 4.4 Relaxation time constant of the helix-coil transition and change in helicity of PGA (20 mg/mL, pH4.7, 100μm pathlength) for $T_{initial}$ = 21°C, induced by a T-jump of 5°C.

4.3.4. Comparison with IR observations

In the course of our collaboration with Dr. Martin Volk's group, University of Liverpool (UK), the unfolding dynamics and time constants observed by our CD/T-jump measurements are discussed in comparison with those measured with IR detection by his PhD student (Sapna Sharma, 2006 [110]) in a 10 mg/mL PGA sample in D_2O. The IR/T-jump experiments uses detection at 1632 cm^{-1} using a setup which has been described in detail in Sharma's thesis [19]. Briefly, the solvent (D_2O) was heated using ns-laser pulses at 1970 nm, generated by a Nd:YAG/dye laser system with IR difference frequency generation. Absorbance changes at 1632 cm^{-1} were probed using the continuous IR beam from a tunable lead-salt diode laser and a fast HdCdTe photodiode with 50 MHz bandwidth, yielding an overall signal rise time of 14 ns. Due to the different strength of hydrogen and deuterium bonds, the pK value of the PGA side chain and the transition midpoint of pH/pD-induced helix unfolding curves are different in D_2O compared to H_2O, so that the sample needs to be adjusted to a higher pD for obtaining the same helical content. We found that a pD of ~5.6 was required for PGA in D_2O to have a helical content (as determined by CD) of approx. 0.5 at room temperature, and thus to have similar structural behavior as the sample in H_2O on

which dynamic CD experiments were performed. Figure 4.9 shows (in blue) absorbance changes measured on a 10 mg/mL PGA sample in D_2O, pD ~5.6, after a T-jump of 5°C from 28°C at 1632 cm^{-1}, i.e. near the maximum of the helical amide I' band. At this wavelength, there is a significant contribution from the solvent which appears instantaneously and remains constant on the ns to µs-time scale [2]. In addition, the amide I' absorbance decreases in parallel to helix unfolding, yielding dynamic information on this process. Within the uncertainty of the experiments, the dynamics are very similar to those observed by our UV-absorbance and by UV-CD. An exponential fit of the IR data yields a time constant of 0.79 ± 0.04 µs after a T-jump from 28°C to 33°C, which is close to the time constant of 0.6 ± 0.1 µs observed by CD after a T-jump from 28°C to 32°C, although the IR results, which are the average of 25,000 individual measurements and consequently have very high signal-to-noise, also show some deviation from a single exponential behavior which is not visible in the CD results due to noise. It has to be noted that the two samples most likely did not agree perfectly in their structural behavior/helical content, which is expected to be the major reason for any remaining differences in the dynamics observed by IR and CD.

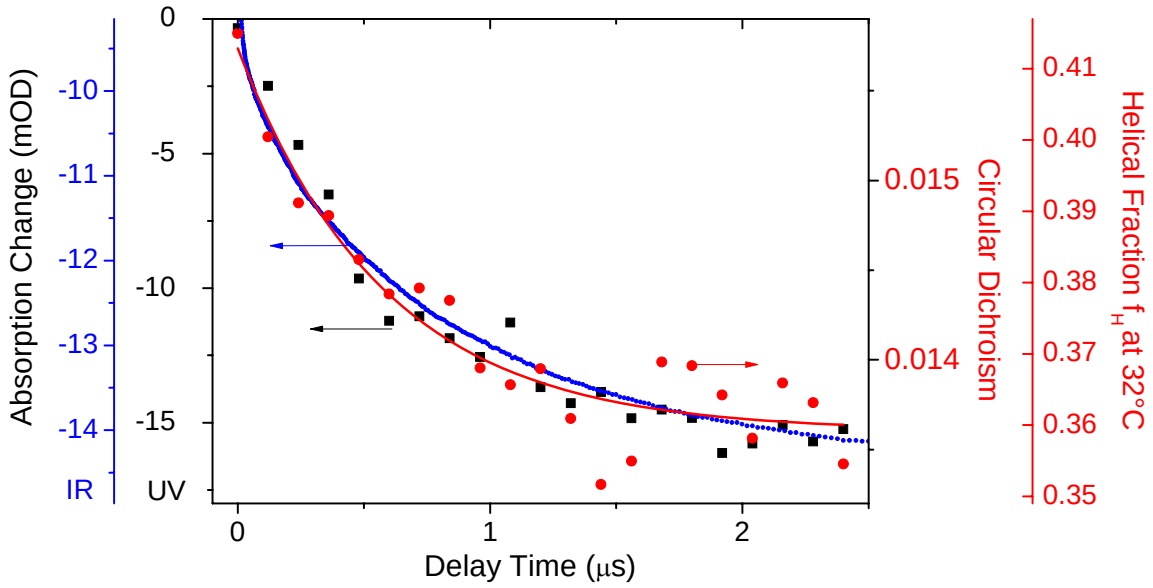

Figure 4.9 Change of IR absorption at 1632 cm^{-1} (solid blue, far left scale) in a 10 mg/mL PGA sample in D_2O, pD ~ 5.6, after a T-jump of 5°C from 28°C, measured by Sapna Sharma, University of Liverpool (UK), 2006 [19]. Also shown for a comparison are our results of transient UV absorption (squares, left scale) and CD (= $2\delta\alpha L$) in absolute values (dots, right scale) at 225 nm following a T-jump of 4°C in a sample of PGA (20 mg/mL, pH 4.7, 100 µm pathlength) at an initial temperature of 28°C. The solid line is an exponential fit common to the two data sets. The change in CD is translated to helical fraction, calculated as described in equation (4.3), on the far right scale.

In addition, the IR results obtained by Krejtschi and Hauser, 2011 [20] for a 20mg/mL PGA sample in D_2O at pD ~ 5.4 observed at 1632 cm^{-1} wavenumber after a T-jump from 23-33°C reported a relaxation time constant of 0.94 ± 0.01 μs, which is in the order of magnitude with Sharma's IR results and our CD results. The difference among the results might due to the fact that the unfolding kinetics does not exhibit a simple mono-exponential behaviour but rather a more complicated process which is proved by the IR observations, thus a higher T-jump which directs the system further from the equilibrium would result in a different average relaxation time constant.

4.4. Conclusion

Steady-state and time-resolved absorption and CD measurements on our PGA sample have carried out at initial temperatures of 21 and 28°C. The time-resolved measurements yield a decrease of the absorption by ~ 15-17 mOD and a drop of the CD by ~ 0.002, consistent with the steady-state measurements and a temperature jump determination of a 4-5°C jump. The relaxation time is measured to be 1.5 μs at 25°C and 0.6 μs at 32°C, similar with Sapna Sharma's results and in the order of magnitude with Krejtschi's measurements [111] using IR detection. Unlike IR detection, however, the CD experiment also allows quantitative monitoring of the thermal denaturation: we measure a drop of the helical fraction from 41% to 36% when the temperature jumps from 28 to 32°C and from 47% to 43% when it goes from 21 to 26°C.

CHAPTER 5

UNFOLDING DYNAMICS OF A COILED-COIL PEPTIDE DIMER STUDIED BY TEMPERATURE JUMP EXPERIMENT IN COMBINATION WITH IR SPECTROSCOPY

5.1. Introduction

Time-resolved IR spectroscopy has been proven to be a powerful technique which allows the direct observation of structural changes on nanosecond and microsecond time-scale [2, 4, 12, 25-33, 35, 41, 110]. We have a collaboration with Dr. Martin Volk at the Surface Science Center of University of Liverpool (GB), who has successfully developed a nanosecond T-jump experiment combined with time-resolved IR spectroscopy for the study of the fast folding/unfolding dynamics of α-helices [2, 12, 25, 30, 110], for a common purpose of better understanding of the dynamics of this particular secondary structure. Volk gives us a chance to acquire fast essential knowledge of T-jump experiment and the secondary conformational changes of α-helices as well as possibility of comparing our two techniques (IR spectroscopy in Volk's group and CD spectroscopy in our group).

In the course of our collaboration with Dr. Martin Volk, apart from exchanging our knowledge about time-resolved IR spectroscopy and time-resolved CD spectroscopy and comparing our results on the helix-coil unfolding dynamics of Poly(α-L-Glutamic Acid), we

also have studied such dynamics of a coiled-coil peptide dimer with his IR-probe T-jump experiment set-up.

5.1.1. IR spectroscopy in the study of secondary structures of proteins and peptides

IR spectroscopy of proteins and peptides in the region of the amide vibrations of the polypeptide structures is sensitive to the secondary conformations of the proteins and peptides. There are distinct differences between the IR spectra of α-helical, β-sheet, β-turn and random coil structures of the polypeptides [114]. These differences result from the dependence of interactions between various amide groups on the local polypeptide structures. Time-resolved IR spectroscopy can therefore provide direct observation of the secondary structural changes in proteins and peptides.

Peptides and proteins are known to absorb in 9 regions of the infrared spectrum, which are named as amide A, B, I, II, III, IV, V, VI and VII bands [115, 116]. The amide I band is commonly used in most IR studies because of its intense absorbance and distinct shift in frequency associated with changes in the secondary structure [116]. This vibration mode originates from a C=O stretching vibration (80%), a C-N stretch (10%) and an N-H bend (10%) and gives rise to IR band(s) between approximately 1600 cm^{-1} and 1700 cm^{-1}. The frequency of this band is highly dependent on hydrogen bonding and coupling between transition dipoles, both of which are directly related to the geometrical arrangements of the peptide groups in the polypeptide chain [23].

Time-resolved IR measurements of proteins and peptides [2, 4, 12, 25-33, 35, 41, 110] are always carried out in D_2O instead of H_2O because of the strong absorption of H_2O at 1650 cm^{-1}, which overlaps with the amide I band of the peptide. In comparison with H_2O, D_2O has weaker absorption in this region while still interacting with the peptide in a similar manner as H_2O. When the peptide is dissolved in D_2O, there occur hydrogen/deuterium (H/D) exchanges for solvent accessible amide protons. As deuterium is a heavier element, the N-H bend, which becomes N-D in D_2O, and the hydrogen bonded C=O stretch vibration are significantly influenced. Thus, the amide I' band (where the apostrophe denotes a deuterated form of the peptide) is shifted to lower frequencies between approximately 1650 cm^{-1} and 1630 cm^{-1}. Another factor that also contributes to this downshift is the solvation effect, which is different in D_2O in comparison with H_2O. The solvation effect involves the formation of

hydrogen/deuterium bonds between the solvent and peptide. The reported positions of the deuterated amide I' band for different secondary structural motifs are shown in table 5.1.

Frequencies (cm^{-1})	Assignment	References
1626-1645	α-helix	4, 31, 32, 109, 153, 154
1629, 1675	β-sheet	153, 154
1637	3_{10}-helix	31
1668, 1675, 1686	β-turn	32, 154
1642-1655, 1665-1675	Random coil	4, 31, 32, 154

Table 5.1 Positions of deuterated amide I' bands for the most common secondary structural motifs found in peptides and proteins.

The amide I' band of helical peptides is known to be temperature dependent. FTIR spectra versus temperature of proteins and peptides are usually performed in order to investigate the temperature dependency of the amide I' band [2, 4, 25, 30]. An increase in the temperature shifts the helix-coil equilibrium towards less helical structures. Hence, the fraction of helical structures (with an amide I' frequency of approximately 1630 cm^{-1}) decreases, whereas the fraction of random coil conformations (with amide I' frequencies of approximately 1655 cm^{-1} and 1670 cm^{-1}) increases. As a result, the amide I' band widens and shifts to higher frequencies. Although the spectral shift is mostly caused by this redistribution of secondary structures, there is also a small contribution of the temperature dependency of the interaction of the backbone carbonyl group with solvent [25].

5.1.2. Folding/unfolding dynamics of coiled-coil peptides

Coiled-coil peptides comprise leucine zipper domains that consist of heptad repeats of seven residues that characterize their sequences (figure 5.1). The peptides contain two amphipathic α-helices, twisted around each other and held by hydrophobic interactions, which are additionally stabilized by electrostatic interactions of polar side chains.

The coiled-coil peptide models that have been extensively studied are GCN4 and their truncated forms. The folding kinetics of GCN4 was first studied by time-resolved stop-flow fluorescence [117-120] and CD techniques [121-123], which reported a two-state-model like folding behaviour. However, these stop-flow techniques have limited time resolution of several milliseconds, thus can only allow observation of slow processes. However, Bai in

2003 proposed that even proteins that exhibit two-state folding kinetics in stop-flowed experiments might actually fold via "hidden" intermediates which could not be seen in first-ordered stopped-flow folding kinetics [124]. T-jump/IR studies on two variants of the GCN4, which have a cross-linker at either the N-terminus or C-terminus, have shown a non-monoexponential relaxation kinetics behaviour, supporting a folding mechanism wherein at least one folding intermediate exists behind the main rate-limiting step of the conventional stopped-flow techniques (Wang *et al.*, 2005 [125]). The relaxation times for helix melting are between 10 and 100 μs. Studying a truncated version of GCN4 by T-jump/UV resonance Raman spectroscopy, Balakrishnan *et al.*, 2006 [126] have obtained much shorter time constants, 0.2 and 15 μs, compared with those reported above by Wang *et al.* [125]. The 200 ns time constant was directly interpreted as the time scale of single helix relaxation, suggesting that some coiled-coils unravelled under their conditions and the helices then rapidly undergo helix-coil transition, followed by further coiled-coil unravelling on the 10 μs time scale. Studying the truncation perturbation on the folding kinetics of cross-linked GCN4 in a T-jump/IR experiment, Bunagan *et al.*, 2006 [127] have observed an ultrafast folding with a 2μs relaxation time constant when removing the first heptad repeat in the peptide sequence, which is 50 times faster than the overall relaxation time (~ 100 μs) of the full-length protein given by Wang *et al.* [125].

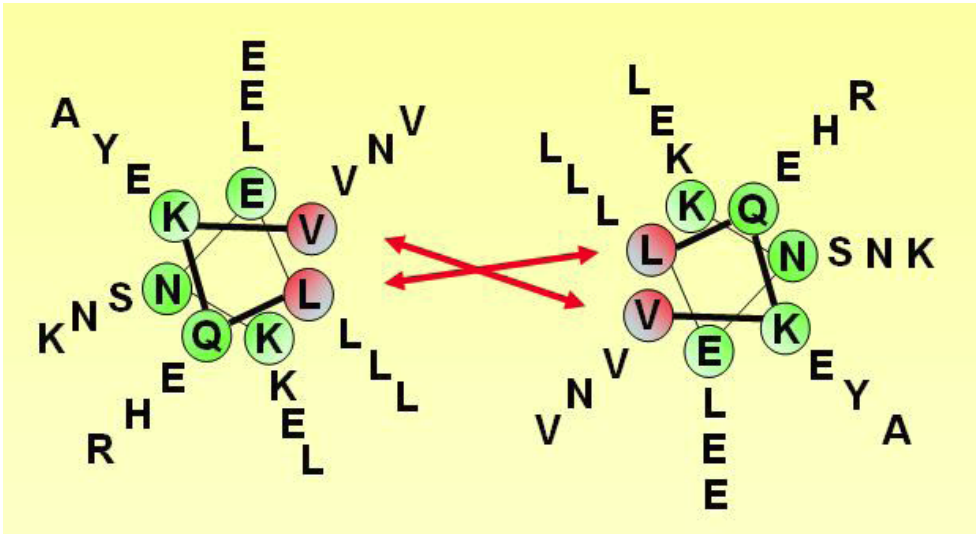

Figure 5.1 A heptad wheel of a coiled-coil peptide structure. The hydrophobic core is indicated in red.

On the other hand, Zitzewit *et al.*, 2000 [121] has shown that the 10-residue sequence at the C-terminus of GCN4 plays a critical role in triggering helix initiation and tertiary structure formation. Also, investigating the effect of truncation on the stability of GCN4 at both N- and C-terminus, Lumb *et al.*, 1994 [128] have concluded that the coiled-coil peptide contain stable subdomains and the formation of specific tertiary interactions is needed for cooperative folding. Wang *et al.*, 2005 [125] suggested that the major folding transition barrier in the coiled-coil peptide arises from the cooperative association of the two peptide strands. Bunagan *et al.*, 2006 [127] indicated that the truncation of the coiled-coil peptide greatly diminishes the folding free energy barrier and results in a maximum folding rate. However, the formation of such subdomain does not appear to dictate the overall folding kinetics.

5.2. Sample and preparation

5.2.1. Material

A leucine zipper-like peptide with the sequence

Ac-RMVKQLENKVEELLSKNYHLENEVARLEKLVGERGGGC-NH_2,

where Ac is an acetyl group and

VKQLENKVEELLSKNYHLENEVARLEKLVGER

contributes to the secondary and tertiary structure of the peptide were kindly supplied by Dr. Molly M. Stevens (Imperial College, London, UK), who has a collaboration with Dr. Volk's group, as lyophilized powder.

5.2.2. CD measurements

For the CD measurements, the coiled-coil peptides were dissolved with a 0.6 mg/ml concentration in a phosphate aqueous buffer (50 mM, pH7, 150 mM NaCl). The measurements were performed by Dr. Stevens's group.

5.2.3. Temperature jump measurements

For temperature jump measurements, the coiled-coil peptides were dissolved with two concentrations: ~ 7 mg/ml and ~ 15 mg/ml in a phosphate buffer/basic fuchsin solution. The

phosphate buffer has pH*~6.7. The buffer/basic fuchsin solution was prepared in D_2O with a phosphate concentration of 50 mM and a dye concentration of 0.6 mM. The addition of basic fuchsin to the sample solutions is needed for indirect heating of the samples since the dye serves as heat-transducing agent. The pH* of each sample were measured using a Whatman PHA230 pH meter fitted with a Hanna Instruments microelectrode (HI1083). In order to convert to pD value of the samples, a constant of 0.4 was added:

$$pD = pH^* + 0.4 \tag{5.1}$$

Thus, the pD value of the phosphate buffer is 7.1.

5.2.4. FTIR measurements

FTIR spectra were taken using a Biorad FTS-40 spectrometer with $1cm^{-1}$ resolution before and after temperature jump measurements on the samples at room temperature to verify that no noticeable irreversible structural changes occurred in the peptide during the temperature jump measurements.

For temperature-dependent FTIR measurements, the coiled-coil peptides were dissolved in the phosphate buffer/D_2O solution with two concentrations: ~ 7 mg/ml and ~ 15 mg/ml with and without the presence of basic fuchsin (table 5.1).

	Peptide concentration	**Phosphate concentration**	**Basic fuchsin concentration**	**pD of phosphate buffer**
Sample 1	7 mg/ml	50 mM	-	7.1
Sample 2	7 mg/ml	50 mM	0.6 mM	7.1
Sample 3	15 mg/ml	50 mM	0.6 mM	7.1

Table 5.2 Conditions of different samples for temperature-dependent FTIR measurements.

5.3. Technical details

5.3.1. Experimental set-up

The IR-probe T-jump experiments have been developed by Martin Volk's group and have been used to investigate the helix-coil dynamic of some α-helical peptides [2, 12, 25,

30, 110]. A schematic representation of the set-up used for studying the coil-coiled dimer is depicted in figure 5.2.

Here, the nanosecond laser pulses working as the pump are created by a Nd:YAG laser (Quantel "Brilliant"), which delivers second harmonic pulses at 532 nm with 5ns pulse duration and 10Hz repetition rate. These visible pulses are used to excite a heat transducer which undergoes rapid internal conversion, instantaneously heating up the solvent. Before passing through a sample, the pump beam is split into two beams which are then directed and focused onto the sample in opposite directions. The angle of the beamsplitter is adjusted to achieve two beams with approximately similar intensities. This increases the heating homogeneity along the beam path. Typical pump pulse energy used in the experiment is about 1.1 mJ.

The probe comes from a continuous IR laser diode (Műtek TLS 150), which is tunable to several stable modes between 1570 cm^{-1} and 1641 cm^{-1}. This spectral range contains the amide I' band. The probe beam is collected and collimated by a parabolic Au mirror, reflected and then focused onto the sample with a 150 mm focal length CaF_2 lens, giving a probe beam diameter of less than 50 μm. One part of the beam will be absorbed by the sample and the transmitted part is collimated by a lens (CaF_2, 150 mm focal length), reflected by a gold mirror and focused onto a fast IR detector using a CaF_2 lens with 150 mm focal length. The detector contains a $N_{2(L)}$-cooled Mercury Cadmium-Telluride Kolmar KMPV50-0.5-J2 50MHz photodiode. The resolution of these experiments is determined by the 15ns rising time of the detector.

The detector is connected to a 300MHz digital oscilloscope (Tektronix TDS 3032), which is triggered by scattered 532 nm light, collected by a fast silicon photodiode (Thorlabs DET210, rise time 1ns). When measurements were being taken, 128 single scans were averaged by the oscilloscope before transferring through an IEEE connection to a PC, where they were analysed.

The YAG laser produces radio frequency (RF) electric noise that is picked up by the IR detector. The detected amount of RF noise are significantly diminished with the help of double wire-mesh sleeves for all cabling, some copper tape for covering detector input and output and several filters and capacitors added to the detector power supply.

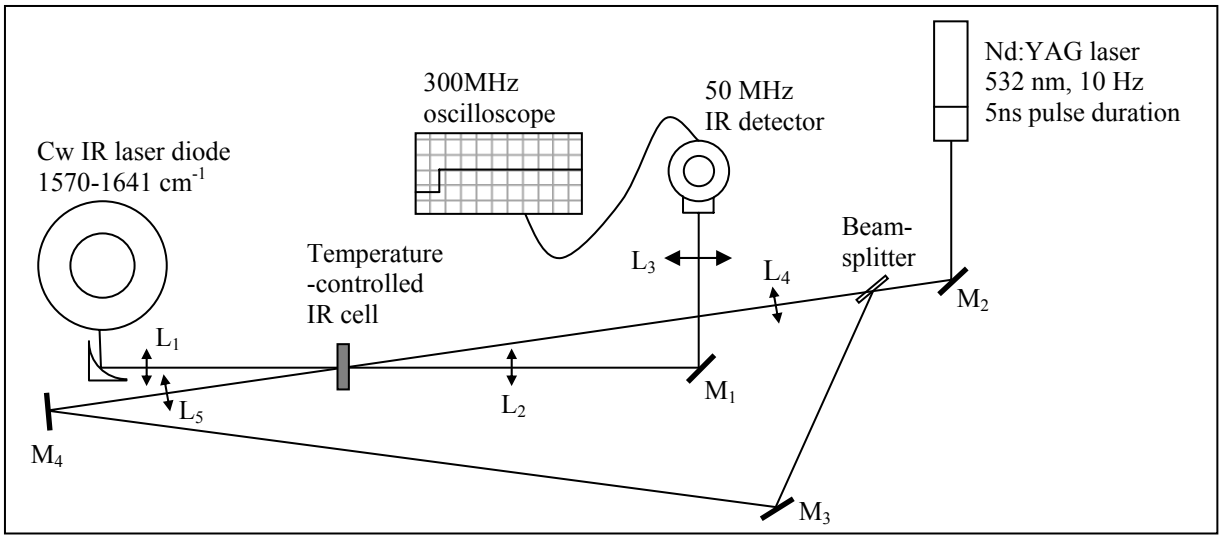

Figure 5.2 Schematic representation of Dr. Volk's T-jump experiment set-up.

5.3.2. Pump beam profiles

In order to ensure the temperature jump to be homogeneously induced in the sample, conditions were chosen for the diameter of the forward/backward pump beam foci to be approximately 10 times bigger than the diameter of the probe beam focus, which is about 50 μm.

The pump profiles were measured by using a 100 μm pinhole, which was placed at the sample position on a micrometer translation stage that allows fine movement of the pinhole in horizontal and vertical directions. The sample position was determined by finding the place where the transmitted part of the probe beam through the pinhole was largest. The amount of transmitted pump light was measured using a fast silicon photodiode (Thorlabs DET210, 1 ns rise time), which was placed behind the pinhole and connected to the oscilloscope. The forward/backward pump beam profile was acquired by plotting the amount of transmitted forward/backward pump beam through the pinhole when moving the pinhole in 50μm steps. The forward/backward beam profiles are shown in figure 5.3.

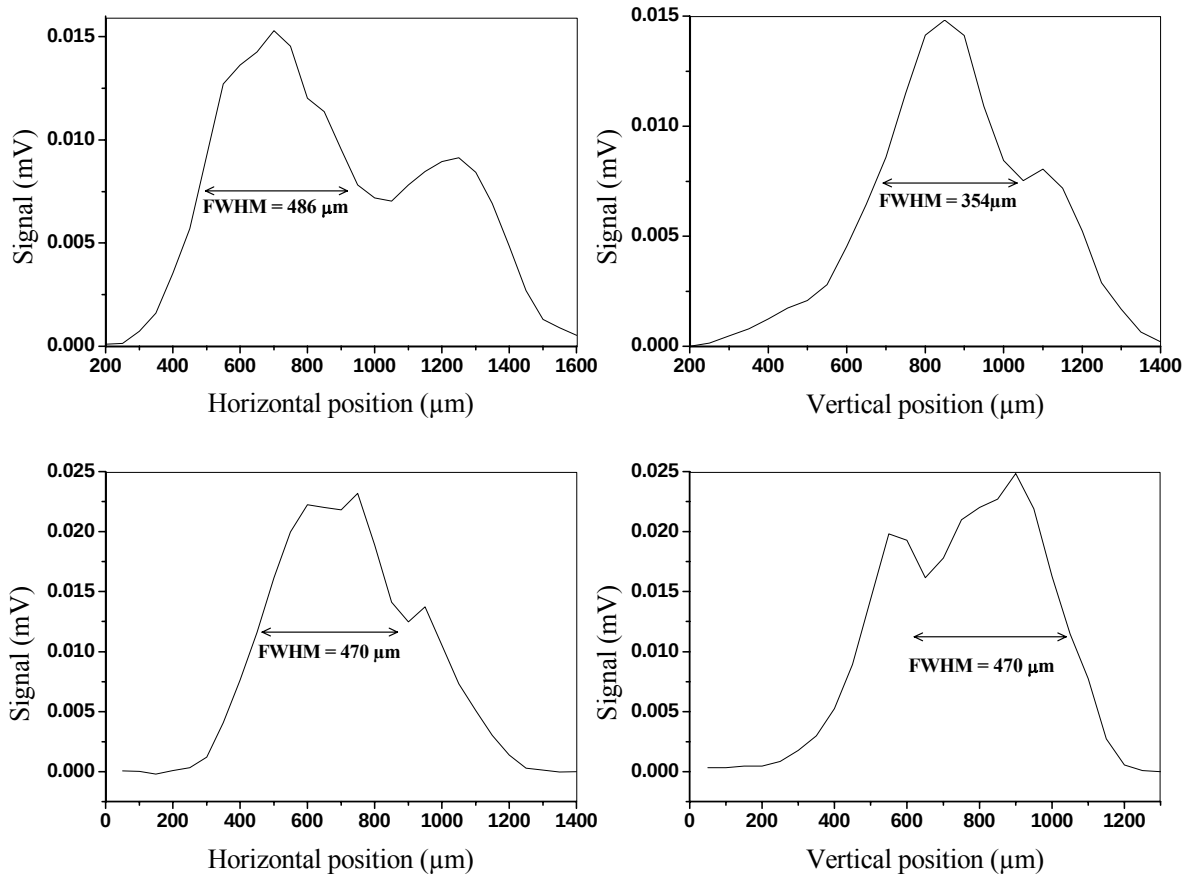

Figure 5.3 Profiles of forward pump beam (upper graphs) and backward pump beam (lower graphs).

5.3.3. Optimisation of pump and probe beam overlap

As mentioned previously in chapter 2, optimisation of pump and probe beam overlap is important to obtain a homogenous temperature jump signal. This procedure was carried out in two steps:

First, the pump and probe beam overlap was roughly obtained by optimising the amount of transmitted part of the forward/backward pump beam through the pinhole, which was fixed at probe focus position, "by eyes", i.e., using a piece of white paper behind the pinhole. This step was done by adjustment of the lens L_4 for the forward pump beam and the mirror M_4 for the backward pump beam.

Second, the pinhole was replaced with the sample, which contained basic fuchsin dye solution, and the pump/probe overlap was obtained by firstly, optimizing the size of the temperature jump for forward/backward pump beam, and secondly, balancing the size of the

temperature jump induced by each pump beam. The temperature jump signal was obtained in the oscilloscope and quantified in the PC. The adjustment was made by moving slightly the lens L_4 for the forward beam and the mirror M_4 for the backward beam. The resulting total size of the temperature rise must be approximately twice larger than the size of the temperature jump caused by forward/backward pump beam.

5.3.4. Data analysis

A T-jump (TJ) measurement, which consists of 128 single scans at a repetition rate of 10 Hz (averaged in the oscilloscope before being transferred to the PC) with the pump beam unblocked, allowed recording of the intensity changes of the probe light after sudden increases in temperature in the sample induced by the pump pulses. A background (BG) measurement was also carried out in the same manner, but with the pump beam blocked. As the RF noise is reproducible to a certain extent, the background measurement is needed in the analysis in order to considerably reduce further the RF electric noise by subtracting from the temperature jump measurement. To maximize RF electric noise reproducibility, the background measurements were taken after every temperature jump measurement.

Once the signal has been transferred to the PC, the data is converted into absorbance change ΔA by a written program using following equation:

$$\Delta A(t) = -\log\left(\frac{I(t)}{I_0}\right), \tag{5.2}$$

where t is the time delay after the temperature jump, $I(t)$ is the time-dependent intensity after the temperature jump (after correction for RF electric noise by subtraction of BG) and I_0 the intensity at negative times (just before the temperature jump). It is important to note that, when the probe beam is blocked, the oscilloscope displays a negative signal of around 100 mV, which must be measured before taking any measurements and added to the observed signals to obtain the real signal which is proportional to the probe light intensity. All data were analyzed immediately by the program after every couple of TJ-BG measurements and data of any bad measurements were rejected. After measurements consisting of 128 single scans had been analyzed in this way, all the measurements (30-90 measurements) were averaged to obtain a single average curve. This average curve was then smoothed by using a logarithmical averaging program. After 50 ns, the program averages any data obtained at

times within 1%, i.e., for 1000 ns, any data acquired between 995 and 1005 ns would be averaged.

After a fast temperature jump, the heat begins to diffuse and the sample cools down to the initial temperature on a time scale of several milliseconds. However, in Volk's previous work [2, 30, 110], the onset of cooling was already observable on the hundred nanosecond to microsecond time scale, which is also the time scale of the folding dynamics of α-helical peptides. This therefore requires a correction with the cooling kinetics to obtain reliable results on the secondary structural dynamics of the α-helical peptides. Thus, measurements were performed to probe the sample at two frequencies: 1592 cm^{-1} where D_2O absorbed and the coiled-coil peptide's absorption could be (almost, see below) neglected and 1632 cm^{-1} where absorption of the peptide could be observed (see FTIR spectra of the coiled-coil peptide in another paragraph).

Figure 5.4 show our data (after logarithmically averaging) obtained at 1592 cm^{-1} and 1632 cm^{-1} after a ~1°C T-jump from 70°C starting temperature in a coiled-coil peptide sample with a 15 mg/ml concentration, studied in a 100μm pathlength CaF_2 cell. As D_2O is heated, its absorption decreases leading to instantaneous bleach observed at both wavenumber, which can even be used to calibrate the T-jump. Now one can see that at 1632 cm^{-1}, in addition to the major bleach due to D_2O, there is small bleach from the peptide which occurs on a microsecond timescale. The recovery of the two curves indicates cooling, which takes place on a millisecond time scale.

The size of the T-jump was determined from the measurement taken at 1592 cm^{-1}, where only D_2O absorbs significantly. The temperature calibration was done and described in Ramajo's thesis [129] by measuring the temperature-dependent FTIR spectra of D_2O. The absorbance change of D_2O per degree centigrade for 50 μm pathlength was found at 1570 cm^{-1} to be (-0.0015±0.0001)/°C, with no strong wavelength dependence.

Usually, the cooling correction can be accomplished by dividing the data obtained at 1632 cm^{-1} by the cooling function. The cooling function is evaluated upon fitting the data obtained at 1592 cm^{-1} with an exponential/bi-exponential/tri-exponential function. We have well fitted the curve at 1592 cm^{-1} (see figure 5.4, blue curve) using a tri-exponential function, however, we observed a distortion effect on the obtained cooling functions which occurs on the time scale of tens of microseconds to hundreds of microseconds (figure 5.5). This matches

the time scale of the dynamics of the coiled-coil peptide (see the curve for 1632 cm^{-1} in figure 5.4), which indicates that the absorption of the peptide at 1592 cm^{-1} could not be ignored. Ideally, in such cases, the cooling function should be determined from measurements on a sample without the presence of the peptide. These measurements will be undertaken in the near future. On the other hand, we could still obtain an idea about the dynamics of the coiled-coil peptide by globally fitting the two curves at 1592 cm^{-1} and 1632 cm^{-1} at the same time using Origin with the following fit function:

$$y = \left(y_0 + Ae^{-(kt)^C}\right)\left[A_1 e^{-\frac{t}{t_1}} + A_2 e^{-\frac{t}{t_2}} + \left(1 - A_1 - A_2\right)e^{-\frac{t}{t_3}}\right], \tag{5.3}$$

where y_0 is an offset constant, A is the amplitude of the absorbance change due to peptide unfolding, A_1 and A_2 are the amplitudes of cooling, k is the rate constant of peptide folding, t is the time, t_1, t_2 and t_3 are the time constants of cooling and C is a measure of the net deviation from monoexponentiality. The first factor, which is a stretched exponential, represents the fit function describing the dynamics of the peptide at a given temperature, whereas the second factor, which is a tri-exponential, represents the cooling function at this temperature. The global fitting was performed for the two curves with some shared parameters, namely k, C, A_1, t_1, A_2, t_2 and t_3 while A_1, t_1, A_2 and t_2 were fixed and were predetermined by Volk's cooling simulation (with the same principle which was described previously in section 3.3) for the same sample cell thickness. The shared parameters are the same for both frequencies, since the cooling kinetics only depends on the cell pathlength, heat conductivity and heat capacity of the solvent and the sample cell material (see the simulation of the temperature jump in chapter 3) and the time constant of the dynamics of the peptide is independent on different observing frequencies.

From the values of k and C obtained from the global fit, the average relaxation time constant of the dynamics of the coiled-coil peptide was calculated using the equation below:

$$\tau_{average}\left(k, C\right) = \frac{\Gamma\left(\frac{1}{C}\right)}{kC}. \tag{5.4}$$

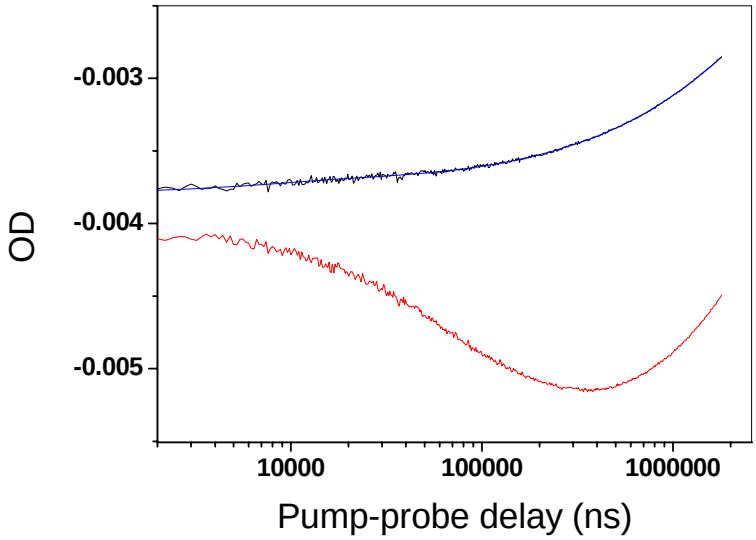

Figure 5.4 Data (after logarithmically averaged) obtained at 1592 cm^{-1} (black) and 1632 cm^{-1} (red) after a ~ 1°C T-jump from 70°C starting temperature in a coiled-coil peptide sample with a 15 μg/ml concentration, studied in a CaF_2 cell having a 100μm pathlength. Blue curve is the fit for the data at 1592 cm^{-1} using a tri-exponential function.

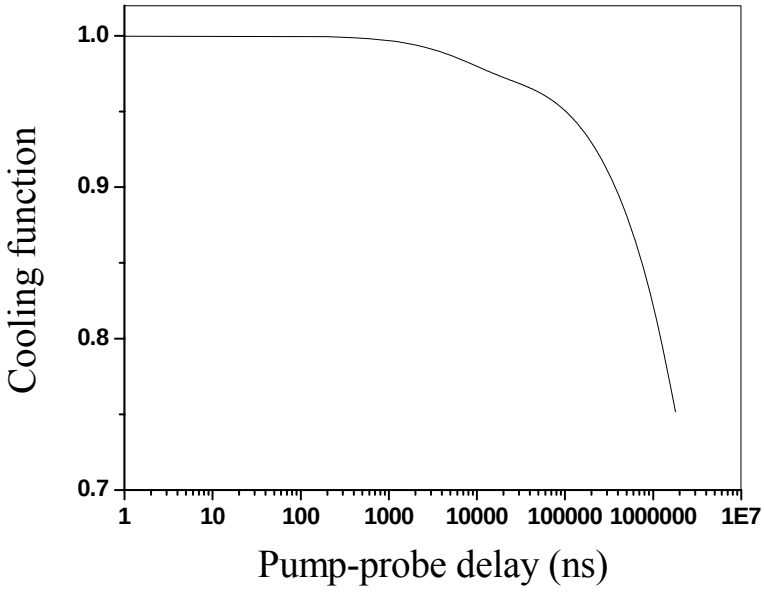

Figure 5.5 Cooling function after a ~ 1°C T-jump from 70°C starting temperature determined by fitting the data (after logarithmically averaging) obtained at 1592 cm^{-1} in a coiled-coil peptide sample with a 15 μg/ml concentration, studied in a CaF_2 cell having a 100μm pathlength.

In order to have a vision of the reliability and accuracy of the results we obtained, an approximate determination for the error $Er(\tau_{average})$ of the relaxation time constant was done, relying on the errors of k and C values given by Origin:

$$Er\left(\tau_{average}\right)=\frac{\tau_{average}\left(k+Er(k),C+Er(C)\right)+\tau_{average}\left(k-Er(k),C-Er(C)\right)}{2}, \qquad (5.5)$$

where *Er(k)* and *Er(C)* are the errors of *k* and *C* values respectively, provided by Origin.

5.3.5. Sample cells

For all temperature jump and FTIR measurements, the samples were held between two CaF2 windows separated by a Teflon spacer of 50 μm or 100 μm and mounted in a copper temperature-controlled cell where the temperature of the sample can be controlled.

5.4. Results and discussions

5.4.1. CD measurements

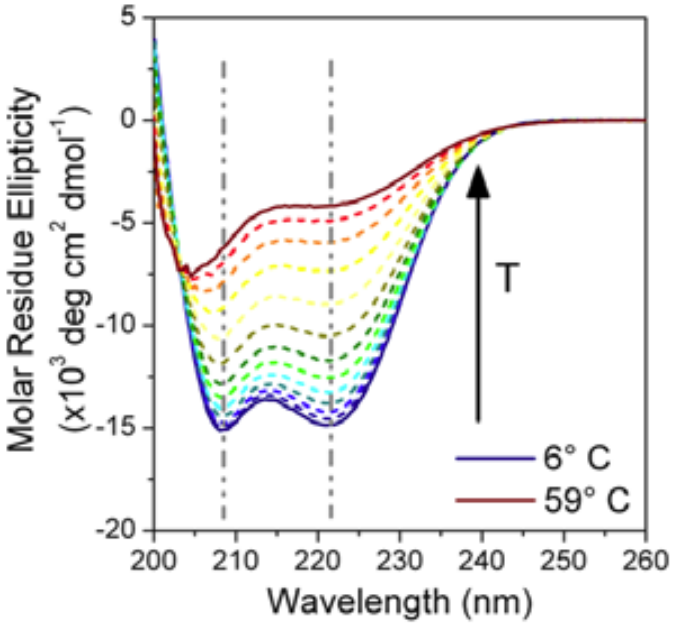

Figure 5.6 Temperature-dependent steady-state CD spectra of a coiled-coil peptide sample with a 0.6 mg/ml concentration in phosphate aqueous buffer (50 mM, pH7, 150 mM NaCl).

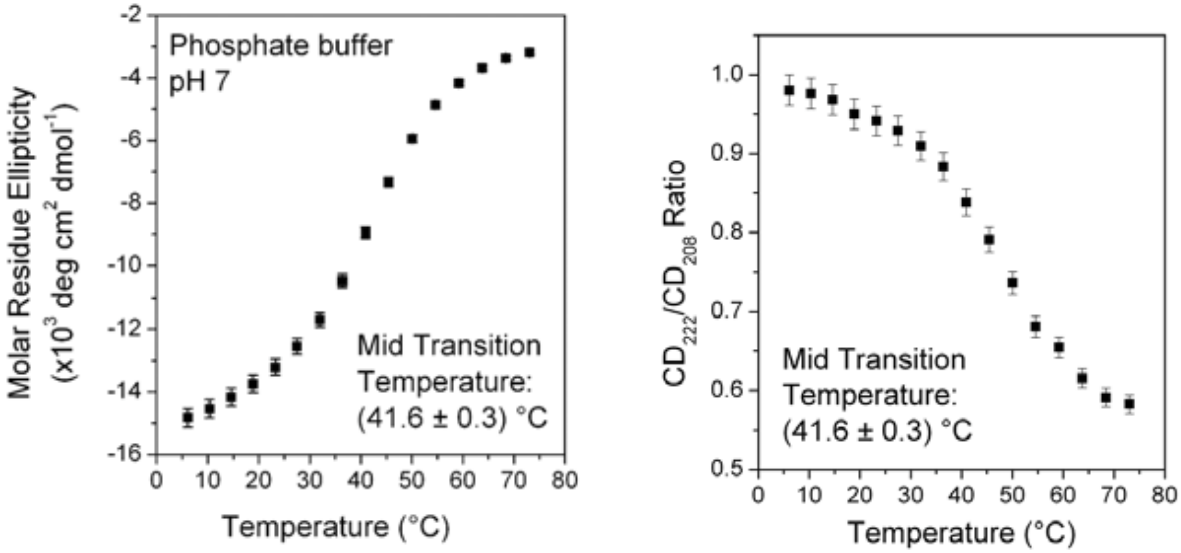

a) b)

Figure 5.7 a) Molar residue ellipticity at 222 nm versus temperature b) Ratio of CD at 222 nm and 208 nm versus temperature.

Temperature-dependent steady-state CD measurements have proved the thermal response of the coiled-coil peptide (figure 5.6). Figure 5.7a plotting the molar ellipticity at 222 nm versus temperature, shows that the sample exhibits higher helical fraction at low temperature. The decrease of the ratio of CD at 222 nm and 208 nm with temperature (figure 5.7b) suggests that the peptide forms coiled-coils at low temperature and disassembles at higher temperature with a mid-transition point of ~ 42°C.

5.4.2. Temperature-dependent FTIR measurements

Temperature-dependent FTIR measurements have been carried out on coiled-coil peptide samples at two peptide concentrations: ~ 7 mg/ml and ~ 15 mg/ml in phosphate buffer/D_2O solution with and without the presence of basic fuchsin. Note that the measurements without the presence of the dye have been only done for the peptide concentration of 7mg/ml. Such measurements will be performed for the peptide concentration of 15 mg/ml in future. Since there were usually some water vapour remaining in the FTIR spectrometer chamber despite of the regular circulation of dry air through the spectrometer during the measurements, the obtained FTIR spectra must be corrected by subtraction of a certain percentage of a FTIR spectrum of the water vapour. Moreover, as D_2O absorbs in the

amide I' band which is the region of interest in the IR/temperature jump measurements, a FTIR spectrum of D_2O also need to be subtracted from the FTIR spectra of the samples.

Figure 5.8 shows the temperature-dependent FTIR spectra of the three samples. The strong band at 1672 cm^{-1} that is seen in these spectra can be confidently assigned to absorption of TFA (trifluoroacetic acid) which is used in the peptide synthesis procedures. The presence of TFA, however, doesn't affect the outcomes of the temperature jump measurements which were taken at 1592 cm^{-1} and 1632 cm^{-1}, far enough from TFA's absorption band at 1672 cm^{-1}.

One can also observe the thermo-response of the coiled-coil peptide in these FTIR spectra. Upon increasing the temperature, the maximum absorbance of the amide I' decreases, the band is broadened and in general shifted to higher frequencies. This indicates a redistribution of secondary structures of the coiled-coil peptide sample toward less helical configuration, which is in agreement with the indication from temperature-dependent CD measurements.

At temperatures lower than 50°C, the FTIR spectra of the sample in the absence of basic fuchsin are different from the ones with the presence of the dye. At low temperatures ($\leq$ 40°C), the peak wavelengths of the FTIR spectra are located at higher frequencies in the absence of the dye, indicating less helicity of the sample. The peak wavelength stays unchanged when the temperature increases up to 40°C with or without the presence of the dye. However, the maximum absorbance decreases in the absence of the dye and stays more or less constant with the dye presence. This indicates that there is a decrease in the peptide concentration of the sample in the absence of the dye due to aggregation. We have clearly observed aggregation of the samples by eyes at temperatures lower than 50°C. The peak wavelength of the sample without the presence of the dye shifts to lower frequencies when the temperature increases from 40°C to 50°C. At higher temperatures ($\geq$ 50°C), the FTIR spectra look identical with or without the presence of the dye. We assume that the presence of the dye in the samples has affected the aggregation state of the peptide.

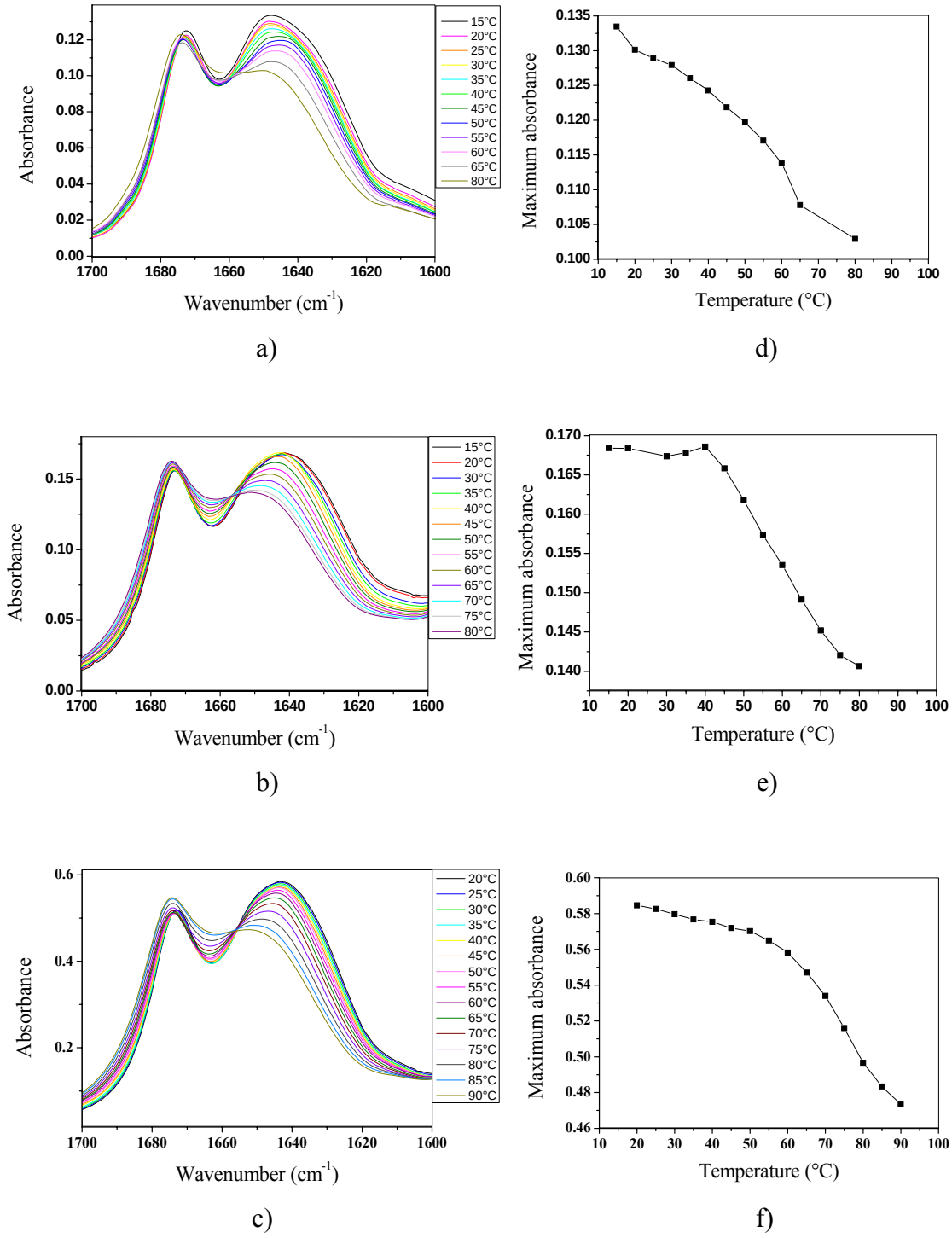

Figure 5.8 Temperature FTIR spectra of samples: a) 7 mg/ml peptide concentration, no basic fuchsin, 50 µm pathlength cell, b) 7 mg/ml peptide concentration in the presence of basic fuchsin, 50 µm pathlength cell, c) 15 mg/ml peptide concentration in the presence of basic fuchsin, 100 µm pathlength cell. Maximum absorbance in the spectral region ranging from 1620 to 1660 cm^{-1} versus temperature of samples: d) 7 mg/ml peptide concentration, no basic fuchsin, 50 µm pathlength cell, e) 7 mg/ml peptide concentration in the presence of basic fuchsin, 50 µm pathlength cell, f) 15 mg/ml peptide concentration in the presence of basic fuchsin, 100 µm pathlength cell.

The temperature dependences of the FTIR spectra are quite different for the two peptide concentrations. The mid-transition temperature of the peptide samples at 7 mg/ml is ~ 60°C whereas at 15 mg/ml concentration the melting curve is shifted to higher temperature with a mid-transition point at ~ 75°C. This is not surprising since dimer formation is expected to be favoured at higher concentrations, thus predicting higher coiled-coil stability at higher concentration.

Comparing with the melting curve from temperature-dependent CD measurements, the mid-transition temperatures in FTIR measurements are higher. This is clearly due to the fact that the peptide concentration used in the CD measurement is lower than those in FTIR measurements. However, other factors might be important, such as salt and dye concentration. As higher ionic strength increases the coiled-coil peptide stability, thus without the concentration effect, we would expect lower melting temperature in the FTIR measurements, since the solvent used in these measurements has lower ionic strength than the one used in the CD measurements.

5.4.3. Temperature jump measurements

Temperature jump measurements have been performed for the samples at two peptide concentrations: ~ 7 mg/ml and ~ 15 mg/ml with a T-jump of ~ 1°C at different starting temperatures. The sample at the peptide concentration of 7 mg/ml was studied in the copper cell for two different spacer thicknesses: 50 μm and 100μm and two different time scales: hundreds of nanoseconds and hundreds of microseconds.

Figure 5.9 shows the time-dependent absorption change on the hundreds of nanosecond time scale after a T-jump of ~ 1°C from 70°C starting temperature on a peptide sample at 7mg/ml concentration studied in a 50μm pathlength cell. We only found the effects of pressure relief which are known to occur on the same observing time scale [130]. The temperature jump induces a sudden change in pressure at the heated point, which drive the D_2O molecules inwards or outwards the heated volume, depending on the final temperature on the time scale of the pressure relief time. We observed no “frayed” helices hanging off which could be expected to melt on the 100 ns time scale as observed by Balakrishnan et al., 2006 [126] for a truncated version of GCN4. This is, however, not surprising since the single helix melting in their studies was found at low temperature (10°C) whereas their coiled-coils melted at greatly-higher temperature (40°C). Our T-jump/IR measurements were taken at high

temperatures (≥ 60°C) and thus might not be in the condition for the melting of the single helices of our coiled-coil peptide.

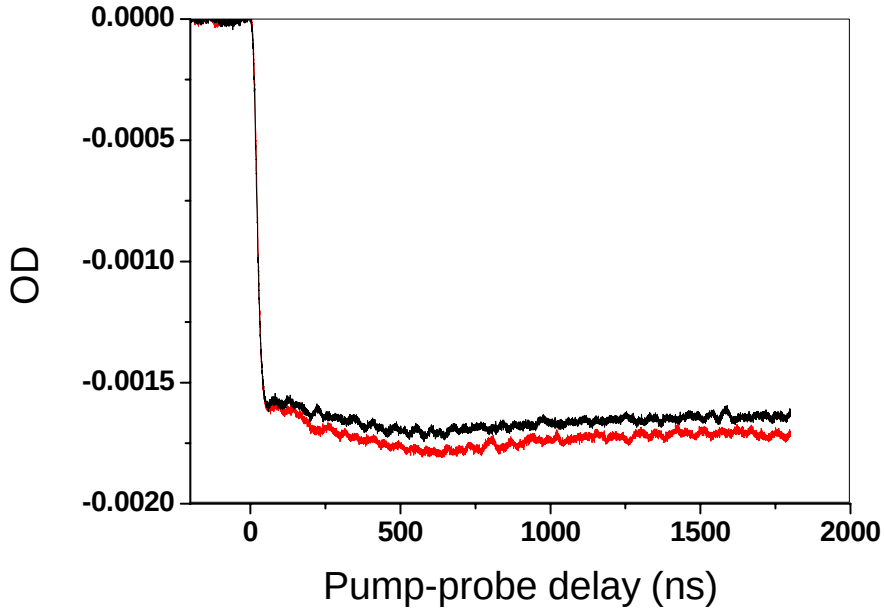

Figure 5.9 Time-dependent absorption change after a T-jump of ~ 1°C from 70°C starting temperature on a peptide sample at 7 mg/ml concentration studied in a 50μm pathlength cell. The black curves correspond to the averaged data obtained at 1592 cm^{-1} and the red curves correspond to those obtained at 1632 cm^{-1}.

However, measuring on the timescale of hundreds of microseconds, we observed a relaxation kinetics at 1632 cm^{-1} which was well-distinguished from the onset of the cooling. This kinetics is associated with the melting of helical structures. Figure 5.10 shows an example of such a temperature jump measurement which was taken on a peptide sample at 15 mg/ml concentration studied in a 100μm pathlength cell with a T-jump of ~ 1°C from 70°C starting temperature.

Due to the noticeable absorption of the coiled-coil peptide at 1592 cm^{-1}, each data set obtained at 1592 cm^{-1} and 1632 cm^{-1} was globally fitted as introduced in section 5.3.4, with values of parameters A_1, t_1, A_2 and t_2 fixed by Volk's cooling simulation for different cell pathlengths, given in table 5.3. By performing global fitting, we were able to obtain the average relaxation time constants of the unfolding dynamics of the coiled-coil peptide in two concentration conditions and studied with two different cell pathlengths (figure 5.11, table

5.4). The average relaxation times range from tens to several hundreds of microseconds, which are on the same time scale as observed for the unfolding dynamics of GCN4 [125].

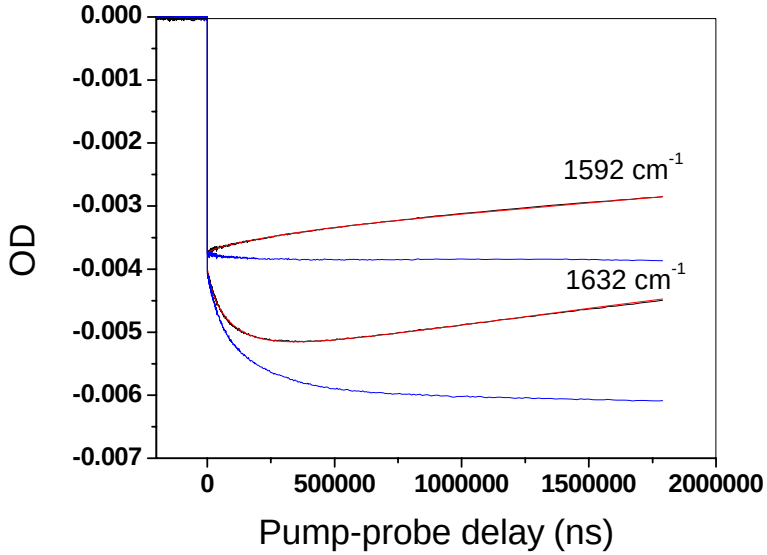

Figure 5.10 Time-dependent absorption change after a T-jump of ~ 1°C from 70°C starting temperature on a peptide sample at 15 mg/ml concentration studied in a 100µm pathlength cell. The black curves correspond to the uncorrected data at 1592 cm^{-1} and 1632 cm^{-1}. The red curves correspond to the fitting curves obtained by global fitting of data at 1592 cm^{-1} and 1632 $cm^{-1}$to equation (5.3). The blue curves correspond to the data that have been corrected for cooling.

Cell pathlength (µm)	Parameters	Values
50	A_1	0.033
	t_1	14100
	A_2	0.0906
	t_2	141700
100	A_1	0.0207
	t_1	19300
	A_2	0.067
	t_2	249000

Table 5.3 Values of fixed A_1, t_1, A_2 and t_2 parameters in global fitting of data given for two different cell pathlengths: 50 and 100 µm, determined by Volk's cooling simulation.

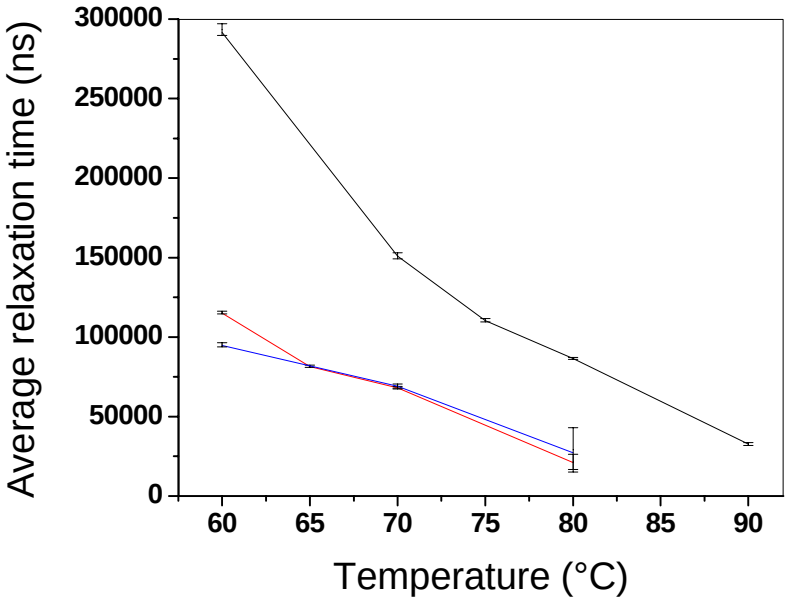

Figure 5.11 Results of temperature-dependent average relaxation times of the unfolding dynamics of the coiled-coil peptide initiated by a ~ 1°C T-jump from different starting temperatures, determined from the stretched-exponential factor of the global fit function. The black color corresponds to peptide concentration of 15 mg/ml and 100 µm pathlength cell. The red color corresponds to peptide concentration of 7 mg/ml and 100 µm pathlength cell. The blue color corresponds to peptide concentration of 7 mg/ml and 50 µm pathlength cell.

Peptide concentration (mg/ml)	Cell path length (µm)	Starting temperature (°C)	$\tau_{average}$ (µs)
15	100	60	291.6±3.7
		70	151±1.9
		75	110.5±1.1
		80	86.5±0.6
		90	32.7±0.9
7	100	60	115.1±0.9
		65	81.5±0.7
		70	68.2±0.8
		80	21±4.8
7	50	60	94.7±1.3
		70	69.1±1.4
		80	37.2±13.9

Table 5.4 Average relaxation time constants of the unfolding dynamics of the coiled-coil peptide initiated by a ~1°C T-jump from different starting temperatures determined from the stretched-exponential factor of the global fit function.

Comparing the results of the same peptide concentration of 7 mg/ml but studied with two different cell pathlengths, one receives a similar average relaxation time constant for the same starting temperature. This is reasonable and helps us verify our analysis and cooling correction of the unfolding dynamics of the coiled-coil peptide in our measurements. Note that the cooling in 50 μm path length cell is four times faster than it is in 100μm pathlength cell, yet the results are identical within the accuracy of the measurements, indicating that there is no distortion by cooling (since that would be much higher in the short path length measurement). Furthermore, one can see that the coiled-coil peptide unfolds faster when the starting temperature is higher due to the usual Arrhenius temperature-dependence.

Comparing the results of different peptide concentrations, one can notice that at the same temperature the average relaxation times for 15mg/ml peptide concentration are much greater than those for 7 mg/ml concentration.

The activation energy of the unfolding transition E_a can be determined from Arrhenius equation, which describes the temperature dependent of the rate constant:

$$\nu(T) = Ae^{-\frac{E_a}{RT}}, \tag{5.6}$$

where $\nu(T)$ is the rate constant as a function of temperature T, A is a pre-exponential factor and R is the ideal gas constant. Thus we can write its logarithmic form as follow:

$$\ln\left(\nu(T)\right) = \ln A - \left(\frac{E_a}{R}\right)\frac{1}{T}. \tag{5.7}$$

Thus we obtain following equation:

$$\ln(\tau_{average}^{-1}) = \ln A - \left(\frac{E_a}{R}\right)\frac{1}{T}. \tag{5.8}$$

Therefore, the activation energy E_a can be determined by plotting $\ln(\tau_{average}^{-1})$ against $1/T$. From figure 5.12 which shows the Arrhenius plot of the average relaxation times obtained for the two peptide concentrations, we obtain similar activation energies at the different concentrations. This proves that the difference in the kinetics comes from the difference in the pre-exponential factor A, which depends on how often the coils get in contact and whether the coils are properly oriented when they are in contact. The higher the concentration, the more often the coils get in contact. The A factor and thus the rate constant are expected to be larger. However, the observed rate constants are smaller at the higher concentration which proves that there were significantly more misaligned contacts than at the lower concentration. We

thought of a possibility that the dimer formation of two coils were misaligned by the presence of one or two other coils which came in contact with the two monomers during the course of the dimer formation. Such a possibility would increase with concentration and delay the dimer formation.

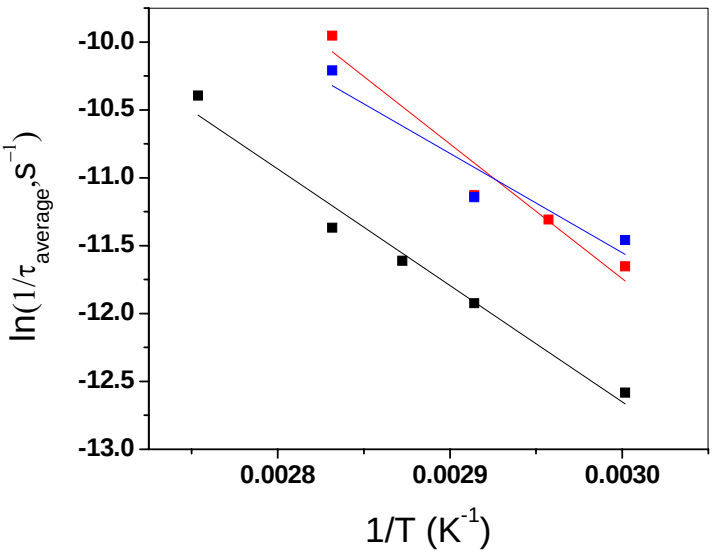

Figure 5.12 Arrhenius plot of the average relaxation of the unfolding dynamics of the coiled-coil peptide initiated by a ~ 1°C T-jump from different starting temperatures. The black dots are results for peptide concentration of 15 mg/ml and 100 µm pathlength cell. The red dots are results for peptide concentration of 7 mg/ml and 100 µm pathlength cell. The blue dots are results for peptide concentration of 7 mg/ml and 50 µm pathlength cell. The solid lines are linear fitting curves of the results of the same colors. The activation energies E_a evaluated from the fit results are 17 kcal/mol for measurements in the 100 µm pathlength cell and 15 mg/ml peptide concentration, 19.7 kcal/mol for the 100 µm pathlength cell and 7 mg/ml peptide concentration, and 14.5 kcal/mol for the 50 µm pathlength cell and 7 mg/ml peptide concentration.

Exploring the behavior of *C* parameter in the stretched-exponential factor of the global fit function, which is the measure of the net deviation from monoexponentiality (figure 5.13), we found that the coiled-coil peptide has non-monoexponential relaxation behaviors, which actually proves that the unfolding kinetics consists of more than one relaxation time constants. This is in agreement with the evidence of folding intermediates reported by previous work on other coiled-coil peptides [125, 126]. While the non-exponentiality is similar for different starting temperatures for the peptide sample at 15 mg/ml peptide concentration, for the peptide sample at lower concentration, it increases at higher starting temperatures and becomes nearly mono-exponentiality at 60°C starting temperature.

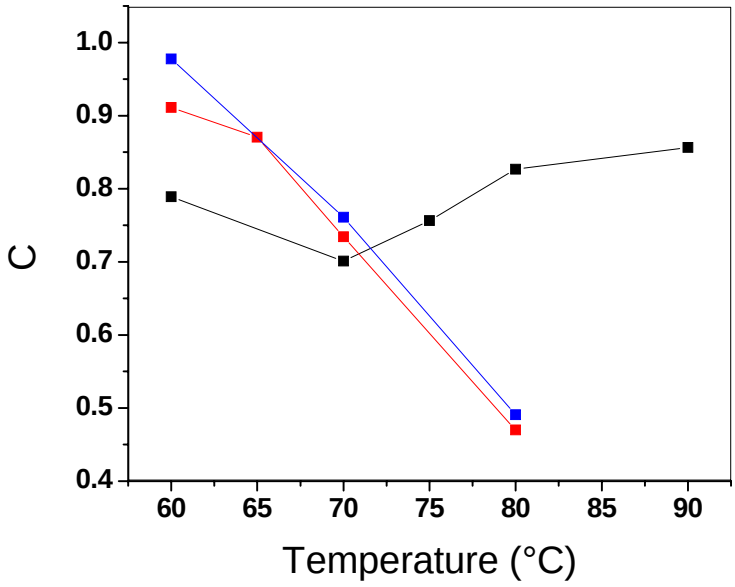

Figure 5.13 Values of C parameter determined from the stretched-exponential factor of the global fit function. The black color corresponds to peptide concentration of 15 mg/ml and 100 µm pathlength cell. The red color corresponds to peptide concentration of 7 mg/ml and 100 µm pathlength cell. The blue color corresponds to peptide concentration of 7 mg/ml and 50 µm pathlength cell.

5.5. Conclusion

Our temperature-dependent CD and FTIR measurements have shown that the leucine-zipper like coiled-coil peptide unfolds upon increasing the temperature. Temperature jump measurements with a T-jump of ~ 1°C reported an unfolding relaxation kinetics, which occurred on a hundred of microseconds time scale. Different average relaxation times were obtained at different starting temperatures. At a given starting temperature, two different average relaxation times are observed for two peptide concentrations. An Arrhenius plot of the obtained average relaxation times shows similar activation energies of the unfolding transition of the coiled-coil peptide, concluding that the difference in relaxation time constants observed at the two different peptide concentrations is due to entropy. Moreover, our results prove a non-monoexponential kinetic behavior, which identifies the existence of some intermediates during the course of the peptide unfolding.

CHAPTER 6

PICOSECOND TRANSIENT CIRCULAR DICHROISM OF THE PHOTORECEPTOR PROTEIN OF THE LIGHT-ADAPTED FORM OF BLEPHARISMA JAPONICUM

6.1. Introduction

Understanding the mechanisms underlying the light-induced responses of photomotile microorganisms represents an exciting challenge in biophysics. The ciliated protozoan Blepharisma japonicum is a well-known example of unicellular organism exhibiting a strong photomovement [131, 132], the molecular origin of which is still not fully understood. B. japonicum can be found in two forms: the dark-adapted form is red and owes its color to a benzoanthrapleiadene-dione pigment called blepharismin (BP, see figure 6.1) [133, 134]; the light-adapted form takes its blue color from oxyblepharismin (OxyBP, figure 6.1), a phenanthroperylene quinone derivative related to hypericin (Hyp, figure 6.1) [135]. Under mild white light illumination (3–30 $W.m^{-2}$), B. japonicum photoconverts from the red to the blue form by photooxidation of its pigment (BP to OxyBP) [135-137]. The cell displays a strong step-up photophobic behavior in both forms and action spectroscopy proved that it is triggered by the excitation of BP for red cells and of OxyBP for blue cells [137, 138]. Blue cells are particularly interesting because a stable chromoprotein complex of OxyBP could be extracted and purified [139, 140]. It was called Oxy-Blepharisma bInding Protein (OBIP) and was considered a good candidate for being the trigger of the photophobic response. Thorough

transient absorption and fluorescence experiments have been performed in vitro on this complex in order to decipher the primary steps of its photoactivation [141–143]. A complete account of these studies can be found in reference [143] and we give here a very short summary of the main conclusions. It appears that the chromoprotein OBIP exists in two forms, a reactive one (rOBIP) which undergoes a fast photocycle after excitation and a non-reactive one (nrOBIP) mostly behaving like the free chromophore in solution on the explored timescale. The reactive form displays a complex relaxation involving four time constants ranging from 0.5 to 133 ps, while the non-reactive species exhibits a single relaxation lifetime of 1.2 ns. The peculiar behavior of rOBIP was interpreted as follows. In this reactive form, the chromophore OxyBP was proposed to form a hydrogen bonding (HB) complex with a (as yet uncharacterized) conjugated electron-acceptor partner and to undergo electron transfer to it under photoexcitation. Photoinduced charge transfer within HB complexes between pairs of conjugated π-electron systems in nonpolar solvents has been well documented [144–146] and a model involving the proton motion along the hydrogen bond as the reaction coordinate has been proposed [146, 147]. Recent computational studies on the indole-pyridine HB complex confirm the role of a charge-transfer state connecting both the locally-excited and ground states and of the proton shift as the reaction coordinate along which excited-state deactivation proceeds [148]. In the case of rOBIP, an equilibrium between the locally-excited state and the charge-transfer state of the complex was hypothesized to occur very rapidly (sub-ps, few ps regime) and then evolves as a response to changes in the protein environment, which are themselves induced by the charge-transfer process. This relaxation process along two coordinates (proton shift and protein local conformation) is schematically depicted in figure 6.2.

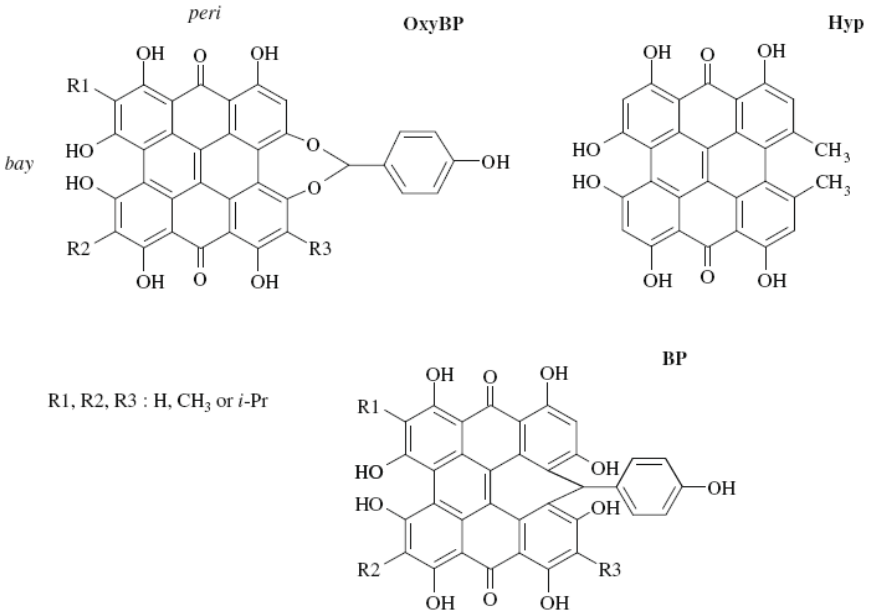

Figure 6.1 Chemical structures of oxyblepharismin (OxyBP), its close parent hypericin (Hyp) and its natural precursor blepharismin (BP). The five isospectral forms of OxyBP and BP only differ by their alkyl lateral substituents (Ri) [134].

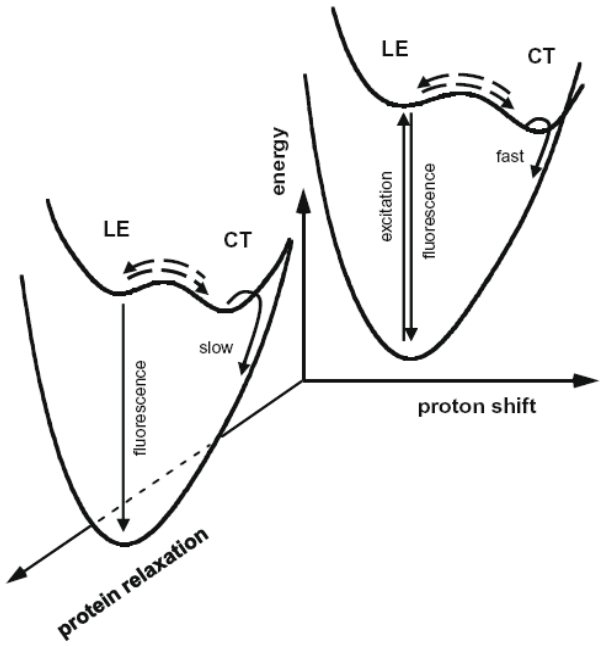

Figure 6.2 Schematic view of the photoinduced reaction mechanism proposed for the reactive form of the chromoprotein OBIP, from previous femtosecond time-resolved transient absorption experiments [139]. The chromophore OxyBP would form a hydrogen bonded complex with a nearby electron acceptor of the protein residues. Photoexcitation of the chromophore leads to a rapid equilibrium with a non fluorescent charge-transfer state of the complex. The environmental response affects the decay kinetic. The potential energy curves were inspired from reference [146].

The previous work relied on electronic absorption spectroscopy. However, as both the OxyBP chromophore and the OBIP protein are chiral molecules, they also display a circular

dichroism activity [149]. Taking advantage of the picosecond time-resolved CD set-up which has been previously developed in the Laboratory [101, 102, 150], we have investigated the dynamics of the pump-induced CD in OxyBP and OBIP in the far UV, a spectral range which is of interest not only for the chromophore, but also for the protein backbone since it corresponds to the signature of alpha helices in the CD spectra. In previous steady-state experiments [149], from the CD spectra measured in the far UV, it was proposed that the presence of OxyBP induces a slight increase in the alpha helices content of the protein matrix, indicating that the chromophore strongly interacts with its apoprotein. In the present preliminary experiments one will not probe the slow helical conformational changes that may occur after photoexcitation of the chromophore. However a local structural response is expected to be involved in the previously hypothesized mechanism of ultrafast electron transfer, from the photoexcited chromophore to a nearby residue [143].

This work was made in close collaboration with Monique Martin and Pascal Plaza from the Laboratoire de Chimie de l'Ecole Normale Supérieure de Paris who have performed most of the aforementioned time-resolved spectroscopy on this system.

6.2. Materials and sample preparation

The samples were given to us by Pascal Plaza. Purified OBIP and OxyBP samples were prepared by F. Lenci from the Istituto di Biofisiaca de Pise following the protocols explained in references [141–143, 151]:

Red Blepharisma japonicum cells were grown in the dark at 23°C in the presence of Enterobacteraerogenes. The blue (light-adapted) cells were produced by in vivo photoconversion under a low intensity cold white lamp (< 10 $W.m^{-2}$) for several days. These blue cells then were washed, collected by low speed centrifugation, and resuspended in a 20 $mmom.L^{-1}$ sodium cholate solution. The OBIP chomoprotein was purified by liquid chromatography of the sodium cholate solution containing the blue cells on a hydroxyapatide column.

Our OBIP samples were prepared in a 0.2 $mol.L^{-1}$ phosphate buffer (pH 7.4) containing 10 $mmol.L^{-1}$ sodium cholate and 100 $mmol.L^{-1}$ sodium chloride. OxyBP sample was dissolved in pure ethanol.

6.3. Experimental details

6.3.1. Experimental set-up

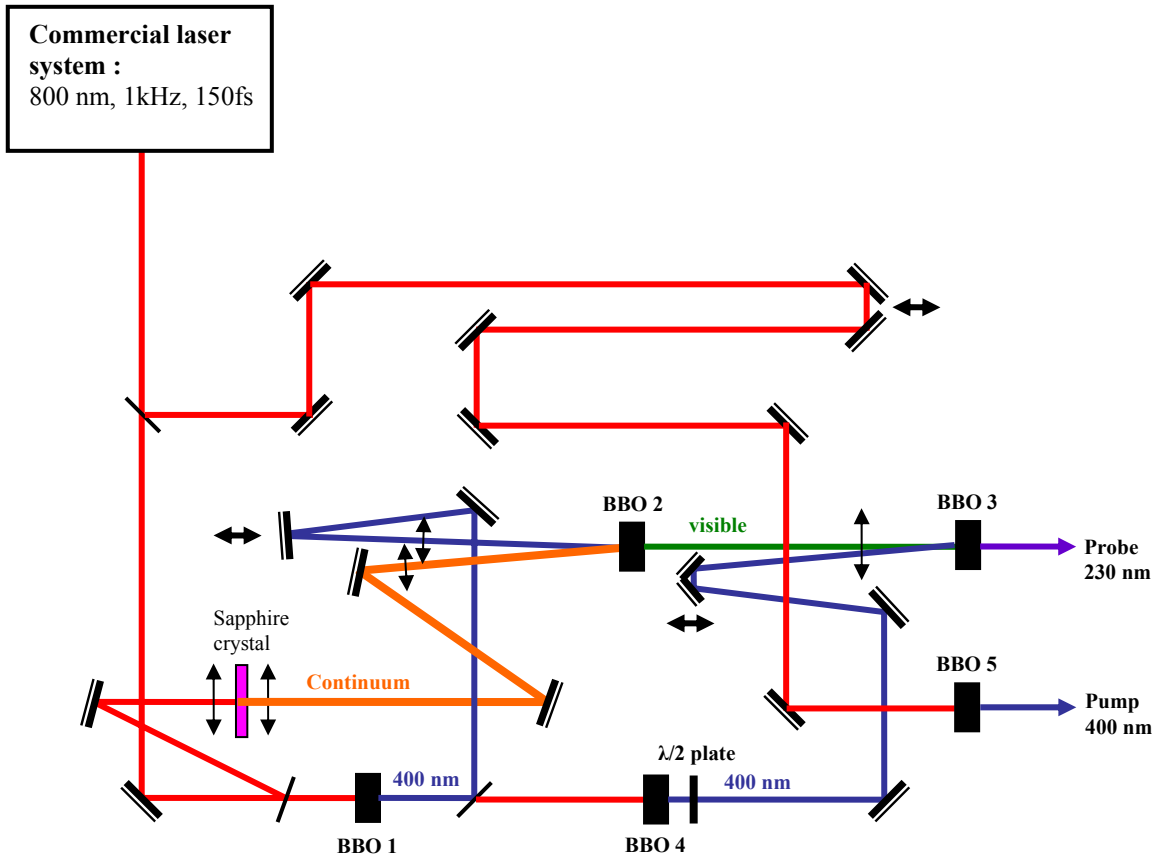

Figure 6.3 Schematic representation of the pump/probe source system.

CD dynamics is obtained in the picosecond time-resolved CD experiment that has been previously developed during Claire Niezborala's PhD project [101, 102, 150]. The principle of the experimental set-up is a pump–probe experiment based on our femtosecond Titanium–Sapphire laser system described in chapter 2. Photoexcitation of the chromophore was performed at 400 nm with the second harmonic of the laser (figure 6.3). Note that no excitation of the protein can occur at this wavelength (see absorption spectrum of OBIP in latter section). Pump pulse energy was about 0.5 µJ. The probe wavelength was fixed at 230 nm. The probe beam was obtained in the same manner with the generation of the UV probe beam for our nanosecond T-jump experiment described in chapter 2. Probe pulse energy was in the nJ range, which is sufficient for detection of the transmitted signal and low enough to avoid UV-related damages. Schematic representation of the pump/probe source system is displayed in figure 6.3.

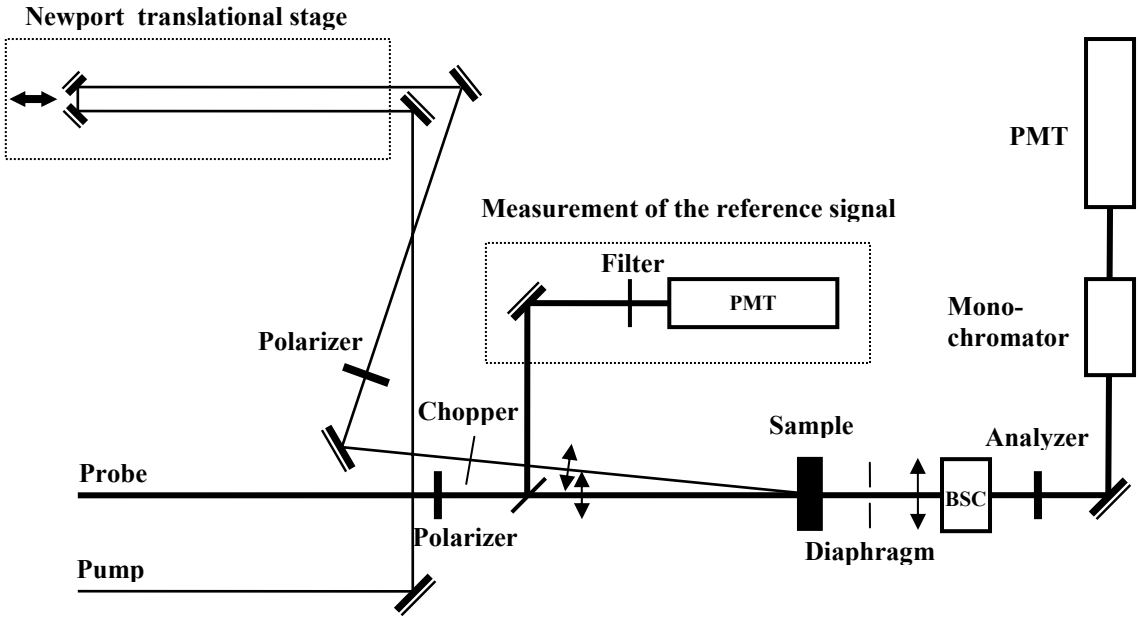

Figure 6.4 Schematic representation of the picosecond pump-probe experimental set-up.

The pump and probe beams were focused onto the sample with 20 cm focal length lenses. To obtain pump and probe polarizations to be linearly polarized like one another, a polarizer was placed on each pump and probe path. In order to access the CD, the sample was placed between the polarizer on the probe beam path and a crossed analyzer. A Babinet-Soleil compensator (BSC) was then inserted between the sample and the analyzer. BSC is a passive optical device which acts as a tunable retardation plate. Fine tuning of this retardation was made with 3.7×10^{4} rad (0.21°) rotation steps. Measuring transmitted probe intensity as a function of this retardation allows precise measurement of the beam ellipticity. The principle of the experiment is the following. A mechanical chopper is inserted on the pump path. This pump modulation induces a modulation of the ellipticity of the probe which is extracted with a lock-in amplifier. Very simple algebra, detailed in latter paragraph, shows that this ellipticity modulation straightforwardly yields the pump-induced absorption and CD at the same time. Measurements therefore consist in obtaining the ellipticity changes by monitoring the probe transmission and its modulation as a function of the BSC retardation and extracting the changes in absorption and CD for a given pump–probe delay. Pump–probe delay is then carefully controlled by a Newport translation stage. Delays up to 1.2 ns are readily usable. The pump-probe experiment set-up is depicted in figure 6.4. The transmitted probe intensity was measured by a photomultiplier tube (PMT, Electron Tubes 9402) and a Boxcar analyzer (Stanford SR250). Elimination of optical noise was done with the use of a monochromator

before the PMT. Normalization of the signal with the help of a reference beam measured by another PMT was performed in order to reduce the effects of laser fluctuations.

6.3.2. Optimization of pump/probe overlap

Optimization of the overlap of the pump and probe beams in a pump-probe experiment is of utmost importance to be able to detect the signal induced by the presence of the pump pulses and to obtain a good signal to noise ratio. Precise alignment of the pump and the probe beam was achieved by taking advantage of a two-photon absorption phenomenon in a cyclohexane solvent. Indeed, considering the wavelengths involved in the experiment, a two-photon absorption phenomenon (one pump photon plus one probe photon) generally takes place. This is illustrated in figure 6.5 where the pump-induced absorption change of the probe is plotted as a function of pump–probe delay in a neat cyclohexane sample. The dip in the transmission profile is due to two-photon absorption, which only occurs when the pump and the probe pulses overlap. Finely adjusting the two lenses used for focusing the pump and the probe beams into the sample to maximize the two photo absorption signal allows optimization of the pump/probe beam spatial overlap. From the curve shown in figure 6.5, we can get two useful pieces of information: the zero-delay between pump and probe, which is clearly determined at the maximum of the dip, and the pump–probe cross-correlation time, of about 1.8 ps, which is given by the width of the dip. This latter time gives the best time resolution that one can achieve with this set-up. This measurement allows us to straightforwardly obtain a very precise spatial and temporal alignment of the beams.

Besides these practical features, the two-photon absorption phenomenon however has a deleterious effect: in all common solvents, including water and ethanol used in this work, it overlaps and therefore obscures any measurement of a genuine molecular signal for delays shorter than 2 ps. We however describe in latter section (transient CD results) a fitting procedure helping to partially overcome this difficulty.

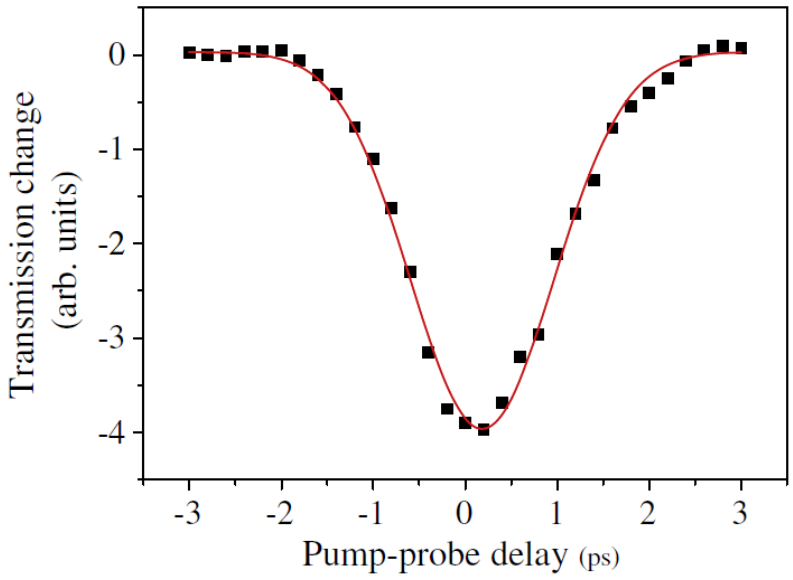

Figure 6.5 Two photon absorption of pure cyclohexane observed when the pump and probe pulses overlap in the sample, showing the zero-delay and the pump-probe cross-correlation time of the pump-probe experiments.

6.3.3. Calculation of absorption and circular dichroism variations induced by the pump

6.3.3.1. Probe alone: Jones matrix analysis

Let (x,y) be the laboratory frame. x (respectively, y) corresponds to the vertical (respectively, horizontal) direction. Consider an incoming laser field which is vertically polarized along x axis:

$$E_{in} = E_0 \begin{pmatrix} 1 \\ 0 \end{pmatrix}, \tag{6.1}$$

where E_0 is the vibration amplitude. After passing the sample, Babinet-Soleil compensator and analyzer, the outcoming electric field is read as

$$E_{out} = M_{Analyzer} M_{BSC} M_{Sample} E_{in}, \tag{6.2}$$

where M_{Sample} describes the response of the sample taking optical activity into account and M_{BSC} and $M_{Analyzer}$ describe the action of the Babinet-Soleil compensator and analyzer respectively. The crossed analyzer is in y direction, so can be simply written as

$$M_{Analyzer} = \begin{pmatrix} 0 & 0 \\ 0 & 1 \end{pmatrix}. \tag{6.3}$$

Supposing the Babinet-Soleil compensator is oriented at 45° compared to the laboratory frame and calling 2X its retardation, we can write its matrix as

$$M_{BSC} = R(-45°)M_X R(45°), \tag{6.4}$$

where *R(±45°)* introduce the rotations of ±*45°* angles and M_X the retardation. Hence, we have

$$M_{BSC} = \begin{pmatrix} \cos(-45°) & -\sin(-45°) \\ \sin(-45°) & \cos(-45°) \end{pmatrix} \begin{pmatrix} e^{-iX} & 0 \\ 0 & e^{iX} \end{pmatrix} \begin{pmatrix} \cos(45°) & -\sin(45°) \\ \sin(45°) & \cos(45°) \end{pmatrix} \tag{6.5}$$

$$= \begin{pmatrix} \cos X & i\sin X \\ i\sin X & \cos X \end{pmatrix}. \tag{6.6}$$

Let n_L, n_R, α_L and α_R the refractive indices and the absorption coefficients for the left and right circular polarization. We define the optical rotation (θ) as

$$\theta = \frac{\pi}{\lambda}(n_L - n_R)l \tag{6.7}$$

and the CD as

$$\eta = (\alpha_L - \alpha_R)l, \tag{6.8}$$

where l is the sample thickness. As said in section 1.2.7, we can decompose the vertically polarized incident wave as the sum of a left-circularly polarized wave and a right-circularly polarized wave. The electric field after passing through the sample then can be defined as

$$E_{Sample} = \frac{E_0}{2} e^{i\frac{2\pi}{\lambda}n_L l} e^{-\frac{\alpha_L l}{2}} \begin{pmatrix} 1 \\ i \end{pmatrix} + \frac{E_0}{2} e^{i\frac{2\pi}{\lambda}n_R l} e^{-\frac{\alpha_R l}{2}} \begin{pmatrix} 1 \\ -i \end{pmatrix} \tag{6.9}$$

$$= \frac{E_0}{2} e^{i\frac{2\pi}{\lambda}nl} e^{-\frac{\alpha l}{2}} \begin{pmatrix} e^{-i\theta} e^{-\frac{\eta}{4}} + e^{i\theta} e^{\frac{\eta}{4}} \\ i(e^{-i\theta} e^{-\frac{\eta}{4}} - e^{i\theta} e^{\frac{\eta}{4}}) \end{pmatrix} \tag{6.10}$$

$$= E_0 e^{i\frac{2\pi}{\lambda}nl} e^{-\frac{\alpha l}{2}} \begin{pmatrix} \cosh\left(\frac{\eta}{4} + i\theta\right) \\ -i\sinh\left(\frac{\eta}{4} + i\theta\right) \end{pmatrix}, \tag{6.11}$$

where $n = \frac{n_L + n_R}{2}$ and $\alpha = \frac{\alpha_L + \alpha_R}{2}$ are the average refractive index and average absorption coefficient, respectively. We then can define the sample matrix M_{Sample} from following equation:

$$E_{Sample} = M_{Sample}\left(\frac{E_0}{2}\begin{pmatrix} 1 \\ i \end{pmatrix} + \frac{E_0}{2}\begin{pmatrix} 1 \\ -i \end{pmatrix}\right). \tag{6.12}$$

Thus we obtain

$$M_{Sample} = e^{i\frac{2\pi}{\lambda}nl} e^{-\frac{\alpha l}{2}} \begin{pmatrix} \cosh\left(\frac{\eta}{4}+i\theta\right) & i\sinh\left(\frac{\eta}{4}+i\theta\right) \\ -i\sinh\left(\frac{\eta}{4}+i\theta\right) & \cosh\left(\frac{\eta}{4}+i\theta\right) \end{pmatrix}. \tag{6.13}$$

Note that in this matrix, we take both effects of optical rotation and circular dichroism into account. Supposing θ, η and X are very small numbers, we can write the outcoming electric field found in equation (6.2) as

$$E_{out} = E_0 e^{i\frac{2\pi}{\lambda}nl-\frac{\alpha l}{2}} \begin{pmatrix} 0 & 0 \\ 0 & 1 \end{pmatrix} \begin{pmatrix} 1 & iX \\ iX & 1 \end{pmatrix} \begin{pmatrix} 1 & -\theta+i\frac{\eta}{4} \\ \theta-i\frac{\eta}{4} & 1 \end{pmatrix} \begin{pmatrix} 1 \\ 0 \end{pmatrix} \tag{6.14}$$

$$= E_0 e^{i\frac{2\pi}{\lambda}-\frac{\alpha l}{2}} \begin{pmatrix} 0 \\ \theta+i\left(X-\frac{\eta}{4}\right) \end{pmatrix}. \tag{6.15}$$

In terms of intensity, we obtain

$$I_{out} = \left|E_0\right|^2 e^{-\alpha l}\left[\theta^2+\left(X-\frac{\eta}{4}\right)^2\right]. \tag{6.16}$$

From equation (6.16), one can notice that if there is no sample (or if the sample is nonchiral), $\theta = 0$ and $\eta = 0$ therefore $I_{out} = 0$ when $X = 0$. Changing the BSC retardation X yields a parabola versus X. When a chiral sample is inserted, the parabola shift. The shifts directly give θ and η. To measure the optical rotation and circular dichroism with this technique in practical however is not very efficient because it requires a very high precision on the position of the parabola minimum, which is very challenging. However, in a pump-probe experiment, this limitation is lifted if one is interested in the variation of the optical rotation and circular dichroism. This matter will be presented in next paragraph.

6.3.3.2. Pump-probe experiment

When the pump is sent to the sample, it induces a change in absorption, optical rotation and circular dichroism. Calling $\Delta\alpha$, $\Delta\theta$ and $\Delta\eta$ the change in absorption, optical rotation and CD due to the pump, we can write the intensity of outcoming electric field without pump as

$$I_{withoutpump} = I_0\left[\theta^2+Y^2\right], \tag{6.17}$$

where $I_0 = |E_0|^2 e^{-\alpha l}$ and $Y = X - \frac{\eta}{4}$ and the outcoming electric field with pump as

$$I_{withpump} = I_0 e^{-\Delta\alpha l}\left[(\theta + \Delta\theta)^2 + \left(Y + \frac{\Delta\eta}{4}\right)^2\right]. \tag{6.18}$$

Let now consider the experiment case where the pump is modulated by the mechanical chopper. We measure the photomultiplier signal (*PMT*), which is the average of $I_{withoutpump}$ and $I_{withpump}$ and the modulated part of the *PMT* signal obtained with the lock-in amplifier, which we call *LI* signal and is equal to the difference between $I_{withpump}$ and $I_{withoutpump}$. From the equations (6.17) and (6.18), we obtain

$$PMT = \frac{1}{2}\left(I_0\left[\theta^2 + Y^2\right] + I_0 e^{-\Delta\alpha l}\left[(\theta + \Delta\theta)^2 + \left(Y + \frac{\Delta\eta}{4}\right)^2\right]\right) \tag{6.19}$$

$$= \frac{I_0}{2}\left[\left(1 + e^{-\Delta\alpha l}\right)Y^2 + e^{-\Delta\alpha l}\frac{\Delta\eta}{2}Y + e^{-\Delta\alpha l}\frac{\Delta\eta^2}{16} + \left(\theta^2 + e^{-\Delta\alpha l}(\theta + \Delta\theta)^2\right)\right] \tag{6.20}$$

and

$$LI = I_0 e^{-\Delta\alpha l}\left[(\theta + \Delta\theta)^2 + \left(Y + \frac{\Delta\eta}{4}\right)^2\right] - I_0\left[\theta^2 + Y^2\right] \tag{6.21}$$

$$= I_0\left[\left(-1 + e^{-\Delta\alpha l}\right)Y^2 + e^{-\Delta\alpha l}\frac{\Delta\eta}{2}Y + e^{-\Delta\alpha l}\frac{\Delta\eta^2}{16} + \left(-\theta^2 + e^{-\Delta\alpha l}(\theta + \Delta\theta)^2\right)\right]. \tag{6.22}$$

Calling $K_1 = \theta^2 + e^{-\Delta\alpha l}(\theta + \Delta\theta)^2$ and $K_2 = -\theta^2 + e^{-\Delta\alpha l}(\theta + \Delta\theta)^2$, we rewrite the equations (6.21) and (6.22) as

$$PMT = \frac{I_0}{2}\left[\left(1 + e^{-\Delta\alpha l}\right)Y^2 + e^{-\Delta\alpha l}\frac{\Delta\eta}{2}Y + e^{-\Delta\alpha l}\frac{\Delta\eta^2}{16} + K_1\right], \tag{6.23}$$

$$LI = I_0\left[\left(-1 + e^{-\Delta\alpha l}\right)Y^2 + e^{-\Delta\alpha l}\frac{\Delta\eta}{2}Y + e^{-\Delta\alpha l}\frac{\Delta\eta^2}{16} + K_2\right]. \tag{6.24}$$

Since the crossed-analyzer angle is fixed in y direction, θ stays constant when the retardation X and thus Y vary. K_1 and K_2 are therefore constant. From the equations (6.23) and (6.24), one can see that the *PMT* and *LI* versus Y are parabolas. The important point here is that the two parabolas of *PMT* and *LI* don't have the same minimum position. To make this clear, we simplify the two equations (6.23) and (6.24) by defining a new variable:

$$Z = Y + \frac{\Delta\eta e^{-\Delta\alpha l}}{4\left(e^{-\Delta\alpha l} + 1\right)}. \tag{6.25}$$

Note that the transformations from X to Y and to Z involve only shifts from the origin but does not involve the change of the scale. Hence, we obtain

$$PMT = \frac{I_0}{2}\left[\left(1+e^{-\Delta\alpha l}\right)Z^2 - \frac{\Delta\eta^2 e^{-2\Delta\alpha l}}{16(e^{-\Delta\alpha l}+1)} + K_1\right], \tag{6.26}$$

$$LI = I_0\left[\left(-1+e^{-\Delta\alpha l}\right)Z^2 + \frac{\Delta\eta e^{-\Delta\alpha l}}{e^{-\Delta\alpha l}+1}Z + \left(3e^{-\Delta\alpha l}+1\right)\frac{\Delta\eta^2 e^{-2\Delta\alpha l}}{16\left(e^{-\Delta\alpha l}+1\right)} + K_2\right]. \tag{6.27}$$

Dividing the two equations (6.26) and (6.27) by the same multiplicative constant $\frac{I_0}{2}\left(1+e^{-\Delta\alpha l}\right)$, we have

$$PMT = Z^2 - \frac{\Delta\eta^2 e^{-2\Delta\alpha l}}{16(e^{-\Delta\alpha l}+1)^2} + \frac{K_1}{(e^{-\Delta\alpha l}+1)}, \tag{6.28}$$

$$LI = 2\frac{e^{-\Delta\alpha l}-1}{e^{-\Delta\alpha l}+1}Z^2 + \frac{2\Delta\eta e^{-\Delta\alpha l}}{\left(e^{-\Delta\alpha l}+1\right)^2}Z + \left(3e^{-\Delta\alpha l}+1\right)\frac{\Delta\eta^2 e^{-2\Delta\alpha l}}{8\left(e^{-\Delta\alpha l}+1\right)^2} + \frac{2K_2}{e^{-\Delta\alpha l}+1}. \tag{6.29}$$

Calling $K_3 = \frac{\Delta\eta^2 e^{-2\Delta\alpha l}}{16(e^{-\Delta\alpha l}+1)^2} + \frac{K_1}{(e^{-\Delta\alpha l}+1)}$ and $K_4 = \left(3e^{-\Delta\alpha l}+1\right)\frac{\Delta\eta^2 e^{-2\Delta\alpha l}}{8\left(e^{-\Delta\alpha l}+1\right)^2} + \frac{2K_2}{e^{-\Delta\alpha l}+1}$, one get

$$PMT = Z^2 + K_3, \tag{6.30}$$

$$LI = 2\frac{e^{-\Delta\alpha l}-1}{e^{-\Delta\alpha l}+1}Z^2 + \frac{2\Delta\eta e^{-\Delta\alpha l}}{\left(e^{-\Delta\alpha l}+1\right)^2}Z + K_4. \tag{6.31}$$

From these expressions, one can clearly see that comparing the two parabolas of *PMT* and *LI* directly yields $\Delta\alpha$ and η. In the case where $\Delta\alpha l \ll 1$, the *LI* signal is reduced to

$$LI = -\Delta\alpha l Z^2 + \frac{\Delta\eta}{2}Z + K_5. \tag{6.32}$$

From the equations (6.30)-(6.32), one can see that plotting the PMT and LI signal on the same graph gives two parabolas with different curvatures and minimum positions. The change in curvatures yields the change in absorption induced by the pump. The shift of the LI parabola compared with the PMT parabola gives $\frac{\Delta\eta}{4\Delta\alpha l}$. This shift is important in our consideration because the ratio can be quite large and can be easily measurable if the change in absorption is weak. The change in CD is then simply obtained by multiplication of the shift of the LI parabola by four times of the change in parabola curvature.

6.3.4. Sample cell

For all pump-probe measurements, the samples were placed in a 1 mm pathlength quartz cell. The cell was held on a rotational stage and continuously rotated during experiments to avoid cumulative heat effects and sample degradation. With these conditions, no degradation was observed during the experiments.

6.4. Results and discussions

6.4.1. Absorption spectra

Figure 6.6 shows the absorption spectra of our OBIP and OxyBP samples. As one can see, the optical density of the OBIP and OxyBP samples at the redmost absorption peaks was 0.52 and 0.2, respectively. Using the value of molar extinction coefficient ε = 22350 $M^{-1}cm^{-1}$ provided from reference [149], which was assumed to be approximately the same for OBIP and OxyBP, we can estimate the corresponding chromophore concentrations of about 2.33×10^{-4} and 8.95×10^{-4} $mol.L^{-1}$ for our OBIP and OxyBP sample, respectively. With the pump pulse energy E of about 0.5 μJ, the energy absorbed per pulse by the OBIP sample is calculated as follow:

$$E_{absorbed} = E\left(1 - e^{-2.3A_{OBIP}}\right), \tag{6.33}$$

where A_{OBIP} = 0.52 is the absorbance of OBIP at the pump wavelength of 400 nm. Thus we get $E_{absorbed} \approx 0.35\times10^{-6}$ (J). Number of excited molecules is evaluated by

$$N_{excited} = \frac{E_{asborbed}}{E_{quantum}}, \tag{6.34}$$

where $E_{quantum}$ is the quantum energy defined by

$$E_{quantum} = \frac{hc}{\lambda}, \tag{6.35}$$

where $h = 6.626\times10^{-34}$ (J.s) is the Plank constant, $c = 2.998\times10^{8}$ ($m.s^{-1}$) is the speed of light in vacuum and $\lambda = 400\times10^{-9}$ (m). Hence, we obtain $N_{excited} \approx 7\times10^{11}$ (molecules). Then we can evaluate the percentage of excited molecules as follow:

$$Pe = \frac{N_{excited}}{N}, \tag{6.36}$$

where N is the number of molecules present in the pumped volume and can be calculated as

$$N = CV_{pumped}N_A, \tag{6.37}$$

where $C = 2.33\times10^{-4}$ mol.L^{-1} is the sample concentration, $N_A = 6.022\times10^{23}$ is the Avogadro constant and V_{pumped} is the volume of the sample under pump irradiation. V_{pumped} can be estimated if we assume the pumped volume has cylindrical shape. Knowing the pump focus radius $r_{pump} \approx 50$ (μm), we have

$$V_{pumped} = \pi r_{pump}^2 l \approx 7.85\times10^{-12} \text{ (m}^3\text{)} \approx 7.85\times10^{-9} \text{ (L)}.$$

From equation (6.37), we calculate $N \approx 1.1\times10^{12}$ (molecules). Thus, one can estimate that about 63% of the molecules were excited.

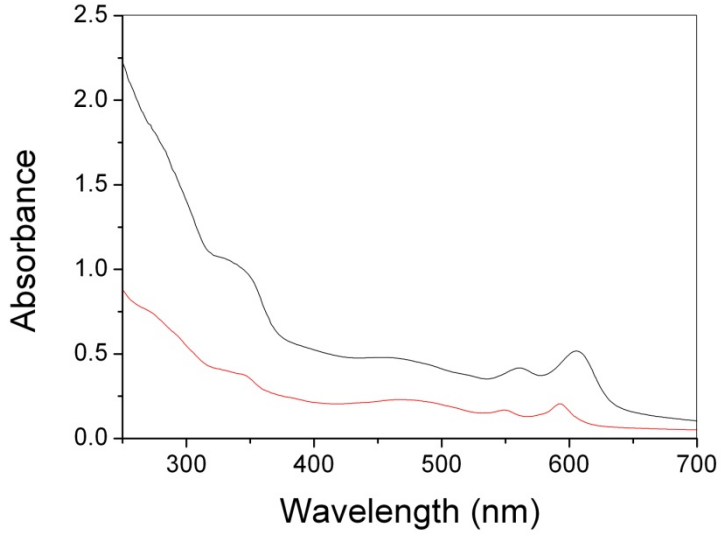

Figure 6.6 Absorption spectra of our OBIP (black curve) and OxyBP (red curve) samples.

6.4.2. Pump-probe experiments

In figure 6.7, we plotted the time-dependence of the OBIP differential absorption (δA) following excitation (difference between the absorption of the excited sample, at time t, and of the unexcited sample). These δA values are very weak and at most amount to only a fraction of percent of the steady-state absorption at 230 nm (A = 2.8). Since one expects about 63% of the molecules to get excited, this indicates that both bleaching and excited-state absorption must play a role at this wavelength and strongly cancel one another. Looking at figure 6.7a and b, one can clearly observe a multi-time dynamics in the δA kinetic traces. A multiexponential fit yields three time constants, namely: 1.6 ps, 50 ps and 1.3 ns. Because the signal to noise ratio is not so good, these times are only indicative. They however compare well with the time constants measured in the previous visible transient absorption experiments

[141–143]. The nanosecond time can in particular be confidently assigned to the non-reactive form of OBIP for which a 1.2 ns lifetime was reported [143]. On the other hand, the 1.6 ps and 50 ps fall respectively in the ranges of the 0.5 ps and 3.7 ps and the 29 ps and 133 ps components found for the reactive form of OBIP [143].

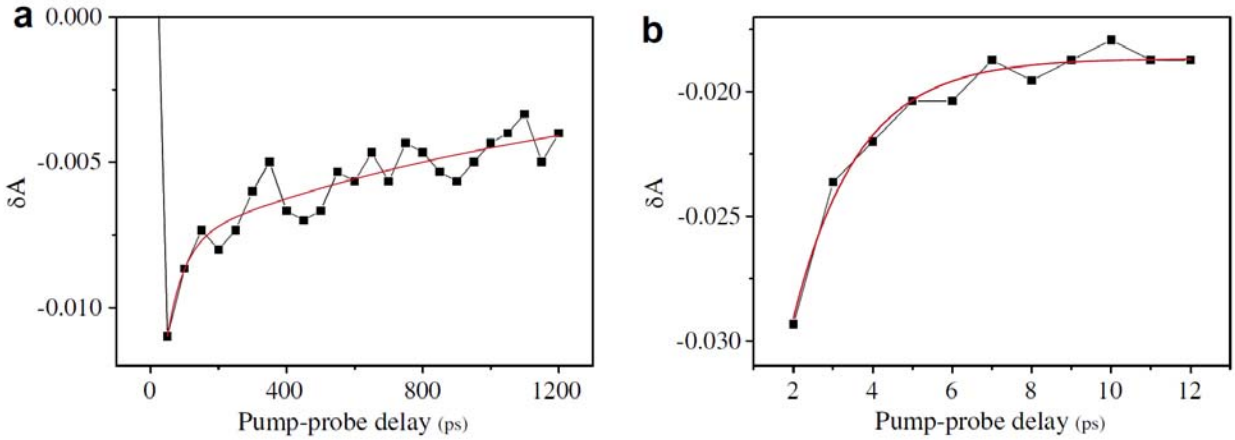

Figure 6.7 Time-resolved transient absorption (δA) of the chromoprotein OBIP sample: (a) up to 1.2 ns after excitation, (b) within 12 ps. Note that the two curves correspond to two different pump energies.

We come now to the results we have obtained for the time-resolved CD measurements (at 230 nm). Figure 6.8 displays the CD changes (δCD) induced by the excitation pulse as a function of pump–probe delay. As in transition absorption spectroscopy, the transient CD signal may contain a contribution due to the bleaching of the ground-state CD. Unfortunately, because both the chromophore and the protein backbone absorb at this wavelength it is not possible to separate out the various contributions. The experimental points are rather dispersed. Two factors explain this high uncertainty. First, δCD is weak by itself (in the 10^{-4} range) and second, extraction of the pump-induced ellipticity is experimentally more difficult when the absorption change is low. Nevertheless, the relaxation process that is visible in figure 6.8 is reproducible. These data were fitted to a sum of one exponential decay and a plateau, convoluted by a Gaussian function representing the response function of the apparatus. The presence of an artifact during pump–probe overlap was empirically taken into account by adding the same Gaussian function to the sum. The origin of this artifact lies in the birefringence induced by the anisotropy of the two-photonsusceptibility tensor. Effects of induced birefringence on CD measurements have been described in section 2.4. The width and peak position of the Gaussian function were imposed to the value precisely determined by the fit of figure 6.5. The fit of figure 6.8 gives a time constant of 2.2 ± 0.9 ps, in agreement with the shortest lifetime measured for the transient absorption decay at the same wavelength

(230 nm). We tried to measure the δCD kinetics on longer timescale but no clear signal was observed under the present conditions.

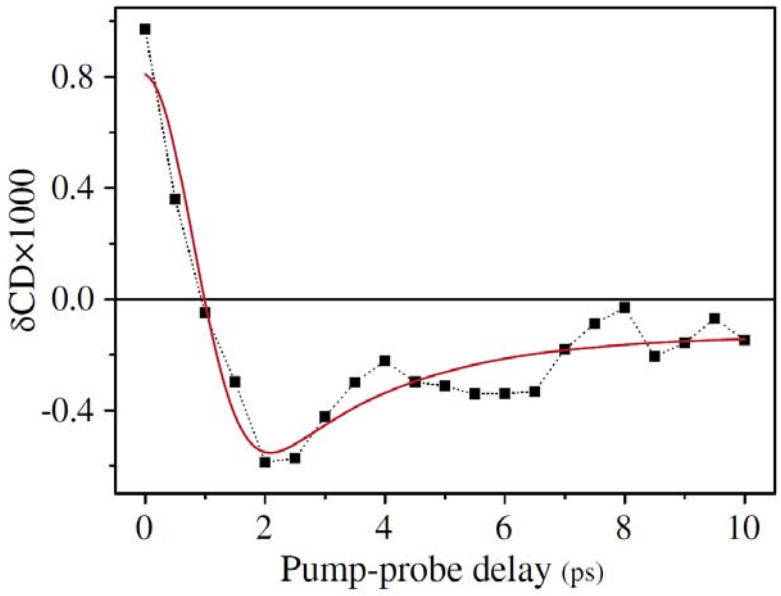

Figure 6.8 Time-resolved change in the circular dichroism (δCD) of the chromoprotein OBIP sample within 10 ps after excitation. The solid line is a fit taking into account the pump-probe overlap artefact.

For the sake of comparison, we also carried out the measurement for the OxyBP chromophore alone. The change in CD is weaker in OxyBP than in OBIP under similar experimental conditions, revealing a first difference between the two compounds. But the most interesting feature is displayed in figure 6.9. Even though a similar negative δCD signal appears instantaneously after the pump excitation for both the free OxyBP and OBIP samples, the signal remains constant for OxyBP whereas a strong relaxation is observed in OBIP. Such a behavior is also observable in the differential absorption curves (see the inset in figure 6.9): δAbs remains constant in OxyBP on this timescale. Note that such clear differences were also well identified in the visible region [141–143].

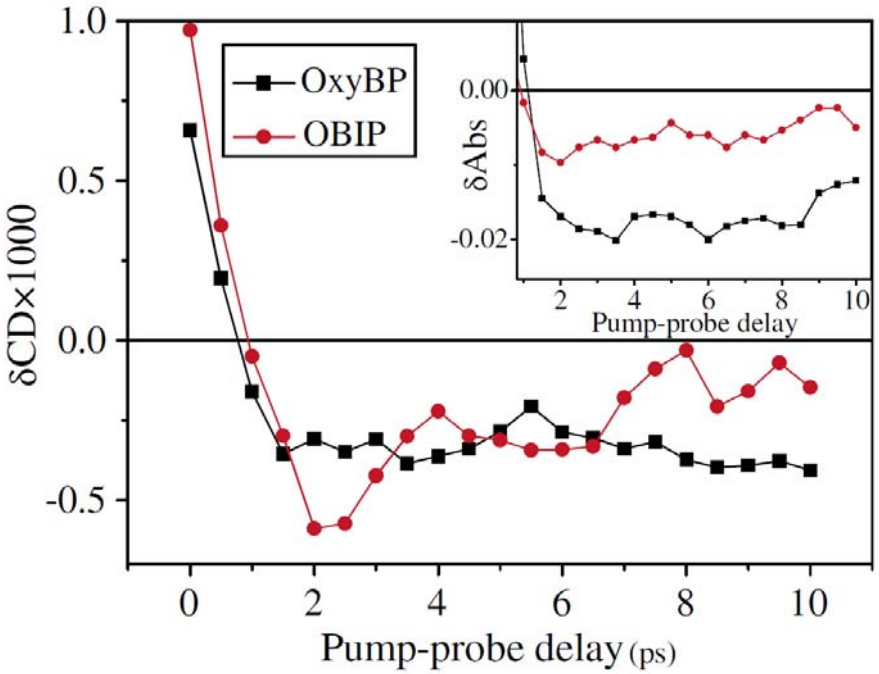

Figure 6.9 Comparison of the time-resolved circular dichroism (δCD) of the chromoprotein OBIP and of the chromophore OxyBP isolated in solution, emphasizing the rapid photoinduced changes when the chromophore is interacting with its native protein partner. The inset shows the corresponding transient absorption curves.

6.4.3. Discussion

The first question is to determine the origin of the CD change that we measure. The answer to this question is by no means easy. It is in particular known that the major part of the steady-state CD signal at 230 nm comes from the alpha helices in the protein backbone [149]. One could therefore expect a strong contribution of the protein in the CD changes. However, the fact that OBIP and OxyBP behave in the same way right after the excitation demonstrates that the δCD signal we observe mainly comes from the chromophore. Actually, this feature looks quite reasonable because it is not expected that the protein backbone undergoes noticeable conformational changes on a short timescale. We can thus confidently assign the CD changes we observe to the chromophore. Since the chromophore is known to be a chiral molecule [149], it is not surprising that the aforementioned excited-state absorption is accompanied by a δCD signal. The difference between the δCD dynamics for OBIP and OxyBP is the most striking feature. It indicates that the underlying mechanisms must be quite different in the two species. Similar conclusions have been reached in reference [143]: whereas absorption changes in OxyBP in the short time range was shown to come mainly from solvation dynamics, those in OBIP were assigned to an electron transfer from the chromophore to the protein backbone. Our present results are in perfect agreement with the

conclusion that the protein environment drives the excited chromophore to a different and fast deactivation process.

For hypericin and analogous compounds containing the same chromophore [152], the phenanthroperylene quinone system is not planar, the two anthrone moieties of the molecule lying in two skewed planes. In the case of OxyBP, no strong structural changes occur upon excitation and therefore the differential CD remains constant whereas for OBIP, changes originate in a charge transfer with dramatic consequences on the CD signal. One indeed expects changes in the chirality of the hypericin-like structure of the chromophore (figure 6.1) after the loss of a π-electron and subsequent reorganization of the single and double bonds within the phenanthroperylene quinone rings. One might also suggest that the observed fast decay of δCD contains information on the hypothesized fast structural responses in the local protein environment resulting from the electron transfer. Unfortunately, at present, the 3D structure of the protein is unknown and it is not possible to go further in the interpretation of the δCD changes. Nevertheless, comparison of OxyBP and OBIP not only strongly supports the conclusions previously reached that reactive OBIP undergoes a fast photoinduced reaction but also brings the additional information that a structural reorganization of the chromophore is involved in this reaction.

As far as we can tell, the signals that we have observed pertain to the so-called reactive form of OBIP proposed to act as a sunscreen of the light-adapted form of B. japonicum [141–143]. However, as discussed in previous works [142, 143] the non-reactive form is suspected to be the genuine trigger of the photophobic response of B. japonicum and photoexcitation of the chromophore, leading to a hypothetical proton transfer to the protein [143], could be the starting point of a structural reorganization of the protein backbone. In that case, transient CD spectroscopy should be able to monitor these changes on the condition that much longer timescale be used.

6.5. Conclusion

We have performed the first picosecond transient circular dichroism study of OBIP, the putative photoreceptor protein involved in the photophobic response of the light-adapted form of the protozoan B. japonicum. The probe wavelength was chosen at 230 nm, a wavelength where the alpha helices of the protein backbone have a dominant contribution to

the steady-state CD spectrum of OBIP [149]. The results were compared to those of the isolated chromophore, OxyBP, in solution. We observe that the CD changes in OBIP and OxyBP do not follow the same dynamics. Although no slow motion of the protein backbone could be observed in the temporal window under investigation, OBIP was found to display a CD relaxation in a few picoseconds whereas no such relaxation is obtained for OxyBP. This brings a strong support to the existence of a fast photoinduced process in the reactive form of OBIP and demonstrates that local geometrical changes accompany the charge transfer between the chromophore and the protein, inferred from previous experiments [143].

CONCLUSION

As introduced in chapter 1 how important it is to understand the mechanism behind the mystery of protein folding/unfolding processes in the way to find a cure or prevention for illnesses caused by protein misfolding, we aim to contribute in the whole work for answering the protein folding/unfolding problem, which have been currently a great concern in biophysics nowadays. We learnt that the laser-induced temperature jump is currently the most versatile and simplest approach for the initiation of fast folding/unfolding processes of proteins and peptides. On the other hand, the amide bond, which is present in all proteins and peptides, has a circular dichroism. The CD spectra of proteins and peptides in the far UV can be extracted to obtain information on the fraction of a molecule that is in different secondary structure configuration, such as α-helices, β-sheets and random coils. Therefore, we put our ambition in developing a temperature jump experiment in combination with CD spectroscopy for a quantitative investigation of the folding/unfolding dynamics of the proteins and peptides.

We described in chapter 2 a complete set-up allowing for the first time the measurement of far UV-CD changes in a temperature jump experiment. The experiment is based on the use of a nanosecond Nd:YAG-pumped OPO to generate an infrared pulse to heat up the water solvent whereas the probe is a far UV pulse generated by a 1 kHz, Titanium-Sapphire based laser system. A full synchronization device was developed to trigger the two laser sources with a delay that is controllable with a 12.1 ns time step. Several detection schemes were proposed and implemented. It showed that three different techniques yield equivalent results, providing a good flexibility to the acquisition system.

The first stage in developing a temperature jump experiment is the measurement of the temperature jump. Chapter 3 presented our measurements of the temperature increase during the temperature jump experiment with the help of visible pulses. A solution mixing a temperature-dependent buffer (Tris HCl) and a pH indicator (Bromothymol Blue) was proven to be very efficient and allowed us to fully characterize our temperature jump apparatus. The

results of our temperature jump determinations yielded a maximum T-jump of 5°C obtained with a 500 μm pump beam focus and a pump energy of 8mJ/pulse in a 100 μm pathlength quartz cell continuously rotated at 300rpm. Moreover, a constant temperature on the time scale of hundreds of microseconds was observed, allowing measurements of folding/unfolding dynamics of proteins and peptides from tens of nanosecond to hundreds of microsecond timescale.

Our CD/T-jump experiment was applied to investigate the unfolding dynamics of poly(glutamic acid). Chapter 4 showed the results of CD/T-jump measurements on our PGA peptide sample with a T-jump of 4-5°C from initial temperatures of 21 and 28°C. We observed a relaxation time constant of 1.5 μs at 25°C and 0.6 μs at 32°C. Also importantly, our CD experiment provide quantitative information of the unfolding process: we measured a drop of the helical fraction from 41% to 36% when the temperature jumped from 28 to 32°C and from 47% to 43% when it went from 21 to 26°C. Our CD/T-jump experiment will be employed to study the unfolding dynamics of short alanine-based peptides and the photocycle of Bacteriorhodopsin following the photoexcitation of the retinal which is bound to the protein.

In the course of our collaboration with Dr. Martin Volk at University of Liverpool (UK), we have studied the unfolding dynamics of a leucine-zipper like coiled-coil peptide using his IR/T-jump experiment. Chapter 5 presented the results of our IR/T-jump measurements on our coiled-coil peptide samples with a T-jump of ~ 1°C. We observed an unfolding relaxation kinetics of the coiled-coil peptide samples, which occurred on a hundred of microseconds time scale. At a given starting temperature, two different average relaxation times are observed for two peptide concentrations. This is due to the difference in entropy of the samples at two peptide concentrations (since the activation energies found for two concentrations are similar). Moreover, the results exhibit a non-monoexponential relaxation kinetics, which identifies the existence of some intermediates during the course of the peptide unfolding. In the near future, the unfolding dynamics of the coiled-coil peptide will be investigated in our CD/T-jump measurements. Since the cooling is much slower in the CD/T-jump experiment, it is possible and also interesting to study the thermal denaturation dynamics on a much longer time scale.

On the other hand, we took advantage of the picosecond time-resolved CD experiment that has been previously developed during Claire Niezborala's PhD project to study the first

picosecond transient circular dichroism of OBIP, the putative photoreceptor protein involved in the photophobic response of the light-adapted form of the protozoan B. japonicum. We probed at 230 nm, a wavelength where the α-helices of the protein backbone have a dominant contribution to the steady-state CD spectrum of OBIP [149]. The observed CD changes in OBIP and OxyBP did not follow the same dynamics: OBIP's signal relaxes in a few picoseconds whereas no such relaxation is obtained for OxyBP. This observation brings a strong support to the formerly evoked existence of a fast photoinduced reaction in the chromoprotein and demonstrates that implication of local geometrical changes that accompany this process [143].

BIBLIOGRAPHY

1. C. B. Anfinsen, Science **181**, 223-230 (1973).
2. A. Pozo Ramajo, S. A. Petty and M. Volk, Chem. Phys. **323**, 11-20 (2006).
3. C. A. Rohl and R. L. Baldwin, Biochemistry **36**, 8435-8442 (1997).
4. C.–Y. Huang, J. W. Klemke, Z. Getahum, W. F. DeGrado and F. Gai, J. Am. Chem. Soc. **123**, 9235-9238 (2001).
5. S. Marquee, V. H. Robbins and R. L. Baldwin, Proc. Natl. Acad. Sci. **86**, 5286-5290 (1989).
6. T. Wang, D. Du and F. Gai, Chem. Phys. Lett. **370**, 842-848 (2003).
7. P. Li, F. Y. Oliva, A. N. Naganathan and V. Muñoz, Proc. Natl. Acd. Sci. **106**, 103-108 (2009).
8. O.B. Ptitsyn, Doklady Akademii Nauk SSSR **210**, 1213-1215 (1973).
9. M. Karplus and D. L. Weaver, Protein Science **3**, 650-668 (1994).
10. K. A. Dill, Biochemistry **24**, 1501-1509 (1985).
11. A. R. Fersht, Curr. Opin. Struct. Biol. **7**, 3-9 (1997).
12. M. Volk, Eur. J. Org. Chem., 2605-2621 (2001).
13. P. E. Leopold, M. Montal, and J. N. Onuchic, Proc. Natl. Acad. Sci. **89**, 8721–8725 (1992).
14. J. D. Bryngelson, J. N. Onuchic, N. D. Socci and P. G. Wolynes, Proteins:Struct. Funct. Genet. **21,** 167–195 (1995).
15. D. Shortle, FASEB J. **10,** 27–34 (1996).

16. F. Chiti and C. Dobson, Annu. Rev. Biochem. **75**, 333–366 (2006).

17. Y. Duan, L. Wang and P. A. Kollman, Proc. Natl. Acd. Sci. **95**, 9897-9902 (1998).

18. C. M. Jones, E. R. Henry, Y. Hu, C.-K. Chan, S. D. Luck, A. Bhuyan, H. Roder, J. Hofrichter and W. A. Eaton, Proc. Natl. Acd. Sci. **90**, 11860-11864 (1993).

19. J. R. Telford, P. Wittung-Stafshede, H. B. Gray and J. R. Wrinkler, Acc. Chem. Res. **31**, 755-763 (1998).

20. P. Wittung-Stafshede, J. C. Lee, J. R. Wrinkler and H. B. Gray, Proc. Nalt. Acad. Sci. **96**, 6587-6590 (1999).

21. E. Chen, M. J. Wood, A. L. Fink and D. S. Kliger, Biochemistry **37**, 5589-5598 (1998).

22. P. Wittung-Stafshede, J. C. lee, J. R. Wrinkler and H. B. Gray, Proc. Natl. Acd. Sci. **96**, 6597-6590 (1999).

23. W. K. Surewicz, H. H. Mantsch and D Chapman, Biochemistry **32**, 389-394 (1993).

24. T. Miyazawa, J. Chem. Phys. **32**, 1647-1652 (1960).

25. S. A. Petty and M. Volk, Phys. Chem. Chem. Phys. **6**, 1022-1030 (2004).

26. C. M. Phillips, Y. Mizutani and R. M. Hochstrasser, Proc. Natl. Acad. Sci. **92**, 7292-7296 (1995).

27. R. Gilmanshin, S. Williams, R. H. Callender, W. H. Woodruff, R. B. Dyer, Proc. Natl. Acd. Sci. **94**, 3709-3713 (1997).

28. D. T. Leeson, F. Gai, H. M. Rodriguez, L. M. Gregoret, R. B. Dyer, Proc. Natl. Acd. Sci. **97**, 2527-2532 (2000).

29. D. M. Vu, J. K. Myers, T. G. Oas, and R. B. Dyer, Biochemistry **43**, 3582–3589 (2004).

30. E. A. Gooding, A. P. Ramajo, J. Wang, C. Palmer, E. Fouts and M. Volk, Chem. Commun., 5985-5987 (2005).

31. S. Williams, T. P. Causgrove, R. Gilmanshin, K. S. Fang, R. H. Callender, W. H. Woodruff, and R. B. Dyer, Biochemistry **35**, 691–697 (1996).

32. R. B. Dyer, F. Gai, W. H. Woodruff, R. Gilmanshin and R. H. Callender, Acc. Chem. Res **31**, 709-716 (1998).

33. T. P. Causgrove and R. B. Dyer, J. Chem. Phys. **232**, 2-10 (2006).

34. W. Barber-Armstrong, T. Donaldson, H. Wijesooriya and S. M. Decatur, J. Am. Chem. Soc. **126**, 2339-2345 (2004).

35. S. H. Brewer, B. Song, D. P. Raleigh, and R. B. Dyer, *Biochemistry* **46**, 3279–3285 (2007).

36. S. M. Decatur and J. Antonic, J. Am. Chem. Soc. **121**, 11914-11915 (1999).

37. B. Nölting, R. Golbik and A. R. Fersht, Proc. Natl. Acd. Sci. **92**, 10668-10672 (1995).

38. B. Nölting, R. Golbik, J. L. Neira, A. S. Soler-Gonzalez, G. Schreiber and A. R. Fersht, Proc. Natl. Acd. Sci. **94**, 826-830 (1997).

39. R. M. Ballew, J. Sabelko and M. Gruebele, Nat. Struct. Biol. **3**, 923-926 (1996).

40. J. Sabelko, J. Ervin and M. Gruebele, Proc. Natl. Acd. Sci. **96**, 6031-6036 (1999).

41. M. P. Lillo and J. M. Beechem, Biochemistry **36**, 11261-11272 (1997).

42. R. M. Ballew, J. Sabelko and M. Gruebele, Proc. Natl. Acd. Sci. **93**, 5759-5764 (1996).

43. C.–K. Chan, J. Hofrichter and W. A. Eaton, Science **274**, 628-629 (1996).

44. M. C. R. Shastry, J. M. Sauder and H. Roder, Acc. Chem. Res. **31**, 717-725 (1998).

45. Z. Chi, X. G. Chen, J. S. W. Holtz and S. A. Asher, Biochemistry **37**, 2854-2864 (1998).

46. C.-Y. Huang, G. Balakrishnan and T. G. Spiro, J. Raman Spectrosc. **37**, 277-282 (2006).

47. I. K. Ledvev, A. S. Karnoup, M. C. Sparrow and S. A. Asher, J. Am. Chem. Soc. **121**, 8074-8086 (1999).

48. G. Balakrishnan, Y. Hu, G. M. Bender, Z. Getahun, W. F. DeGrado and T. G. Spiro, J. Am. Chem. Soc. **129**, 12901-12808 (2007).

49. G. Balakrishnan, Y. Hu, M. A. Case and T. G. Spiro, J. Phys. Chem. **110**, 19877-19883 (2006).

50. R. D. JiJi, G. Balakrishnan, Y. Hu and T. G. Spiro, Biochemistry **45**, 34-41 (2006).

51. C-Y. Huang, G. Balakrishnan and T. G. Spiro, Biochemistry **44**, 15734-15742 (2005).

52. I. K. Lednev and V. A. Shashilov, J. Am. Chem. Soc. **130**, 309-317 (2008).

53. G. Balakrishnan, Y. Hu, O. F. Oyerinde, J. Su, J. T. Groves and T. G. Spiro, J. Am.

Chem. Soc. **129**, 504-505, (2007).

54. A. V. Mikhonin, S. A. Asher, S. V. Bykov and A. Murza, J. Phys. Chem. B **111**, 3280–3292 (2007).

55. E. Chen, J. R. Kumita, G. A. Woodley and D. S. Kliger, J. Am. Chem. Soc. **125**, 12443-12449 (2003).

56. E. Chen, T. E. Swartz, R. A. Bogomolni and D. S. Kliger, Biochemistry **46**, 4619-4624 (2007).

57. E. Chen, C. J. Abel, R. A. Goldbeck and D. S. Kliger, Biochemistry **46**, 12463-12472 (2007).

58. R. A. Goldbeck, D. S. Kliger, R. M. Esquerra and D. S. Kliger, Proc. Nalt. Acad. Sci. **96**, 2782-2787 (1999).

59. L. Pollack, M. W. Tate, N. C. Darnton, J. B. Knight, S. M. Gruner, W. A. Eaton and R. H. Austin, Proc. Nalt. Acad. Sci. **96**, 10115-10117 (1999).

60. S. Abbruzzetti, E. Crema, L. Masino, A. Vecli, C. Viappiani, J. R. Small, L. J. Libertini and E. W. Small, Biophys. J. **78**, 405-415 (2000).

61. J. Mikšovská and R. W. Larsen, J. Protein Chem. **22**, 387-394 (2003).

62. V. M. Grigoryants, A. V. Veselov and C. P. Scholes, Biophys. J. **78**, 2702-2708 (2000).

63. R. Mandel and G. Holzwarth, J. Chem. Phys. **57**, 3469-3477 (1972).

64. W. Moffitt, J. Chem. Phys **25**, 467-478 (1956).

65. R. W. Woody, Tetrahedron: Asymmetry **4**, 529-544 (1993).

66. Circular dichroism, the Conformational Analysis of Biomolecules (Ed: G. Fasman), Plenum Publishers, New York, 1996.

67. L. Whitmore and B. A. Wallace, Biopolymers **89**: 392-400 (2008).

68. P. A. Jennings, P. E. Wright, Science **262**, 892-895 (1993).

69. G. A. Elöve, A. F. Chaffotte, H. Roder and M. E. Goldberg, Biochemistry **31**, 6876-6883 (1992).

70. P. Regenfuss, R. M. Clegg, M. J. Fulwyler, F. J. Barrantes and T. M. Jovin, Rev. Sci. Instrum. **56**, 283-290 (1985).

71. M. C. R. Shastry, S. D. Luck and H. Roder, Biophys. J. **74**, 2714-2721 (1998).

72. C.-K. Chan, Y. Hu, S. Takahashi, D. L. Rousseau, W. A. Eaton and J. Hofrichter, Proc, Nalt. Acad. Sci. **94**, 1779-1784 (1997).

73. S. Takahashi, S.-R. Yeh, T. K. Das, C.-K. Chan, S. D. Gottfried and D. L. Rousseau, Nat. Struct. Biol. **4**, 44-50 (1997).

74. G. Schwarz and J. Seelig, Biopolymers **6**, 1263-1277 (1968).

75. G. G. Hammes and P. B. Roberts, J. Am. Chem. Soc. **91**, 1812-1816 (1969).

76. B. Nölting, M. Jiang and S. G. Sligar, J. Am. Chem. Soc. **115**, 9879-9882 (1993).

77. O. Bieri, J. Wirz, B. Hekkrung, M. Schutkowski, M. Drewello and T. Kiefhaber, Proc. Nalt. Acad. Sci. **96**, 9597-9601 (1999).

78. L. J. Lapidus, W. A. Eaton and J. Hofrichter, Proc. Nalt. Acad. Sci. **97**, 7220-7225 (2000).

79. W. A. Eaton, V. Muñoz, P. A. Thompson, E. R. Henry and J. Hofrichter, Acc. Chem. Res **31**, 745-753 (1998).

80. S. J. Hagen, J. Hofrichter and W. A. Eaton, J. Phys. Chem **101**, 2352-2365 (1997).

81. T. Pascher, J. P. Chesick, J. R. Wrinkler and H. B. Gray, Science **271**, 1558-1560 (1996).

82. J. C. Lee, H. B. Gray and J. R. Wrinkler, Proc. Nalt. Acad. Sci. **98**, 7760-7764 (2001).

83. P. L. Privalov, Y. V. Griko and S. Y. Venyaminov, J. Mol. Biol. **190**, 487-498 (1986).

84. B. H. Zimm, P. Doty and K. Iso, Proc. Nalt. Acad. Sci. **45**, 1601-1607 (1959).

85. H. S. M. Lu, M. Volk, Y. Kholodenko, E. Gooding, R. M. H. Hochstrasser and W. F. DeGrado, J. Am. Chem. Soc. **119**, 7173-7180 (1997).

86. G. Czerlinski and M. Eigen, Z. Elektrochem. **63**, 652-661 (1959).

87. H. Staerk and G. Czerlinski, Nature **205**, 63-64 (1965).

88. P. A. Anfinrud, C. Han and R. M. Hochstrasser, Proc. Nalt. Acad. Sci. **86**, 8387 (1989).

89. L. Richard, L. Genberg, J. Deak, H.-L. Chiu and R. J. D. Miller, Biochemistry **31**, 10703 (1992).

90. P. A. Thompson, W. A. Eaton and J. Hofrichter, Biochemistry **36**, 9200-9210 (1997).

91. J. W. Lewis, R. F. Tilton, C. M. Eiterz, S. J. Milder, I . D. Kuntz and D. S. Kliger, J. Phys. Chem. **89**, 289-294 (1985)

92. X. Xie and J. D. Simon, Rev. Sci. Instrum. **60**, 2614-2626 (1989).

93. Thibault Dartigalongue, Dynamique conformationelle de la myoglobine suivie par dichroïsme circulaire résolu temporellement, PhD thesis, Ecole Polytechnique (2005).

94. E. Chen, R. A. Goldberk and D. S. Kliger, Methods **52**, 3-11 (2010)

95. A. Trifonov, I. Buchvarov, A. Lohr, F. Würthner and T. Fiebig, Rev. Sci. Instrum. **81**, 043104-1-6 (2010); L. Mangot, G. Taupier, M. Romeo, A. Boeglin, O. Cregut and K. D. Dorkenoo, Opt. Lett. **35**, 381-383 (2010).

96. J. Turkevich, P. C. Stevenson, J. Hillier, Discuss. Faraday. Soc. **11**, 55-75 (1951).

97. J. Kimling, M. Maier, B. Okenve, V. Kotaidis, H. Ballot, A. Plech, J. Phys. Chem. B **110**, 15700-15707 (2006).

98. R. W. Boyd, Nonlinear Optics, Second edition, 99-107 (2003).

99. D. E. Spence, P. N, Kean and W. Sibbett, Optics Letters **16**, 42 (1991).

100. D. Strickland and G. Mourou, Optics Communications **56**, 219-221 (1985).

101. Claire Niezborala, Une nouvelle technique de mesure du dichroïsme circulaire : premiers pas vers l'étude du repliement de polypeptides modèles, PhD thesis, Ecole Polytechnique (2008).

102. C. Niezborala and F. Hache, J. Opt. Soc. Am. B **23**, 2418-2424 (2006).

103. P. Bayley, S. Martin and M. Anson, Biochem. Biophys. Res. Commun. 66, 303 (1975).

104. W. O. Wray, T. Aida and R. B. Dyer, Appl. Phys. B **74**, 57 (2002)

105. E. F. Chen, Y. W. Lewis, R. A. Goldbeck, D. S. Kliger and C. E. M. Strauss, Rev. Sci. Instrum. **76**, 083120 (2005).

106. P. Doty, A. Wada, J. T. Yang and E. R. Blout, J. Polym. Sci. **23**, 851-861 (1957).

107. M. Nagasawa and A. Holtzer, J. Am. Chem. Soc. **86**, 538-543 (1963).

108. D. S. Olander and A. Holtzer, J. Am. Chem. Soc. **90**, 4549-4560 (1968).

109. B. R. Jennings, G. Spach and T. M. Schuster, Biopolymers **6**, 635-652 (1968).

110. Sapna Sharma, Helix-coil transition dynamics of α-helical peptides, PhD thesis,

University of Liverpool (2006).

111. C. Krejtschi and K. Hauser, Eur. Biophys. J. **40**, 673-685 (2011).

112. F. Bordi, C. Cametti and G. Paradossi, Phys. Chem. Chem. Phys. **1**, 1555-1561 (1999).

113. K. Rosenheck and P. Doty, Biochemistry **47**, 1175-1785 (1961).

114. S. Krimm and J. Bandekar, J. Adv. Protein. Chem. **38**, 181-364 (1986).

115. A. Jabs, http://www.imb-jena.de/imglibDoc/ftir/IMAGE_FTIR.html: Home page of IMBjena (image library of Biological molecules), 1999.

116. W. K. Surewicz and H. H. Mantsch, Biochem. Biophys. Research Comm. **952**, 115-130 (1988).

117. H. Wendt, A. Baici, and H. R. Bosshard, J. Am. Chem. Soc. **116**, 6973–6974 (1994).

118. T. R. Sosnick, S. Jackson, R. R. Wilk, S. W. Englander and W. F. DeGrado, Proteins **24**, 427–432 (1996).

119. L. B. Moran, J. P. Schneider, A. Kentsis, G. A. Reddy and T. R. Sosnick, Proc. Natl. Acad. Sci. **96**, 10699–10704 (1999).

120. B. A. Krantz and T. R. Sosnick, Nat. Struct. Biol. **8**, 1042–1047 (2001).

121. J. A. Zitzewitz, B. Ibarra-Molero, D. R. Fishel, K. L. Terry and C. R. Matthews, J. Mol. Biol. **296**, 1105–1116 (2000).

122. B. Ibarra-Molero, G. I. Makhatadze and C. R. Matthews, Biochemistry **40**, 719–731 (2001).

123. J. A. Zitzewitz, O. Bilsel, J. B. Luo, B. E. Jones and C. R. Matthews, Biochemistry. **34**, 12812–12819 (1995).

124. Y. Bai, Biochem. Biophys. Res. Commun. **305**, 785–788 (2003).

125. T. Wang, W. L. Lau, W. F. DeGrado and F. Gai, Biophys. J. **89**, 4180-4187 (2005).

126. G. Balakrishnan, Y. Hu, M. A. Case and T. G. Spiro, J. Phys. Chem. **110**, 19877-19883 (2006).

127. M. R. Bunagan, L. Cristian, W. F. DeGrado and F. Gai, Biochemistry **45**, 10981-10986 (2006).

128. K. J. Lumb, C. M. Carr and P. S. Kim, Biochemistry **33**, 7361-7367 (1994).

129. Angela Pozo Ramjo, Fast folding dynamics of α-helical peptides, PhD thesis, University of Liverpool (2006).

130. Renee Peta-Gaye Whynes, Fast folding dynamics of proteins and peptides, PhD thesis, University of Liverpool (2010).

131. A. C. Giese, Blepharisma; The biology of a light-sensitive protozoan, Stanford University Press, CA 1973.

132. M. Kraml, W. Marwan, Photochem. Photobiol. **37**, 313-319 (1983).

133. G. Checcucci, R. S. Shoemaker, E. Bini, R. Cerny, N. Tao, J.-S. Hyon, D. Gioffre, F. Ghetti, F. Lenci and P.-S. Song, J. Am. Chem. Soc. **119**, 5762-5763 (1997).

134. M. Maeda, H. Naoki, T. Matsuoka, Y. Kato, H. Kotsuki, K. Utsumi and T. Tanaka, Tetrahedron Lett. **38**, 7411-7414 (1997).

135. D. Spitzner, G. Höfle, I. Klein, S. Pohlan, D. Ammermann and L. Jaenicke, Tetrahedron Lett. **39**, 4003-4006 (1998).

136. A. C. Giese, J. Cell. Compar. Physiol. **28**, 119-127 (1946).

137. G. Checcucci, G. Damato, F. Ghetti, F. Lenci, Photochem. Photobiol. **57**, 686-689 (1993).

138. T. Matsuoka, S. Matsuoka, Y. Yamaoka, T. Kuriu, Y. Watanabe, M. Takayanagi, Y. Kato and K. Taneda, J. Protozool. **39**, 498-502 (1992).

139. T. Matsuoka, M. Sato, M. Maeda, H. Naoki, T. Tanaka and H. Kotsuki, Photochem. Photobiol. **65**, 915-921 (1997).

140. T. Matsuoka, D. Tokumori, H. Kotsuki, M. Ishida, M. Matsushita, S. Kimura, T. Itoh and G. Checcucci, Photochem. Photobiol. **75**, 709-713 (2000).

141. M. Mahet, P. Plaza, M. M. Martin, G. Checcucci and F. Lenci, J. Photochem. Photobiol. A: Chemistry **185**, 345-353 (2007).

142. P. Plaza, M. Mahet, M. M. Martin, G. Checcucci and F. Lenci, J. Phys. Chem. B **111**, 690-696 (2007).

143. J. Blazard, C. Ley, F. Lacombat, M. Mahet, P. Plaza, M. M. Martin, G.Checcucci and F. Lenci, J. Phys. Chem. B **112**, 15182-15194 (2008).

144. M. M. Martin, N. Ikeda, T. Okada and N. Mataga, J. Phys. Chem. **86**, 4148-4156

(1982).

145. N. Mataga, Pure Appl. Chem. **56**, 1255-1268 (1984).

146. H. Miyasaka, A. Tabata, S. Ojima, N. Ikeda and N. Mataga, J. Phys. Chem. **97**, 8222-8228 (1993).

147. H. Tanaka, K. Nishimoto, J. Phys. Chem. **88**, 1052-1055 (1984).

148. A. L. Sobolewski and W. G. Domcke, J. Phys. Chem. A **111**, 11725-11735 (2007).

149. O. Pieroni, P. Plaza, M. Mahet, N. Angelini, G. Checcucci, M. Malatesta, M. M. Martin and F. Lenci, Photochem. Photobiol. **81**, 1343-1346 (2005).

150. F. Hache, J. Photochem. Photobiol. A **204**, 137-143 (2009).

151. G. Checcucci, Y. Takada and T. Matsuoka, Mem. Fac. Sci. Kochi Uni. D **22**, 39-44 (2001).

152. H. Falk, Angew. Chem. **38**, 3116-3136 (1999).

153. A. Shibata, M. Yamamoto, T. Yamashita, J.-S. Chiou, H. Kamaya and I. Ueda, Biochim. Biophys. Acta. **31**, 5728-5733 (1992).

154. M. Jackson, P.I. Haris and D. Chapman, Biochim. Biophys. Acta. **998**, 75-79 (1989).

Résumé

La question de savoir comment les protéines se replient dans leur propre structure tridimentionnelle offre un défi passionnant pour les biophysiciens de nos jours. L'utilisation d'un saut de température rapide est une technique très puissante pour l'étude du processus de dénaturation des protéines. Toutefois, sonder la structure secondaire est un défi difficile et on obtient rarement des valeurs quantitatives.

Le but principal de ce projet de thèse est de développer une mise en œuvre technique de dichroïsme circulaire dans l'UV extrême dans une expérience de saut de température nanoseconde. Notre expérience permet de suivre quantitativement l'évolution de la fraction hélicoïdale d'un peptide poly(acide glutamique) au cours de sa dénaturation thermique avec une résolution de 12 ns de temps.

Abstract

The question how proteins fold into their specific three-dimentional structures provides an exciting challenge for biophysicists nowadays. The use of a fast temperature-jump is a very powerful technique for the study of the denaturation process of proteins. However, probing the secondary structure is a difficult challenge and rarely yields quantitative values.

The main purpose of this PhD project is to develop a technical implementation of far-UV circular dichroism in a nanosecond T-jump experiment. Our CD/T-jump experiment allows us to follow quantitatively the change in the helical fraction of a poly(glutamic acid) peptide during its thermal denaturation with 12 ns time resolution.